

Rochester Institute of Technology

RIT Digital Institutional Repository

Theses

12-2022

Electrolyte loss and voltage degradation of HT-PEM fuel cells operated at 200oC.

Jared Oscar Leader
jl1111@rit.edu

Follow this and additional works at: <https://repository.rit.edu/theses>

Recommended Citation

Leader, Jared Oscar, "Electrolyte loss and voltage degradation of HT-PEM fuel cells operated at 200oC." (2022). Thesis. Rochester Institute of Technology. Accessed from

This Dissertation is brought to you for free and open access by the RIT Libraries. For more information, please contact repository@rit.edu.

Electrolyte loss and voltage degradation of HT-PEM fuel cells operated at 200°C.

By

Jared Oscar Leader

A DISSERTATION

Submitted in partial fulfillment of the requirements

for the degree of Doctor of Philosophy

in

Sustainability

Department of Sustainability

Golisano Institute for Sustainability

Rochester Institute of Technology

December 2022

CERTIFICATE OF APPROVAL

Golisano Institute for Sustainability

Rochester Institute of Technology

Rochester, New York

Ph.D. DEGREE DISSERTATION

The Ph.D. Degree Dissertation of Jared Oscar Leader has been examined and approved by the dissertation committee as satisfactory for the dissertation requirement for the Ph.D. degree in Sustainability.

Dr. Thomas A. Trabold
Research Professor
Golisano Institute for Sustainability
Rochester Institute of Technology
Advisor

Dr. Nenad Nenadic
Research Professor
Golisano Institute for Sustainability
Rochester Institute of Technology
Committee Member

Dr. Thomas W. Smith
Professor
School of Chemistry and Material Science
Rochester Institute of Technology
Committee Member

Dr. Michael G. Waller
Chief Executive Officer
Falcon Fuel Cells, Inc.
External Committee Member

Dr. Christopher L. Lewis
Associate Professor
College of Engineering Technology
Rochester Institute of Technology
Dissertation Exam Chairperson

Dr. Amitrajeet A. Batabyal
Interim Department Head
Golisano Institute for Sustainability
Rochester Institute of Technology

Date

Abstract

As the world transitions toward a more sustainable energy future, it becomes clear that fuel cells will play a role in the global sustainable energy infrastructure. Of the many types of fuel cells, high temperature proton exchange membrane (PEM) fuel cells operating in the range of 120-200°C are particularly interesting as they offer several advantages over low temperature proton exchange membrane fuel cells. Most notably high temperature proton exchange membrane fuel cells exhibit increased tolerance to fuel impurities and simplified water management system requirements. These advantages are offset by a significantly shortened operational lifespan which makes high temperature proton exchange membrane cells suitable for small rugged applications including unmanned aerial vehicles, emergency backup power systems, and portable power production. The focus of this research is to extend the lifespan of high temperature membrane electrode assemblies (MEA's) through a fundamental understanding of what the degradation modes are, what common process parameters best suit high temperature operation, and an understanding of the role of water in cell operation. The research is focused on operation at the higher reaches of the high temperature PEM range at 200°C. Initially the gap in previous literature will be identified and addressed as the exact degradation rate at our ideal operating conditions is not well understood with commercially available MEAs. Postmortem and in situ analysis of MEAs was undertaken to better understand the modes of degradation. This was followed with testing into the effective role of water on cell function and with innovative MEA design to promote cell longevity. To explore the impact of utilizing reformat fuels, a techno-economic analysis was undertaken comparing solid oxide fuel cells (SOFC) to high temperature proton exchange membrane fuel cells (HT-PEM) for use with a pyrolysis process.

Acknowledgements

This endeavor would not have been possible without the wisdom and steadfast support of my advisor, Dr. Thomas Trabold. Without his mentorship, encouragement, and patience none of this would have been realized. Beyond the laboratory and the program, itself, I have found his passion for sustainability infectious. It is that enthusiasm, which he brings to every task that I strive to emulate in my own life. I would also like to extend my gratitude to my dissertation committee of Dr. Smith, Dr. Waller, Dr. Nenadic, and my committee chair Dr. Lewis for their guidance and input throughout this process.

My time at RIT has been made more enjoyable by friends I have made within my cohort. Ajay Gupta, Sinoun Phoung, and Alexa Kaminski have all contributed to this work through both insight and moral support. Their friendship has made these last few years memorable.

Throughout my work both in and out of the laboratory I have enjoyed the support of both Mark Walluk and Chris Piggott. Their willingness to assist me on a myriad of issues, often at inopportune times, is both more than I could have asked for and worthy of recognition. I am thankful for their advice and generous support.

I would be amiss not to assign 100% of the credit for this work to my father, Dave Leader, as he has claimed he deserves it. With all the effort he has had to expend on my upbringing, who could disagree with him. Throughout all the late nights and complications, he was always there to offer some keen insight born of his years of experience. My sister, Dr. Leader, is credited with introducing me to the program and paving the way for me in both my current and previous endeavors. Watching her excel through life has given me a path to follow and aspire towards. Without her I would not be here today. I would like to thank my mother (for adding commas to

my work), grandparents, and my younger sisters Sam and Jo for their encouragement. I would also like to thank Kayla Bicknell for her assistance in editing and reviewing my papers as well as for making room in our relationship for my work towards this dissertation. She has always been willing to offer advice where she can or a listening ear if needed.

I also gratefully acknowledge the financial support of the New York State Center of Excellence in Advanced & Sustainable Manufacturing, New York Empire State Development, FuzeHub Manufacturing Grant program of New York State, and Rochester Institute of Technology for tuition support.

Table of Contents

Acronyms / Abbreviations	8
List of Tables	9
List of Figures	10
Chapter 1 - Introduction	15
Background	15
Fuel Impurities.....	16
Voltage Degradation Rate	17
Fuel Cell Fundamentals.....	23
HT-PEM Fuel Cell Stands	24
<i>Stand 1</i>	24
<i>Stand 2</i>	25
<i>Stand 3</i>	27
Citations Chapter 1	27
Chapter 2 – Optimization of Membrane Electrode Assembly (MEA) Fabrication	32
Overview of Membrane Electrode Assembly	32
MEA Sample Preparation.....	34
MEA Experimental Methods	36
Conductivity and Bond Strength Results	37
Impact of Pressing Conditions on Repeatability	41
Identification of Optimal Pressing Conditions.....	44
Impact of Pressing Conditions on Electrolyte Hydration.....	44
Impact of Catalyst Layer Thickness on Performance	48
Conclusions and Implications	50
Citations Chapter 2.....	51
Chapter 3 - Voltage Degradation of High-Temperature PEM Fuel Cells Operating at 200°C Under Constant Load	52
Materials and Methods	52
Experimental Voltage Degradation Apparatus.....	52
Results	55
<i>Voltage Degradation Rate</i>	55

<i>Normalized Voltage</i>	57
<i>Voltage Degradation Rate Calculation</i>	58
Discussion	59
Conclusions	60
Citations Chapter 3.....	61
Chapter 4 - Assessment of Electrolyte Degradation of HT-PEM Fuel Cells at 200°C Under Constant Load.	62
Experimental Materials and Methods	71
Performance and Durability Testing Protocol.....	72
pH Measurement.....	73
Phosphoric Acid Content Measurement	74
Oxygen-to-Phosphorous Ratio Measurement.....	76
Results and Discussion.....	78
Conclusions	92
Citations Chapter 4.....	93
Chapter 5 - Mitigating Degradation of HT-PEM Systems Operated at 200°C	97
Introduction	97
Experimental Materials and Methods	97
<i>High-frequency resistance (HFR) measurement</i>	97
<i>pH measurement</i>	97
Results and Discussion.....	98
<i>Raw data</i>	98
<i>Normalized Data</i>	100
<i>Effect of Humidity</i>	102
<i>Effect of Pressure</i>	113
<i>Water and pH measurements</i>	123
<i>High-frequency resistance (HFR)</i>	127
<i>Phosphorus acid content</i>	130
Oxygen-to-Phosphorus Ratio	134
Conclusions and Future work.....	137
Citations Chapter 5.....	138
Chapter 6 - Comparative Analysis of HT-PEM Performance Versus Results of Prior Studies	139

<i>Application of TPS Type MEAs</i>	146
TPS 1	147
TPS 2	148
TPS 3	150
<i>Presentation of Normalized Data</i>	152
Conclusions	153
Citations Chapter 6.....	153
Chapter 7 - Techno-Economic Analysis of SOFC vs. HT-PEM for use with Reformate Fuel Derived from Co-pyrolysis	155
Introduction	155
Methods and Results	156
<i>Co-pyrolysis system</i>	157
<i>SOFC system</i>	162
<i>HT-PEM system</i>	165
Cost Analysis.....	167
Conclusions and Future Work.....	169
Citations Chapter 7.....	170
Chapter 8 - Conclusions and Future Outlook	175
Appendix -Chapter 1	178
Appendix -Chapter 6.....	179
160°C POL Curves	179
180°C POL Curves	197
200°C POL Curves	203

Acronyms / Abbreviations

MEA – Membrane electrode assembly

PBI – Polybenzimidazole

Stoich – Stoichiometric ratio

Pt – Platinum

TPS – MEA type supplied by Advent Technologies

HT-PEM – High temperature proton exchange membrane
 LT-PEM – Low temperature proton exchange membrane
 PEM – Proton exchange membrane
 SOFC – Solid oxide fuel cell
 CPOx – Catalytic partial oxidation
 HFR – High frequency resistance

List of Tables

Table 1.1 - Reported HT-PEM voltage degradation rates.....	18
Table 3.1 – Constant load voltage degradation rates, run times, and times to peak voltage.....	55
Table 4.1 - Summary of prior studies of phosphoric acid loss in HT-PEM fuel cells.....	64
Table 4.2 - Comparison of voltage degradation rates for three tested MEAs.....	80
Table 4.3 - Comparison of oxygen to phosphorus ratios for the virgin MEA and PBI4, 5, and 6 post-durability testing.....	90
Table 5.1- Summary of durability tests and operating parameters.....	100
Table 5.2- Liquid water injections for PBI 7.....	103
Table 5.3- Molar oxygen-to-phosphorus (O/P) ratio measurements.....	134
Table 6.1- Studies utilizing Commercial MEAs sourced in this chapter.....	141
Table 7.1- Summary of prior biomass-plastic co-pyrolysis studies (PLA-Polylactic acid, PE-Polyethylene, PP-Polypropylene, PS-Polystyrene , PHB- Polyhydroxybutyrate, LDPE-Low density polyethylene, HDPE- High density polyethylene.....	158
Table 7.2- Sample Composition 4B refers to the sample set in the sourced reference.....	162
Table 7.3- Composition of gas exiting the co-pyrolysis process.....	162
Table 7.4- Comparative cost data for SOFC and HT-PEM systems in 2022 dollars.....	169

List of Figures

Figure 1.1 – Cell temperature and current density conditions considered in prior studies of HT-PEM durability studies with hydrogen/air.....	17
Figure 1.2 – Reported voltage degradation rates with hydrogen/air at 0.2 A/cm ² . and temperature of 160, 180 and 200°C, Yellow circles indicate outliers.....	21
Figure 1.3 - Cross-sectional view of fuel cell function diagram.....	23
Figure 1.4 - Electro-pneumatic setup of stand 2.....	26
Figure 2.1 - MEA diagram.....	32
Figure 2.2 - Analysis of resistance vs. hot-press time for all temperature and pressure conditions.....	38
Figure 2.3 - Effects of hot-press pressure, time and temperature on adhesion strength and resistance.....	40
Figure 2.4 - Number of MEA samples resulting in failure during hot-pressing at different pressures	41
Figure 2.5 - Number of MEA samples resulting in failure during hot-pressing for different Times.....	42
Figure 2.6 - Number of MEA samples resulting in a failure during hot-pressing at different temperatures	42
Figure 2.7 - SEM cross-sectional image of MEA fabricated at hot-press conditions of 200°C and 92.68 MPa for 10 min.....	45
Figure 2.8 - Resistance and oxygen-to-phosphorus ratio for MEA sample fabricated at 200°C and 92.68 MPa for 10 minutes, Resistance on the left-hand y-axis is area specific.....	47
Figure 2.9 - Resistance and oxygen-to-phosphorus ratio for MEA sample fabricated at 200°C and 7.72 MPa for 10 minutes.....	48
Figure 2.10 -Polarization curves of in-house MEAs compared against commercial Advent PBI.....	49

Figure 3.1 – In-house voltage degradation experiment with hydrogen/air at 0.2 A/cm ² , 160°C and 101.3 kPa with H ₂ /air stoichiometric ratios = 1.5/2.....	54
Figure 3.2 – Results of triplicate voltage degradation experiments run with Advent PBI materials at 0.4 A/cm ² , 200°C and 101.3 kPa with H ₂ /air stoichiometric ratios = 1.5/2.....	56
Figure 3.3 – Normalized voltage degradation profiles at 0.4 A/cm ² , 200°C and 101.3 kPa with H ₂ /air stoichiometric ratios = 1.5/2.....	57
Figure 4.1 - Conceptual map of HT-PEM degradation modes and their relation to phosphoric acid loss and dehydration.....	70
Figure 4.2 - Flow fields used in fuel cell testing, operated in counter-flow orientation.....	71
Figure 4.3 -Example spectrum from phosphorus quantity measurement ,Shimadzu EDX8100...	74
Figure 4.4 - Calibration curve relating phosphoric acid content to counts per second per micro-amp [CPS/μA].....	76
Figure 4.5 – Results of triplicate voltage degradation experiments run with Advent PBI materials at 0.4 A/cm ² , 200°C and 101.3 kPa with H ₂ /air stoichiometric ratios = 1.5/27.....	79
Figure 4.6 – Normalized voltage degradation profiles at 0.4 A/cm ² , 200°C and 101.3 kPa with H ₂ /air stoichiometric ratios = 1.5/2.....	80
Figure 4.7 -Polarization curves for PBI 5 and 6 measured at beginning-of-life (after break-in) and end-of-life (at completion of durability testing).....	82
Figure 4.8 - pH of water collected at both cathode and anode exhaust for PBI 5 and 6.....	83
Figure 4.9 - Phosphoric acid content of degraded vs virgin MEAs.....	84
Figure 4.10 – MEA mass loss between beginning and end of testing for PBI 4, 5, and 6.....	85
Figure 4.11 – Cross-sectional SEM image of PBI 4, highlighting different layers of the MEA..	88
Figure 4.12 - MEA sample locations for the SEM EDX measurement of oxygen-to-phosphorus ratio. AO = anode outlet, AI = anode inlet, and C = center, figure not to scale.....	89
Figure 5.1 - Results of voltage degradation experiments run with Advent PBI materials at 0.4 A/cm ² , 200°C and atmospheric pressure (PBI 7,8), 200 kPa (PBI 9-11), and 300 kPa (PBI 14) with H ₂ /air stoichiometric ratios = 1.5/2.....	99

Figure 5.2- Normalized voltage degradation profiles at 0.4 A/cm ² , 200°C with H ₂ /air stoichiometric ratios = 1.5/2, atmospheric pressure (PBI 7,8), 200 kPa (PBI 9-11), and 300 kPa (PBI 14)	100
Figure 5.3- Voltage profiles of PBI 7 on stand 2 and stand 3 under varying operational conditions.....	102
Figure 5.4- PBI 7 humidified operation expanded operation on stand 2.....	105
Figure 5.5- voltage degradation profiles of PBI 8 at 0.4 A/cm ² , 200°C, 101.3 kPa with H ₂ /air stoichiometric ratios = 1.5/2, and intermittent humidification.....	109
Figure 5.6- voltage degradation profiles of PBI 11 at 0.4 A/cm ² , 200°C, 0.09 ml/min, and 200 kPa with H ₂ /air stoichiometric ratios = 1.5/2.....	111
Figure 5.7- Impact of pressure fluctuations on voltage, PBI 11.....	112
Figure 5.8- Voltage degradation profiles of PBI 9 and 10 at 0.4 A/cm ² , 200°C, 200 kPa with H ₂ /air stoichiometric ratios = 1.5/2.....	114
Figure 5.9- Polarization curves for PBI 9 measured at beginning-of-life (after break-in) and end-of-life (at completion of durability testing) for temperature of 160, 180 and 200°C at 101.3 kPa (figure A) and 200 kPa (figure B)	115
Figure 5.10- Polarization curves for PBI 10 measured at beginning-of-life (after break-in) and end-of-life (at completion of durability testing) for 3 temperature 160,180,200°C at 100 kPa (figure A) and 200 kPa (figure B)	117
Figure 5.11- Voltage degradation profiles of PBI 14 at 0.4 A/cm ² , 200°C, and 300 kPa with H ₂ /air stoichiometric ratios = 1.5/2.....	118
Figure 5.12- Polarization curves for PBI 14 measured at beginning-of-life (after break-in) and end-of-life (at completion of durability testing) for 160,180,200°C at atmospheric pressure....	120
Figure 5.13- PBI 11 vs PBI 9 effect of pressure fluctuations.....	121
Figure 5.14- pH and volume of water collected at both cathode and anode exhaust for PBI9..	123
Figure 5.15- pH and volume of water collected at both cathode and anode exhaust for PBI10..	124
Figure 5.16- pH and volume of water collected at both cathode and anode exhaust for PBI14..	125

Figure 5.17- Net volume of water collected compared against calculated water production rate for PBI 9, 10, and 14.....	126
Figure 5.18- High-frequency resistance (HFR) as a function of time for PBI 7 and PBI 9	127
Figure 5.19- BOL and EOL measurements of HFR for PBI 10 and 14.....	128
Figure 5.20- Effect of break in procedure on HFR for PBI 9 and 14.....	129
Figure 5.21- Phosphoric acid content of virgin MEAs vs PBI 9, 10, 14, and 16 at EOL.....	130
Figure 5.22- MEA mass loss between beginning and end of testing for PBI 9, 10, 14 and 16...	132
Figure 5.23- Thickness change over testing period of PBI 9,10,11,14, and 16.....	133
Figure 5.24- Break in voltage curves for PBI 6,7,9, and 14	136
Figure 6.1- Comparative voltage and power data for commercially available MEAs operated on H ₂ and air at 160°C	142
Figure 6.2- Comparative voltage and power data for commercially available MEAs operated on H ₂ and air at 180°C.....	144
Figure 6.3- Comparative voltage and power data for commercially available MEAs operated on H ₂ and air at 200°C.....	145
Figure 6.4- (A) Voltage degradation profile of TPS 1 at 0.4 A/cm ² , 200°C, and atmospheric pressure with H ₂ /air stoichiometric ratios = 1.5/2 (B) Polarization curves of TPS 1 at 160, 180, and 200°C and atmospheric pressure with H ₂ /air stoichiometric ratios = 1.5/2	147
Figure 6.5- (A) voltage degradation profiles of TPS 2 at 0.4 A/cm ² , 200°C, and atmospheric pressure with H ₂ /air stoichiometric ratios = 1.5/2 (B) Polarization curves of TPS 2 at 160,180, and 200°C at atmospheric pressure with H ₂ /air stoichiometric ratios = 1.5/2 for both beginning of life (BOL) and end of life (EOL).....	148
Figure 6.6- (A) voltage degradation profiles of TPS 3 at 0.4 A/cm ² , 200°C, and atmospheric pressure with H ₂ /air stoichiometric ratios = 1.5/2 (B) Polarization curves of TPS 3 at 160,180, and 200°C at atmospheric pressure with H ₂ /air stoichiometric ratios = 1.5/2 for both beginning of life (BOL) and end of life (EOL).....	150
Figure 6.7- Normalized voltage degradation profiles of TPS 1,2, and 3 at 0.4 A/cm ² , 200°C with H ₂ /air stoichiometric ratios = 1.5/2.....	152

Figure 7.1- System Diagram.....	157
Figure 7.2- Sub-model of co-pyrolysis and SOFC system.....	164
Figure 7.3- Sub-models of co-pyrolysis, two fuel reforming stages, and HT-PEM systems....	165
Figure 7.4- Presentation of cost data for 1 kW SOFC and HT-PEM systems at annual production scale of 100 units/year.....	168

Chapter 1 - Introduction

Background

Hydrogen fuel cells have found application in many sectors of the economy, including transportation, stationary power, and portable power [1]. Proton exchange membrane (PEM) fuel cells represent one of the many types of fuel cell systems that exist today. Low temperature proton exchange membrane (LT-PEM) fuel cells operate below the boiling point of water, generally in the range of 80-100°C, as dictated primarily by the operational requirements of the solid acid membrane material [2]. The high temperature proton exchange membrane (HT-PEM) variation is a less common system that typically uses a phosphoric acid doped polybenzimidazole (PBI) based membrane electrode assembly (MEA) that operates above the boiling point of water, typically in the range of 160-200°C [3]. Novel HT-PEM membrane chemistries are being explored with operational ranges above 200°C [4]. There is currently a research focus on high temperature systems due to several benefits relative to low temperature proton exchange membrane (LT-PEM), including faster electrode kinetics, superior tolerance to fuel impurities, potential for combined heat and power (CHP) applications, and simplified water management. However, HT-PEM cells are not yet widely adopted, as during operation these systems can experience significant performance loss over time. The objective of this research is to advance the current understanding of HT-PEM operation at 200°C, enabling the development of mobile mid-range power systems (nominally 350 W) that run efficiently on reformed hydrocarbons such as propane, and ultimately on reformed biofuels. Currently, there is a gap in commercial mobile fuel cell system development in the range of 100 W to 1 kW [5].

Fuel Impurities

One drawback to the use of reformat fuels is the presence of impurities that impact cell operation. These impurities can vary depending on the primary fuel, operational parameters, and the reforming system that may be comprised of a combination of auto-thermal, steam reforming, partial oxidation, and water gas shift reactors [6]. Some common impurities include carbon dioxide (CO_2), carbon monoxide (CO), water, and slipped fuel. CO has been shown to have a significant impact on the performance of fuel cells, with CO poisoning being a driving factor behind the development of HT-PEM [7], [8]. CO poisoning refers to the loss in cell performance resulting from the presence of CO in the hydrogen fuel. When CO is present in the hydrogen stream, the cell experiences a loss in power due to the stronger bond between CO and the platinum catalyst than the hydrogen-platinum bond required for normal cell operation [9]. This causes CO to occupy the platinum bonding sites intended for hydrogen bonding and subsequent oxidation. The effect of CO on the cell's performance is reduced at higher temperatures, motivating interest in higher operating temperatures (up to 200°C) for reformates with relatively high CO concentrations, such as propane reformed by catalytic partial oxidation (cPOx) [10].

There is a lack of understanding of the effects of operating parameters on the longevity of HT-PEM fuel cells, although elevated temperature and current density are suspected to be two of the primary factors driving cell degradation due to increased phosphoric acid loss [11].

Voltage Degradation Rate

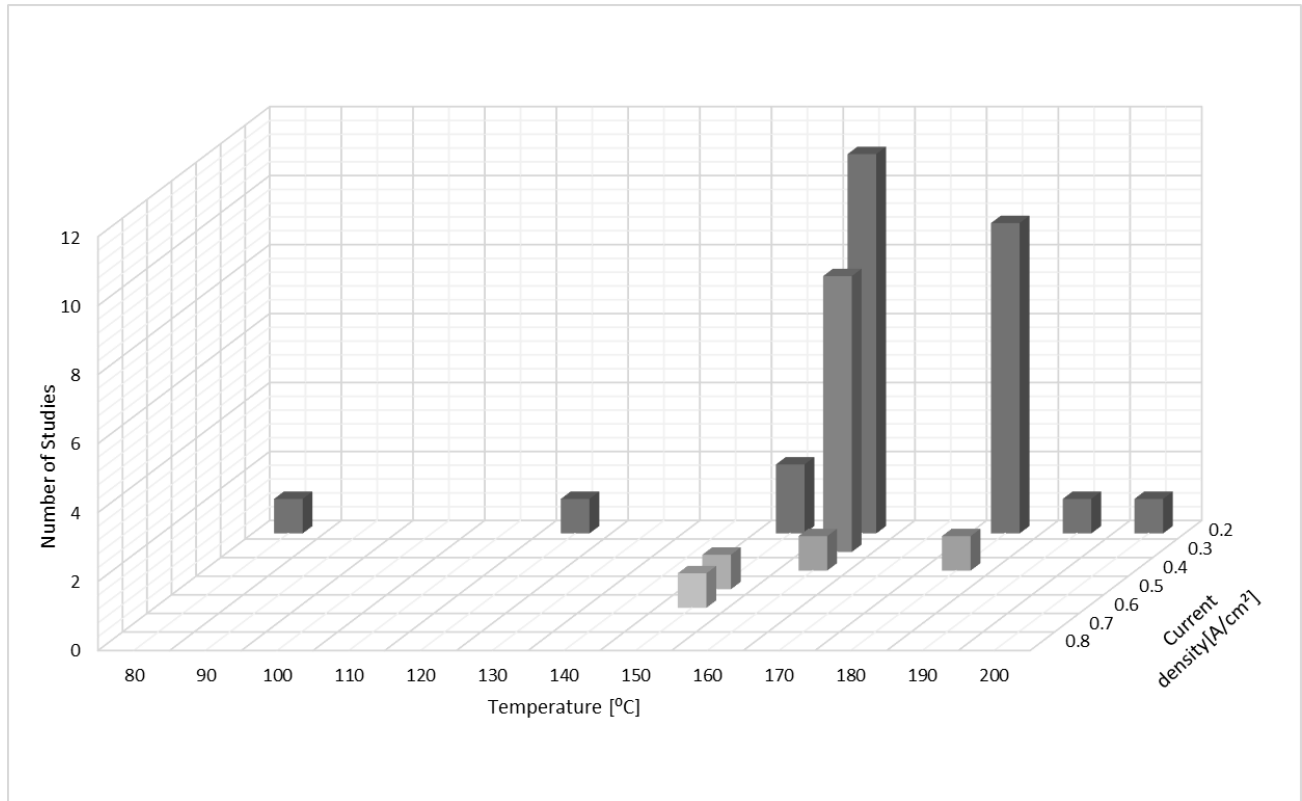


Figure 1.1 – Cell temperature and current density conditions considered in prior studies of HT-PEM durability studies with hydrogen/air

Figure 1.1 shows the number of studies investigating voltage degradation rates for current densities ranging from 0.2 to approximately 0.7 A/cm², and temperatures from 80 to 200°C. Details of the papers included in this graph are provided in Table 1. As the majority of the data were found at a current density of 0.2 A/cm², a close-up of the voltage degradation trend at this current density is provided in Figure 1.2, showing the average reported degradation rate versus cell temperature.

Table 1.1 - Reported HT-PEM voltage degradation rates

Year	Reference	Temperature [°C]	Current density [A/cm ²]	Elapsed time [h]	Degradation Rate [μV/h]	MEA type	Replicates reported?	Comments
2006	[12]	150	0.640	500	150	In-house	N	
2006	[13]	150	0.714	510	81.6	In-house	N	Also investigated intermittent operation
2008	[14]	80	0.2	1,000	45	In-house	N	Investigated different PBI polymers and the effect of temperature
		160	0.2	2,500	4.9			
		190	0.2	800	60			
		120	0.2	14,000	6.3			
2008	[15]	160	0.2	6,000	5	Celtec® P1000	N	Also investigated intermittent operation
2008	[16]	160	0.2	1,000	25	In-house	N	Description of MEA preparation
2009	[17]	160	0.2	780	25	In-house	N	MEA degradation mostly attributed to Pt ESA decrease over time.
2011	[18]	180	0.35	1,600	<10	Celtec® P2100	N	Explored the effect of
		180	0.35	300	400			

		180	0.35	1600	<10			bipolar plate material
		180	0.35	1600	10-50			
2012	[19]	150	0.2	2,000	1.82	In-house	Y	Postmortem analysis into the growth of Pt particles, and H3PO4 loss values estimated
		150	0.2	12,000	4.2			
		150	0.2	15,000	3.3			
		150	0.2	17,860	3.75			
2012	[20]	160	0.3	2,000	2.4	In-house	N	Investigated different PBI polymers
		160	0.3	2,400	6.4			
		160	0.3	2,000	23.2			
2013	[21]	160	0.3	1,400	1.59	In-house	N	Investigated different PBI polymers
		160	0.3	1,600	3.9			
		160	0.3	800	110.1			
2013	[22]	160	0.2	950	8.6	BASF Celtec® P2100		Reference MEA with load and thermal changes
		160	0.2	540	6			
		160	0.2	210	7			
		180	0.2	400	19			
		160	0.4	850	4.5			
2014	[23]	180	0.2	2,350	5.23	In-house	N	
2015	[24]	150	0.5	1,640	15.3	PBI/ phosphoric acid sol-gel MEA from BASF	N	Also investigated intermittent operation
2016	[25]	200	0.2	1,450	82	In-house	N	Investigated different PBI polymers
		200	0.2	1500	27			
		200	0.2	1500	129			

2016	[26]	160	0.3	3,000	4.7	Dapozol®-G55	Y	Varying O ₂ and air mixtures
		160	0.3	9,000	3			
		160	0.3	3,000	-2			
2016	[4]	160	0.2	4,400	5.6	In-house	N	Investigated different PBI polymers
		160	0.2	13,000	10.7			
		160	0.2	4,400	8.8			
		160	0.2	13,000	5			
2018	[27]	180	0.2	3,508	52.8	In-house	N	Investigated effect of different gas diffusion layers and catalyst loadings
		180	0.2	3,508	23.7			
		180	0.2	3,508	11.1			
		180	0.2	2,086	10.8			
		180	0.2	2,084	38.2			
		180	0.2	3,430	26.7			
		180	0.2	5,512	12.5			
2018	[28]	160	.2	100	331	In-house	N	

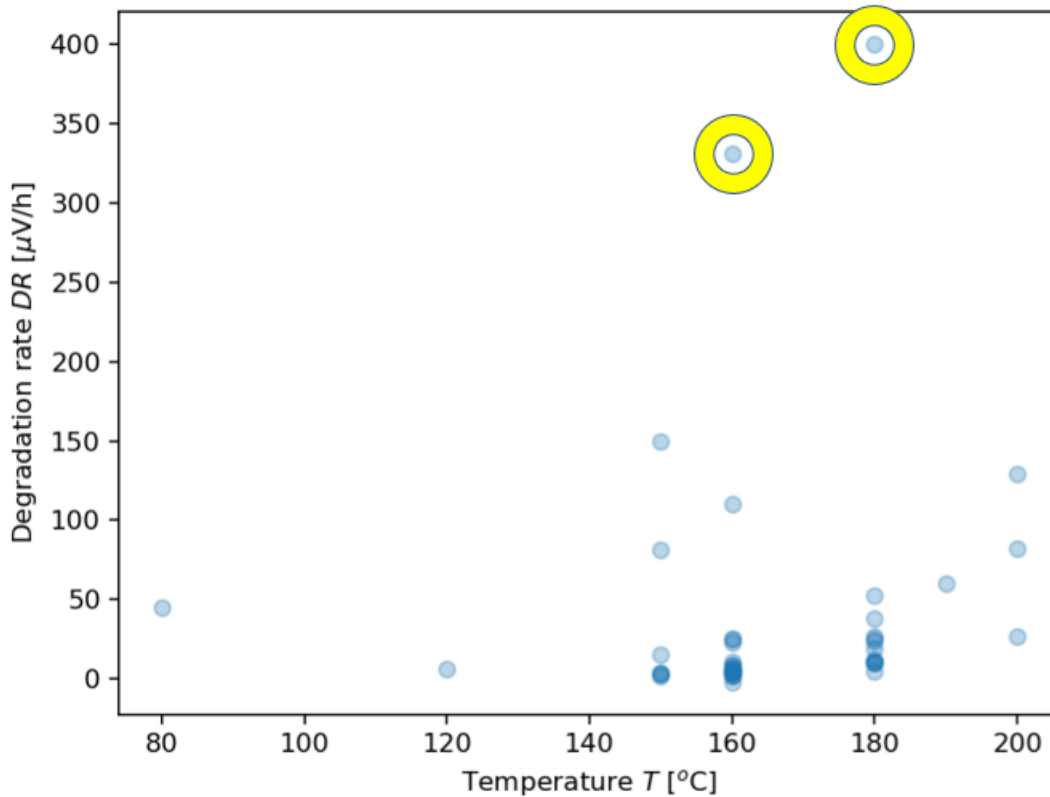


Figure 1.2 – Reported voltage degradation rates with hydrogen/air at 0.2 A/cm² and temperature of 160, 180 and 200°C, Yellow circles indicate outliers.

In this analysis, only studies reporting results of phosphoric acid doped PBI based MEAs running pure hydrogen at the anode and air or oxygen at the cathode were included. This is important to note, as existing data for HT-PEM degradation using reformates or with added fuel impurities have not been included in Figure 1.2. These studies were omitted because the inclusion of impurities within fuel can lead to increased degradation rates that would obscure the trend illustrated in Figure 1.2, with minimum degradation in the temperature range of 120-160°C and significantly greater voltage loss at lower and higher temperatures. Also, it is pertinent to mention that a very large body of literature exists addressing the degradation behavior of low-temperature PEM fuel cells and the associated impacts on cell components such as the membrane, gas diffusion

layer (GDL), and bipolar plates (e.g., [29]-[31]). However, because of the fundamental differences in materials and operating conditions between the LT-PEM and HT-PEM systems [32], it is expected that there is little commonality in the specific loss mechanisms involved, and prior LT-PEM results cannot be directly applied to the outcomes of the present research. Alternative versions of Figure 1,2 can be found in the Appendix – Chapter 1.

Based on the data in Table 1.1 and Figure 1.2, general trends of increasing degradation rates with both increasing temperature and current density can be observed. However, there is a great deal of variability in the data, as many of the cited studies fabricated in-house MEAs with varying materials, doping levels, membrane size, and PBI polymer structures. Further complicating the comparison of the data are variations in testing procedures and hardware configurations with custom test stands, and differing cell assemblies. Many of the reported data included in Table 1.1 are repeat experiments conducted within the same study. However, these repeat runs were rarely designed to establish measurement uncertainty, but rather used as comparison tests at similar conditions or with alternate MEA chemistries. As illustrated in Figure 1.1, there is a clear lack of published data at both higher temperatures and current densities in the targeted range for this study, 200°C and 0.4 to 0.6 A/cm². The cited data sources from literature indicate that voltage degradation rates increase with both current density and temperature, but there is not a consistent trend due to the wide variations in test methods, MEA fabrication techniques, and test conditions employed. Moreover, there is very little known about degradation at relatively high temperatures (> 180°C) where we are targeting our operating parameters to enable the use of propane reformat (and ultimately syngas/biogas reformat) with high expected CO concentration. This research addresses these limitations by conducting multiple repeatable 200+ hour tests to establish a baseline. Figure 1.1, illustrating the trends in parameters across different studies,

highlights the need for further investigation at the higher current density and temperature regime explored in this paper.

Fuel Cell Fundamentals

Fuel cell systems operate using hydrogen as fuel combined with oxygen in an electrochemical reaction to produce electricity. This reaction is the opposite of an electrolysis reaction and involves the recombination of oxygen and hydrogen to produce electrical energy see (Equation 1.1):



In the typical case of proton exchange membrane (PEM) fuel cells, an electrolyte is positioned between anode and cathode sides of the cell (Figure 1.3).

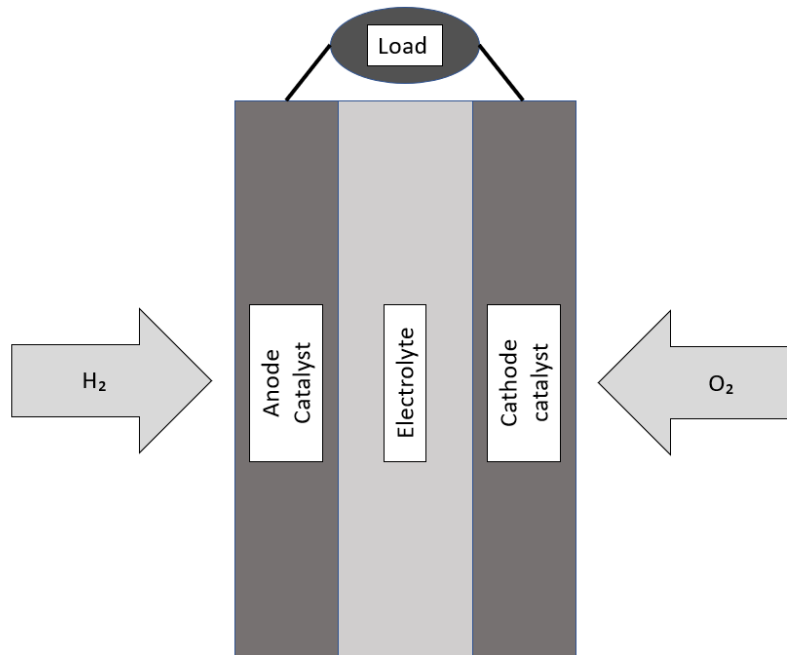


Figure 1.3: Cross-sectional view of fuel cell function diagram

As the H₂ flows to the anode it is ionized and creates two hydrogen protons and releases electrons. The ionization process is assisted by the inclusion of a catalyst which can vary in composition depending on application and desired use. An important quality of the electrolyte is the ability to allow protons but not electrons to pass through. With the hydrogen protons able to pass through the membrane they can reach the cathode side reacting with the oxygen:



With the reaction in Eq. 1.2 requiring electrons, there needs to be an external path available to provide transport of the electrons from the anode to the cathode, as they cannot pass through the electrolyte. This external route provides a flow of electrons that with an applied load can be used to do work.

HT-PEM Fuel Cell Stands

With PEM fuel cell operation there are many components which are required for operation and testing beyond the cell itself. During operation in both laboratory and commercial settings there are a variety of balance-of-plant and auxiliary components that can have an impact on the function of a fuel cell system. Three different testing setups were used over the course of this work.

Stand 1

The first stand used was a commercially available stand from Hydrogenics. This stand featured mass flow controllers, back-pressure control, heated gas lines and reactant humidification. The work in Chapter 3 utilized this stand, but unfortunately suffered issues with reliability. After the completion of the initial round of testing, this stand was retired rather than repaired primarily due to its age which led to lack of replacement parts and ongoing reliability issues.

Stand 2

As a result of the reliability issues experienced with Stand 1, a second test apparatus was developed in-house to enable long duration experiments. The work presented in Chapters 2, 4 and 6 is based on testing on Stand 2. Figure 1.4 shows an electro-pneumatic diagram of the stand layout. The dashed lines represent electrical connections while the solid lines represent the gas lines. Each sub-assembly is color coded and referenced in the legend. This testing setup allowed for the control of gas flow, pressure, temperature and current draw as well as providing over-temperature and over-pressure protection in case of emergency. This setup also featured the ability to collect product water from both anode and cathode exhaust streams and high frequency resistance (HFR) measurements. There are several subsystems in the stand diagram, both the anode and cathode subsystems are very similar allowing for the control of gas flow and pressure to be regulated. The electrical system encompasses the load bank used to draw a load from the cell in addition to the power for stand components and HFR capabilities. The nitrogen system is included for startup-shutdown purposes and for safety in case of a stand or cell malfunction.

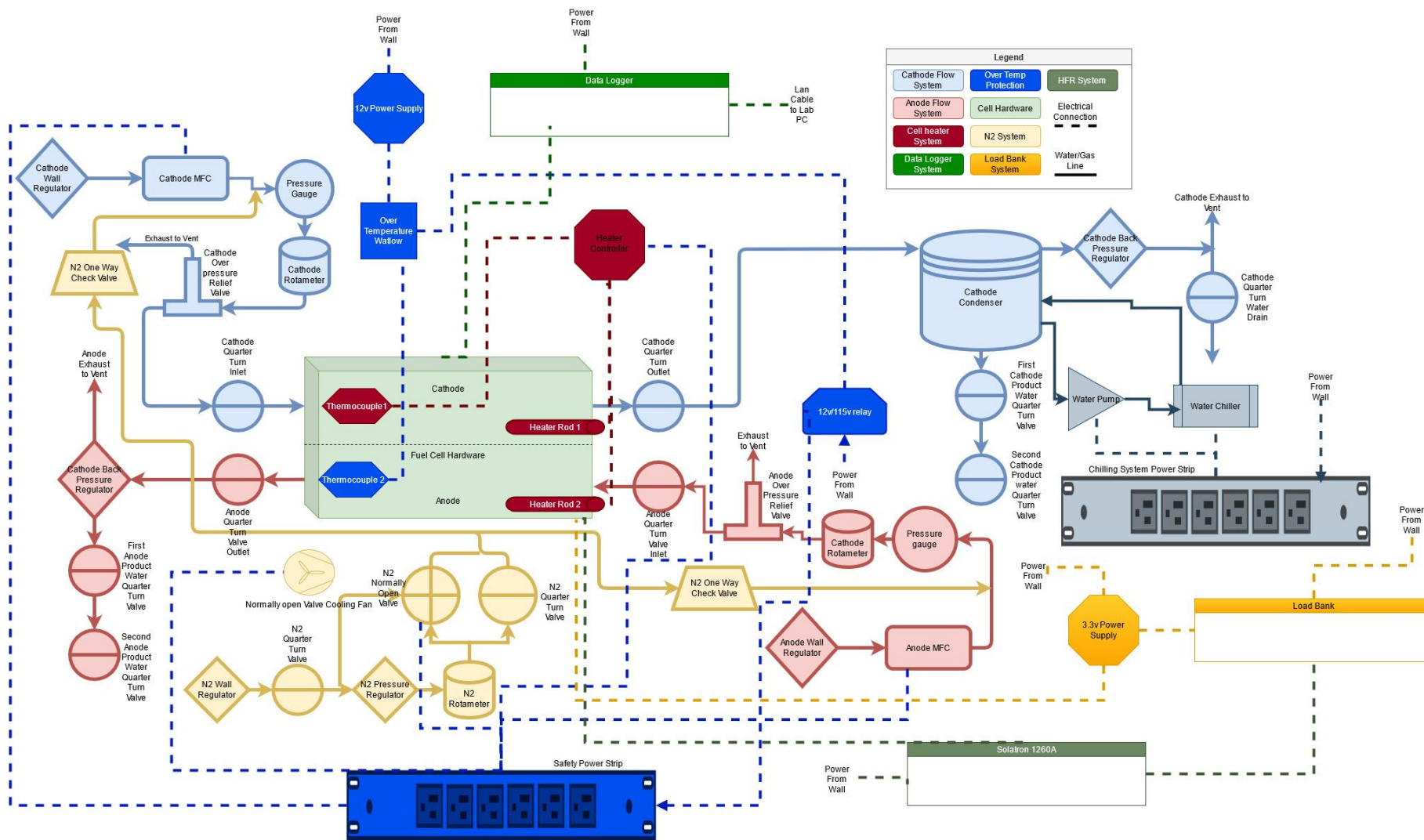


Figure 1.4: Electro-pneumatic setup of Stand 2

Stand 3

Stand 3 was a commercially available stand produced by Greenlight model G40 and was in many ways similar to Stand 1 with the same capabilities but with generally newer components. This stand was used to test the role of water on MEA performance and degradation, with results presented in Chapter 5. With the failure of irreplaceable components on stand 1 it was necessary to transition to another setup.

Citations Chapter 1

- [1] Barbir F. Fuel Cell Applications. PEM Fuel Cells, 2013; 373–434. doi: 10.1016/B978-0-12-387710-9.00010-2.
- [2] Daud WRW, Rosli RE, Majlan EH, Hamid SAA, Mohamed R, and Husaini T. PEM fuel cell system control: A review. Renewable Energy. 2017; 113:620-638. doi: 10.1016/j.renene.2017.06.027. <https://doi.org/10.1016/j.renene.2017.06.027>
- [3] Jalani NH, Dunn K, and R. Datta. Synthesis and characterization of Nafion®-MO₂ (M = Zr, Si, Ti) nanocomposite membranes for higher temperature PEM fuel cells. Electrochim. Acta. 2005; 51.3:553–560. doi: 10.1016/j.electacta.2005.05.016.
- [4] Products – High Temperature PEM Products – Advent Technologies. <https://www.advent-energy.com/products-high-temperature-pem-products/> (accessed Aug. 01, 2021).
- [5] Waller MG, Walluk MG, and Trabold TA. Design of an integrated propane fuel reformer and fuel cell system for unmanned aerial system (UAS) applications. STRATUS 2016 - Proceedings of 2016 IEEE Systems and Technologies for Remote Sensing Applications Through Unmanned Aerial Systems, 2017; 1–4, doi: 10.1109/STRATUS.2016.7811135.
- [6] Ming Q, Healey T, Allen L, and Irving P. Steam reforming of hydrocarbon fuels. Catal. Today. 2002; 77: 51–64. doi: 10.1016/S0920-5861(02)00232-8.

- [7] Araya SS, Zhou F, Liso V, Sahlin SL, Vang JR, Thomas S, Gao X, Jeppesen C, and Kær SK. A comprehensive review of PBI-based high temperature PEM fuel cells. *Int. J. Hydrogen Energy*. 2016;41(46): 21310-21344.
<https://doi.org/10.1016/j.ijhydene.2016.09.024>
- [8] Tseng P, Lee J, and Friley P. A hydrogen economy: opportunities and challenges. *Energy*. 2005; 30.14:2703–2720. doi: 10.1016/J.ENERGY.2004.07.015.
- [9] Søndergaard T, Cleemann LN, Becker H, Aili D, Steenberg T, Hjuler HA, Seerup L, Li Q, and Jensen JO. Long-term durability of HT-PEM fuel cells based on thermally cross-linked polybenzimidazole. *J. Power Sources*. 2016;342:570–578. doi: 10.1016/j.jpowsour.2016.12.075.
- [10] Waller MG, Walluk MR, and Trabold TA. Operating envelope of a short contact time fuel reformer for propane catalytic partial oxidation. *J. Power Sources*. 2015; 274:149-155.
<https://doi.org/10.1016/j.jpowsour.2014.10.025>
- [11] Eberhardt SH, Toulec M, Marone F, Stampanoni M, Büchi FN, and Schmidt TJ, Dynamic operation of HT-PEFC: In-operando imaging of phosphoric acid profiles and (re)distribution, *J. Electrochem. Soc.* 2015;162.3:F310–F316. doi: 10.1149/2.0751503jes.
- [12] Hu J, Zhang H, Zhai Y, Liu G, and Yi B. 500 h Continuous aging life test on PBI/H₃PO₄ high-temperature PEMFC. *Int. J. Hydrogen Energy*. 2006;31:1855–1862doi: 10.1016/j.ijhydene.2006.05.001.
- [13] Liu G, Zhang H, Hu J, Zhai Y, Xu D, and Shao Z-G, Studies of performance degradation of a high temperature PEMFC based on H₃PO₄-doped PBI. *J. Power Sources*. 2006;162.1;pp. 547–552. doi: 10.1016/j.jpowsour.2006.07.008.
- [14] Yu S, Xiao L, and Benicewicz BC. Durability studies of PBI-based high temperature

- PEMFCs. *Fuel Cells* 2008;3:165–174, 2008, doi: 10.1002/fuce.200800024.
- [15] Schmidt TJ and Baurmeister J. Properties of high-temperature PEFC Celtec®-P 1000 MEAs in start/stop operation mode. *J. Power Sources*, 2008;176.2:428–434. doi: 10.1016/j.jpowsour.2007.08.055.
- [16] Wannek C, Kohnen B, Oetjen H-F, Lippert H, and Mergel J. Durability of ABPBI-based MEAs for high temperature PEMFCs at different operating conditions. *Fuel Cells*. 2008;8.2:87–95. doi: 10.1002/fuce.200700059.
- [17] Modestov AD, Tarasevich MR, Filimonov VY, and Zagudaeva NM. Degradation of high temperature MEA with PBI-H₃PO₄ membrane in a life test. *Electrochim. Acta*. 2009;54.27:7121–7127. doi: 10.1016/J.ELECTACTA.2009.07.031.
- [18] Hartnig C and Schmidt TJ. On a new degradation mode for high-temperature polymer electrolyte fuel cells: How bipolar plate degradation affects cell performance. *Electrochim. Acta*. 2011;56.11:4237–4242. doi: 10.1016/j.electacta.2011.01.088.
- [19] Oono Y, Sounai A, and Hori M. Long-term cell degradation mechanism in high-temperature proton exchange membrane fuel cells. *J. Power Sources*, 2012;210:366–373. doi: 10.1016/j.jpowsour.2012.02.098.
- [20] Yang J, Li Q, Cleemann LN, Xu C, Jensen JO, Pan C, Bjerrum NJ, He R. Synthesis and properties of poly(aryl sulfone benzimidazole) and its copolymers for high temperature membrane electrolytes for fuel cells. *J. Mater. Chem*. 2012;22.22:11185–11195doi: 10.1039/c2jm30217a.
- [21] Yang JS, Cleemann LN, Steenberg T, Terkelson C, Li QF, Jensen JO, Hjuler HA, Bjerrum NJ, He RH. High molecular weight polybenzimidazole membranes for high temperature PEMFC. *Fuel Cells*. 2013;14.1:7–15. doi: 10.1002/fuce.201300070.

- [22] Galbiati S, Baricci A, Casalegno A, and Marchesi R. Degradation in phosphoric acid doped polymer fuel cells: A 6000 h parametric investigation. *Int. J. Hydrogen Energy*. 2013;38.15:6469–6480. doi: 10.1016/j.ijhydene.2013.03.012.
- [23] Molle MA, Chen X, Ploehn HJ, Fishel KJ, and Benicewicz BC. High polymer content 3,5-pyridine-polybenzimidazole copolymer membranes with improved compressive properties. *Fuel Cells*. 2014;14.1:16–25. doi: 10.1002/fuce.201300202.
- [24] Lang S, Kazdal TJ, Kühl F, and Hampe MJ. Experimental investigation and numerical simulation of the electrolyte loss in a HT-PEM fuel cell. *Int. J. Hydrogen Energy*. 2015; 40.2:1163–1172. doi: 10.1016/j.ijhydene.2014.11.041.
- [25] Aili D, Zhang J, Jakobsen MTD, Zhu H, Yang T, Liu J, Forsyth M, Pan C, Jensen JO, Cleemann LN, Jiang SP, Li Q. Exceptional durability enhancement of PA/PBI based polymer electrolyte membrane fuel cells for high temperature operation at 200 °C. *J. Mater. Chem. A*. 2016;4.11:4019–4024. doi: 10.1039/C6TA01562J.
- [26] Rastedt M, Pinar FJ, Wagner P, Garcia HR, Steenberg T, Hjuler HA, Paidar M, and Bouzek K. Ultralow degradation rates in HT-PEM fuel cells. *ECS Transactions*. 2016;75.14:301. <https://doi.org/10.1149/07514.0301ecst>
- [27] Kannan A, Li Q, Cleemann LN, and Jensen JO. Acid distribution and durability of HT-PEM fuel cells with different electrode supports. *Fuel Cells*. 2018;18.2:103–112. doi: 10.1002/FUCE.201700181.
- [28] Yao D, Jao T-C, Zhang W, Xu L, Xing L, Ma Q, Xu Q, Li H, Pasupathi S, and Su H. In-situ diagnosis on performance degradation of high temperature polymer electrolyte membrane fuel cell by examining its electrochemical properties under operation. *Int. J. Hydrogen Energy*. 2018;43.2:21006–21016. doi: 10.1016/j.ijhydene.2018.09.103.

- [29] Wei T, Song W, Yang X, Zhang E, Huang Z, Zhang H, Yu H, and Shao Z. Degradation behavior of proton exchange membrane fuel cells under hydrogen starvation in freezing conditions. *J. Power Sources*. 2022; 521: 230898.
<https://doi.org/10.1016/j.jpowsour.2021.230898>
- [30] Yuwei P, Wang H, and Brandon NP. Gas diffusion layer degradation in proton exchange membrane fuel cells: Mechanisms, characterization techniques and modelling approaches. *J. Power Sources*. 2021; 513: 230560. <https://doi.org/10.1016/j.jpowsour.2021.230560>
- [31] Chu T, Xie M, Hao J, Xu Z, Li Y, Yang D, Li B, Ming P, and Zhang C. Degradation analysis of the core components of metal plate proton exchange membrane fuel cell stack under dynamic load cycles. *Int. J. Hydrogen Energy*. 2022; 47(11): 7432-7442.
<https://doi.org/10.1016/j.ijhydene.2021.12.068>
- [32] Rosli RE, Sulong AB, Daud WRW, Zulkifley MA, Husaini T, Rosli MI, and Haque MA. A review of high-temperature proton exchange membrane fuel cell (HT-PEMFC) system. *Int. J. Hydrogen Energy*. 2017; 42(14): 9293-9314.
<https://doi.org/10.1016/j.ijhydene.2016.06.211>

Chapter 2 – Optimization of Membrane Electrode Assembly (MEA) Fabrication

Overview of Membrane Electrode Assembly

Comprised of multiple layers, the membrane electrode assembly (MEA) is a fuel cell's central component. In use with HT-PEM cells these are often referred to as "5 layers MEAs" this is due to the 5 constituent layers which make up the assembly. These layers are the gas diffusion layer, the catalyst layer, and the membrane itself see figure 2.1 below.

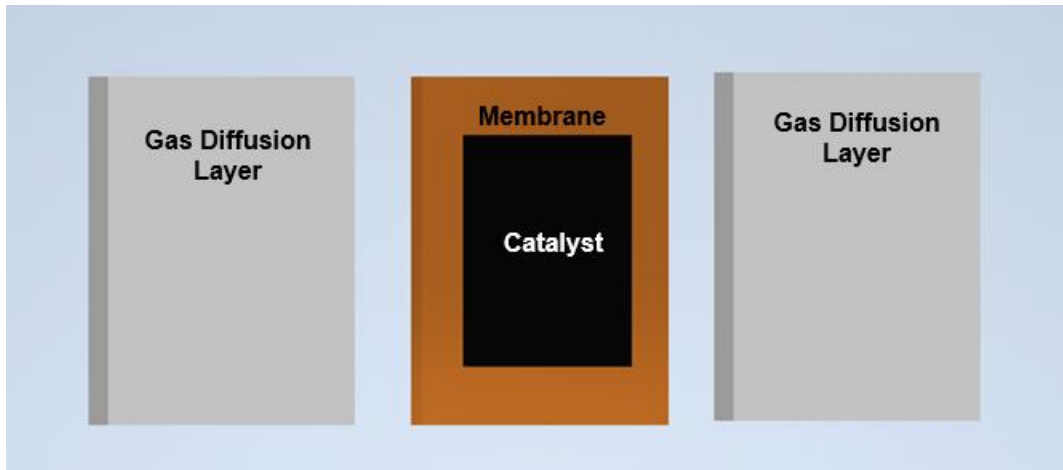


Figure 2.1: MEA diagram

The outermost layer is the gas diffusion layer which is typically either a carbon cloth consisting of woven fiber or a carbon paper. The gas diffusion layer provides a structure for the catalyst, ensures good electrical contact with the cell hardware, and helps to evenly distribute the reactants onto the membrane. Working inwards the next layer is a catalyst layer which can either be applied to the gas diffusion layer or directly to the membrane. The purpose of the catalyst layer is to help facilitate the reaction. In the interest of preserving catalyst material and keeping costs down it is

bonded to a carbon support which has the effect of increasing surface area while decreasing total platinum loading. At the center of the assembly is the membrane itself. In HT-PEM the membrane is made of polybenzimidazole (m-PBI) and doped in a phosphoric acid generally in the ortho-phosphoric acid phase and at an 85 wt.% concentration.

Literature Review of MEA Fabrication Processes

In a fabrication process similar to LT-PEM MEAs, the proton-conducting membrane, electrodes, gas diffusion layers and sub gaskets are often hot-pressed together. The parameters relevant to the hot-pressing operation can have a significant impact on the ultimate performance of the fuel cell, in addition to influencing process reliability and repeatability. There is little published on optimal conditions of the hot-pressing process, with significant variations of conditions being reported. Several researchers have reported successful hot-pressing parameters; however, these published conditions cover wide ranges of temperature, time, and pressure. In work on catalyst layer binders, Su et al. [1] pressed the MEA at 130°C, while Søndergaard et al. [2] used a temperature of 200°C for the MEA hot-press in a study of long-term HT-PEM durability. A wide range of press times have also been reported. For example, Morfopoulou et al. [3] used a press time of 15 minutes compared with Share et al. [4] who tested press times as short as 15 seconds in a study similar to the present one on optimizing hot pressing conditions.

The pressures tested in this work range from the average found among prior studies to significantly higher than those values cited in literature. It is hypothesized that HT-PEM MEA performance may benefit from increased pressure during the hot-press process, providing stronger adhesion between the layers, increasing the mechanical stability of the MEA and lowering contact

resistance. This hypothesis is based in part on the difference between the pressing of high temperature and low temperature MEAs. The material differences between the two systems necessitates a different approach to the pressing process. It is understood that Nafion® can undergo a thermal transition leading to an increase in the adhesion strength with temperature, time, and pressure, as reported by Froelich et al. [5]. The materials used in HT-PEM MEAs do not undergo a transition within the same temperature range, leading to the hypothesis of potential benefits with increasing pressure. It is, however, also important to recognize that alternatives to a hot-pressing process in the MEA fabrication have been explored. One alternative involves eliminating the hot pressing operation altogether, and simply placing the layers within the cell assembly (Kannan et al. [6]). This has the benefit of simplifying the fabrication process and has been reported in several studies. Ultrasonics have also been used as an alternative to hot pressing as a way to seal the MEA, with Walczyk [7] identifying a reduction in the cost of pressing operation through the use of ultrasonic welding.

MEA Sample Preparation

The MEA samples were prepared by coating two 25.4 mm square gas diffusion layer (GDL) samples with a catalyst simulating slurry, placing these coated electrodes on either side of a phosphoric acid doped polybenzimidazole (PBI) sample, and hot pressing the assembly together. The sample hot pressing was performed with two 102 × 152 mm 6061 aluminum plates with a total of four embedded 160W heater rods. Two proportional-integral-derivative (PID)-controlled heater rods were located in both the top and bottom press platens. The applied pressure was controlled by a manual jack with attached pressure gauge. After hot pressing, samples were removed from the press and immediately transferred to a nitrogen purged glove box, allowing the samples to cool in a humidity-controlled environment.

A catalyst-on-carbon support is typically used for MEA fabrication. Due to the large number of MEA samples prepared in this study to optimize hot-press conditions, a carbon support without catalyst was used to reduce cost. Selected control tests were also performed on samples with and without a platinum catalyst and it was determined that conductivity, internal bond test (IBT), and thickness measurements of samples without catalyst behaved similarly to samples containing catalyst. The MEA sample fabrication process began with 25.4 mm square samples of AvCarb MGL190, a commercially available GDL material. To create a uniform coating of the simulated catalyst, a slurry was prepared using a mixture of deionized water, isopropyl alcohol, PTFE dispersal fluid, and a carbon support (XC-72R). This slurry was prepared in a vial and mixed using a 30 kHz sonicator, then applied to the GDL using a brush in a series of thin coats until the correct coverage had been achieved. Carbon support loading on the MEA samples was determined using a total anticipated coverage of 1.8 mg/cm² platinum on the MEA, with areal densities on the cathode and anode of 1 mg/cm² and 0.8 mg/cm², respectively. An assumption was made that in our case this level of catalyst loading would be achieved using a 20 wt.% platinum on carbon material.

All MEA samples were prepared following the above procedure and then assembled under varying conditions in the hot press. Three factors were varied within these tests: times of 1,3,5, and 10 minutes; temperatures of 140°C, 180°C, and 200°C; and pressure of 7.72, 23.17, 46.34, and 92.67 MPa. Two MEA samples were prepared for each combination of time, temperature, and pressure. After the samples had been pressed, they were placed in a nitrogen purged glove box to cool.

MEA Experimental Methods

The MEA samples were placed in a Solartron Analytica 12962A sample holder connected to a 1260A frequency response analyzer, also within a nitrogen environment. Resistance and thickness measurements were acquired in triplicate for each sample. The value for resistance was multiplied by the area of the sample to compute the area specific resistance (Equation 2.1).

$$\begin{aligned} \text{Area Specific Resistance } [\Omega\text{cm}^2] &= \text{Resistance } [\Omega] \times \text{Area Sample } [\text{cm}^2] \quad [\text{eq 2.1}] \\ \text{ASR} &= R \times A \end{aligned}$$

After completing the resistance measurement, samples were moved to a Scott type internal bond tester to measure the strength of the adhesion between the MEA layers. As this was a destructive test, it was performed last and resulted in the delamination of the sample. This measurement used a pendulum to peel apart or delaminate the samples and was measured in units of J/cm². Although standards for adhesion strength measurement usually involve units of N/mm² or MPa (e.g., [8]), we directly used the measurements from the Scott internal bond tester without further unit conversion, as a means of comparing relative bond strength of the different MEA samples. A scanning electron microscope (SEM) was used with energy dispersive X-ray spectroscopy (EDX) to further characterize the MEA samples and the associated effects of pressing conditions. MEA samples were sliced in half and then placed within a custom fabricated sample holder that allowed imaging of the sample in cross section, exposing the different layers of the MEA. Measurements in the SEM were made at a 10 keV accelerating voltage. A box scan function was used to perform the EDX scans for a quantitative analysis, with each sample being measured three times. For testing polarization performance of functional 25.2 cm² MEA, a set of fuel cell hardware was used with gold plated current collectors, Poco-sealed graphite flow fields

in a quad serpentine pattern, and aluminum endplates with embedded heater rods torqued to 5.65 Nm (50 in-lbs.) using 8 bolts. A custom-built test stand constructed of several mass flow controllers, load bank, and heater controllers was used for all fuel cell testing. Pure hydrogen and air without external humidification were introduced to the cell with stoichiometric ratio of 1.5 and 2 for the anode and cathode, respectively.

Conductivity and Bond Strength Results

Figure 2.2 illustrates the effect of hot-press time on resistance for the 25.4 mm square samples fabricated without Pt catalyst. It is worth noting that this figure includes all hot-pressing conditions, only differentiating for time. Thus, at the 10-minute mark, there are multiple data points for various temperatures at both 7.72 and 92.67 MPa. Figure 2.1 presents only the effect of time in the press, concealing the effects of pressure and temperature. From this data presentation, there is an apparent trend with a minimum resistance occurring at moderate times between the 4 and 6 minutes.

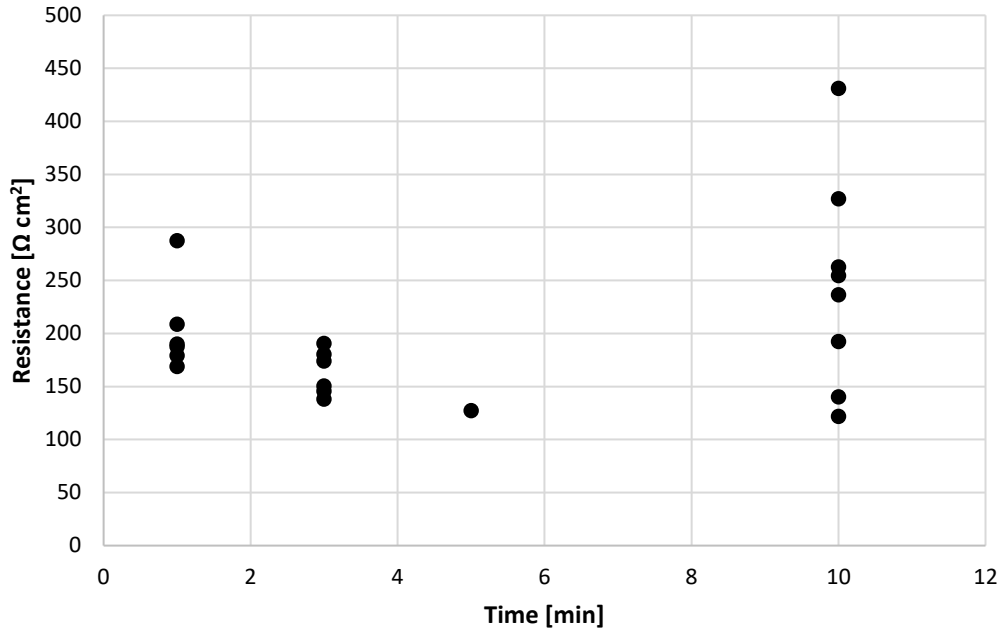


Figure 2.2. Analysis of resistance vs. hot-press time for all temperature and pressure conditions

A total of 46 individual 25.4 mm square samples were prepared and tested, but each testing condition was run in duplicate with the average of these measurements plotted to simplify the presentation of the data. Further reducing the number of data points in the figures are hot pressing failures. Some combinations of parameters did not produce a properly pressed MEA and constituted a process failure. Each instance of failure to properly press an MEA sample was recorded and removed from the data set.

As mentioned above, the two-dimensional presentation in Figure 2.2 conceals many of the interactions among the three independent variables (time, temperature and pressure). However, the three-dimensional plots in Figure 2.3 elucidate these interactions through measurements of adhesion strength (subplots A, C and E) and resistance (subplots B, D and F). Each subplot represents different hot-press temperatures of 140, 180 and 200°C. For the internal bond tester

(IBT) measurements of adhesion strength, larger values indicate greater force required to delaminate the samples.

Ignoring the 1 minute, 7.72 MPa value in Figure 2.3A (140°C) that may be an outlier, there seems to be a general trend toward greater adhesion strength at higher hot-press pressure, temperature, and time. This trend in adhesion strength with respect to pressure and time is most evident in Figure 2.3E. However, with increasing temperature there is an overall increase in the average adhesion strength. Figures 2.3B, 2.3D and 2.3F show the area specific resistance measurements for the MEA samples (units of $\Omega \text{ cm}^2$), with a lower value considered beneficial for fuel cell performance. The MEA resistance trends toward an overall increase with increasing temperature. In Figure 2.3D, the downward trend towards the front right corner shows a decrease in resistance with increasing hot-press time and decreasing pressure. Alternatively, Figure 2.3F trends toward the front center of the plot with the lower resistance region corresponding to a moderate pressing time of around 3 minutes and lower pressures.

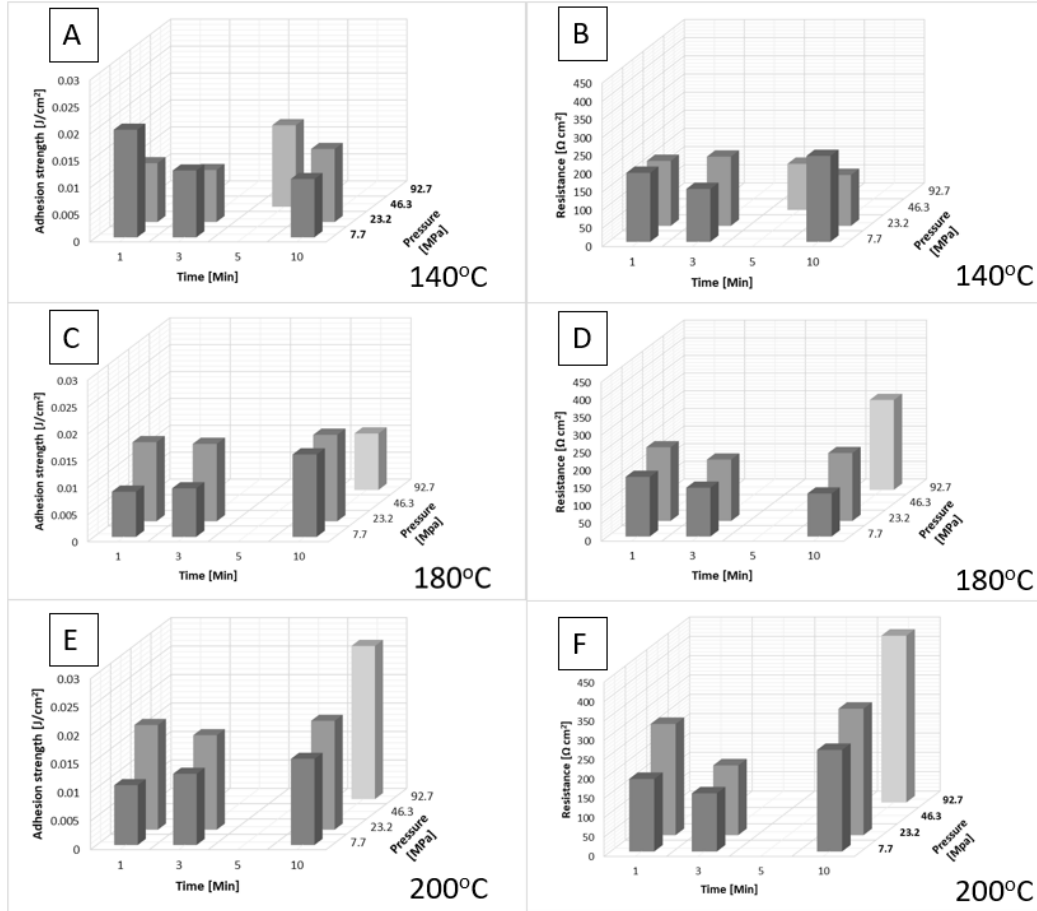


Figure 2.3. Effects of hot-press pressure, time and temperature on adhesion strength and resistance

(A) bond strength at 140°C; (B) resistance at 140°C; (C) bond strength at 180°C; (D) resistance at 180°C; (E) bond strength at 200°C; (F) resistance at 200°C

In the early stages of the project, it was expected that there would be a trade-off between reducing the contact resistance between MEA layers, which could be achieved through increasing pressing time, temperature, and pressure, and a loss of conductivity of phosphoric acid (PA) due to dehydration of the acid at higher temperatures. The boiling point of PA is known to be 160°C, and it is interesting to note that while the 140°C plot (Figure 2.3B) indicates minimal variations in resistance, both the 180°C (Figure 2.3D) and 200°C (Figure 2.3F) conditions show significant variations within each data set.

Impact of Pressing Conditions on Repeatability

Occasionally the MEA samples would delaminate within the press, as a result of MEA layers failing to adhere internally and pulling apart, or the sample adhering to the press platen and delaminating the GDL when removed. In the present study, either outcome was considered a press failure and the failure was recorded. Figure 2.4 shows these failures as a percentage of total samples attempted at each pressure. With a 0% failure rate, 23.17MPa was the most reliable pressure attempted. Looking at the effect of press time on failure rate, Figure 2.5 shows a minimum of 14% failure rate at 3 minutes, with the rate of failure greatest (40%) at 5 minutes.

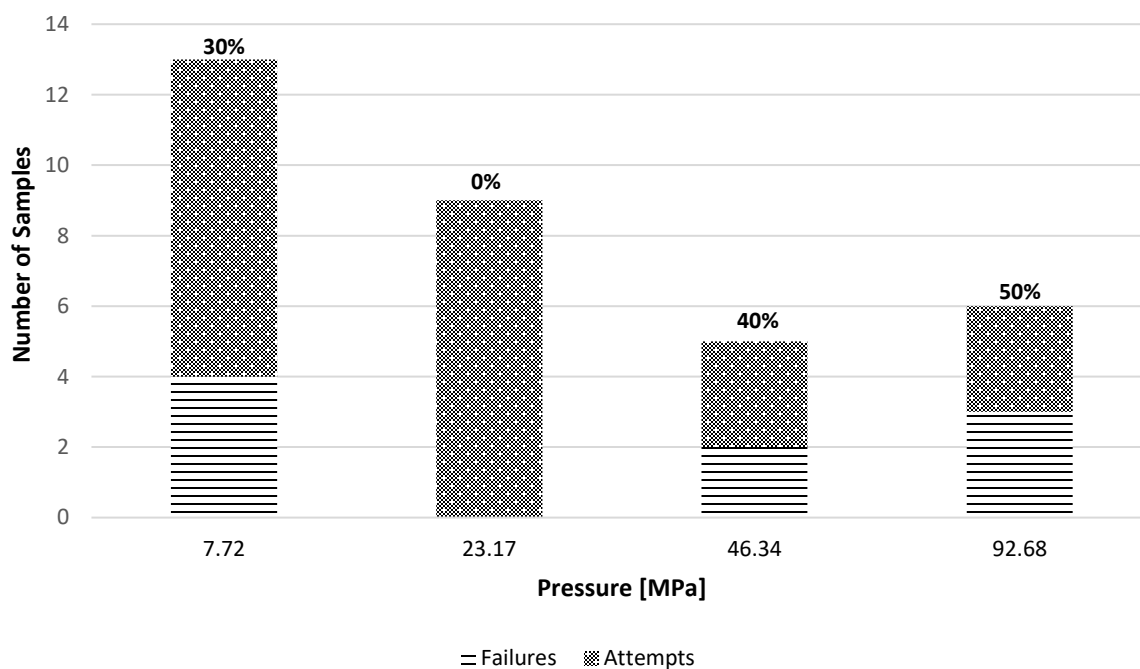


Figure 2.4. Number of MEA samples resulting in failure during hot-pressing at different pressures

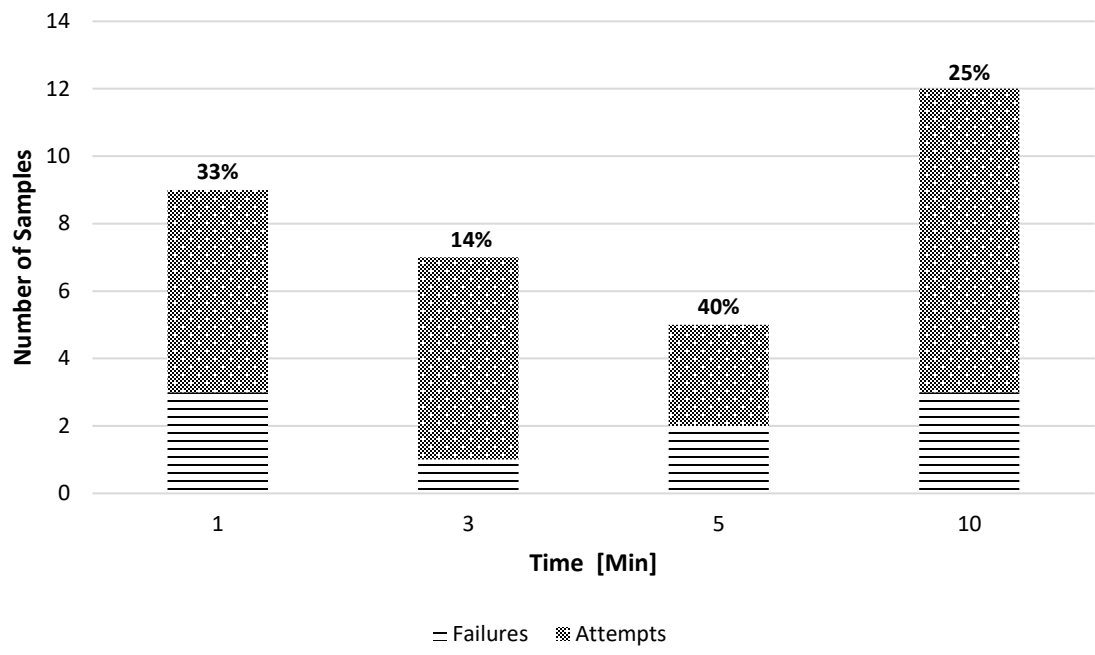


Figure 2.5. Number of MEA samples resulting in failure during hot-pressing for different times

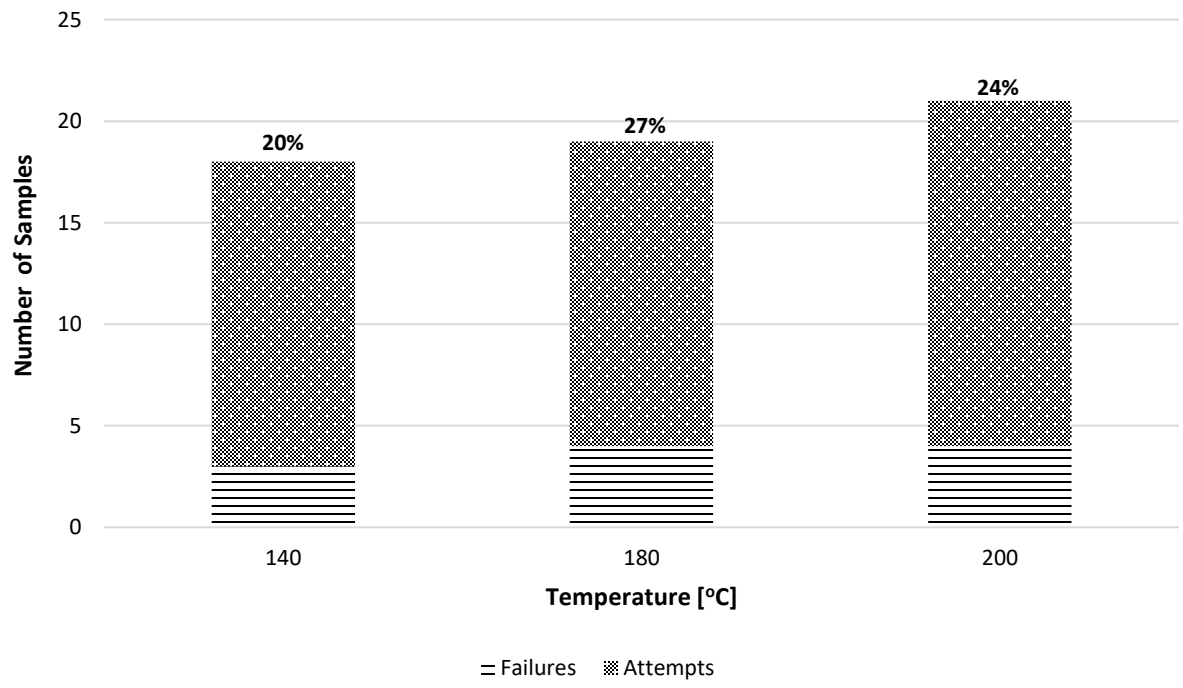


Figure 2.6. Number of MEA samples resulting in a failure during hot-pressing at different temperatures

The difference in failure rate between 3 and 5 minutes may be explained by the order of MEA sample pressing. In order to minimize the effect of pressing order on failure rates MEA samples were pressed in order of temperature, from low to high. Figure 2.6 may validate this approach, showing minimal change in failure rate with increasing temperature indicating that the hot-press platens did not deteriorate during the bulk of MEA sample preparation. Between each MEA sample pressed, the press platen was cleaned with an abrasive pad and water, and then wiped with isopropyl alcohol. This process was repeated throughout the entirety of the sample set. The condition of 46.34 MPa and 5 minutes was unique, as MEAs were prepared with these process conditions after all other samples, and after the press had been used on several other experiments with full size MEAs. After the full-size MEA experiments, the press platens had become visibly scored, and it is possible that this change influenced the failure rate at the 46.34 MPa and 5-minute condition. This condition was added at the latter stages of the experimental campaign to include more resolution in the data.

As stated above, when pressing the MEAs, failures occurred due to delamination in two different ways. In Mode 1, the MEA layers failed to adhere internally, pulling apart in the press. In Mode 2, the MEA layers were firmly pressed together, however, one of the GDL's would remain adhered to a platen and would rip if an attempt was made to remove it, delaminating the GDL in sections. It was observed that during the manufacturing of the samples with less aggressive conditions (i.e., relatively low pressure, temperature, and time), the failure was dominated by the Mode 1 where the MEA components were not sufficiently adhered and pulled apart. This differed from failures observed at more aggressive conditions where the MEAs were stuck to the press platen. This is important to note, as with an improved setup (e.g., PTFE coated aluminum platens)

Mode 2 failures are likely avoidable, while Mode 1 failures represent an inability to properly adhere the MEA components under the conditions tested.

Identification of Optimal Pressing Conditions

A press time of 5 minutes was selected to minimize the MEA resistance as seen in Figure 2.2, given the assumption that changing the hot press platen material would reduce the elevated failure rate relative to the 3-minute hot-press time (Figure 2.5). Three data points were tested at these conditions. The trend seen in the Figure 2.3 resistance plots was an increase in resistance with increasing pressure. Based on the failure rate data presented in Figure 2.4, 23.1MPa was the lowest pressure that could be applied and still achieve a reliable adhesion of the MEA components. Raising the pressing temperature increased the strength of the MEA layer adhesion while the resistance also increased. A value of 170°C was therefore selected as the optimal pressing temperature.

Impact of Pressing Conditions on Electrolyte Hydration

With the known boiling point of phosphoric acid of 160°C, some of the deleterious effects on resistance of the hot-pressing process at higher temperatures may be due to the dehydration of phosphoric acid. As phosphoric acid dehydrates, it forms different polyphosphoric acid compounds and becomes less conductive, possibly leading to an increase in MEA resistance (Schechter and Savinell [9]). To test this hypothesis, three new 25.4 mm square MEA samples were prepared at different hot-press conditions, including one considered as most aggressive in

regards to phosphoric acid dehydration (200°C, 92.67 MPa, 10 minutes). Another sample was included to assess the same temperature and time conditions as the previous MEA, but at a lower pressure (200°C, 7.72MPa, 10 minutes). The third MEA was assembled and pressed at what was anticipated to be the most benign conditions for acid dehydration (140°C, 7.72 MPa, 1 minute). After hot-pressing these three samples, the resistance of the assembled MEAs was measured and then transferred to the SEM to measure the ratio of oxygen to phosphorus (O/P) within the membrane layer.

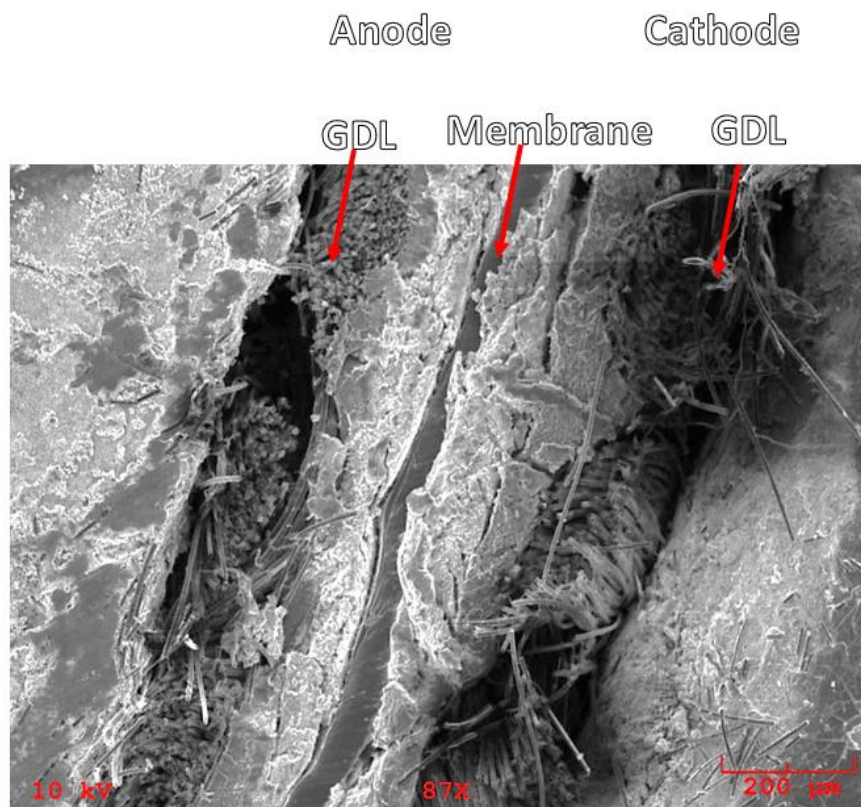


Figure 2.7. SEM cross-sectional image of MEA fabricated at hot-press conditions of 200°C and 92.68 MPa for 10 min

Measurement of the oxygen-to-phosphorus ratio was acquired through the percentage function on the SEM-EDX system, with the common form of orthophosphoric acid (H_3PO_4) having a molar O/P ratio of 4. It is known that loss of water can cause orthophosphoric molecules to combine via condensation, creating other forms of phosphoric acid with lower O/P ratios, for example

pyrophosphoric acid ($\text{H}_4\text{P}_2\text{O}_7$) and tripolyphosphoric acid ($\text{H}_3\text{P}_5\text{O}_{10}$); Higgins and Baldwin [10]. Figures 2.8 and 2.9 present the results of areal resistance and O/P ratio measurements for two MEA samples hot-pressed at 200°C for 10 minutes, but with different pressures of 92.68 and 7.72 MPa, respectively. In each figure, the left-handed vertical axis corresponds to the resistance, while the right-handed vertical axis corresponds to the molar ratio of oxygen to phosphorus. The horizontal axis indicates the stage in the testing process during which the measurements were taken. After the hot-press operation, it was observed that the O/P ratio for both MEAs had dropped well below the known orthophosphoric acid value of 4. For the sample pressed at 200°C and 7.72 MPa (Figure 2.9) the ratio dropped to 2.75, while for the sample pressed at 200°C and 92.67 MPa (Figure 2.8) the ratio was 1.25. For comparison, the equivalent sample pressed at 140°C yielded an O/P ratio of 3.98. These results suggest that at elevated pressing temperatures the acid was dehydrating. Comparing the resistance results against samples made previously at the same conditions showed they were reasonably consistent. These results for the ratio of oxygen to phosphorus cannot be used to determine the exact dehydrated form of phosphoric acid, however they provide a quantitative indication of conditions under which dehydration has taken place, thereby providing guidance for optimizing the MEA fabrication process.

After confirming that the acid was dehydrating under some hot-pressing conditions, another test was devised to determine if the dehydration of the phosphoric acid was reversible and if re-hydration would positively affect resistance. For this stage of the testing, only the two MEA samples pressed at 200°C were used as they had experienced the most significant level of dehydration. Both of the 25.4 mm square samples pressed at 200°C were sliced in half, creating two samples at both conditions for a total of 4 samples. For each material, one half was placed in ambient temperature and humidity conditions, the other half was placed in a humidified box at

30°C and 100% relative humidity. The samples were allowed to equilibrate for 3 hours in either environments and then transferred to a nitrogen atmosphere for 30 minutes to remove any surface moisture which may have accumulated.

The results for both materials are presented in Figures 2.8 and 2.9 moving along the horizontal axes, indicating that the oxygen-to-phosphorus ratio (O/P) increased upon moving the samples from the post hot-press conditions to the ambient environment or the humidified box. While these pressing conditions are the most aggressive studied in the present experimental campaign, the reduction in resistance with increasing hydration level indicates that phosphoric acid is dehydrating in the press, increasing the resistance of the MEA, but that this dehydration is reversible and adding water back to the material can result in a reduction of resistance.

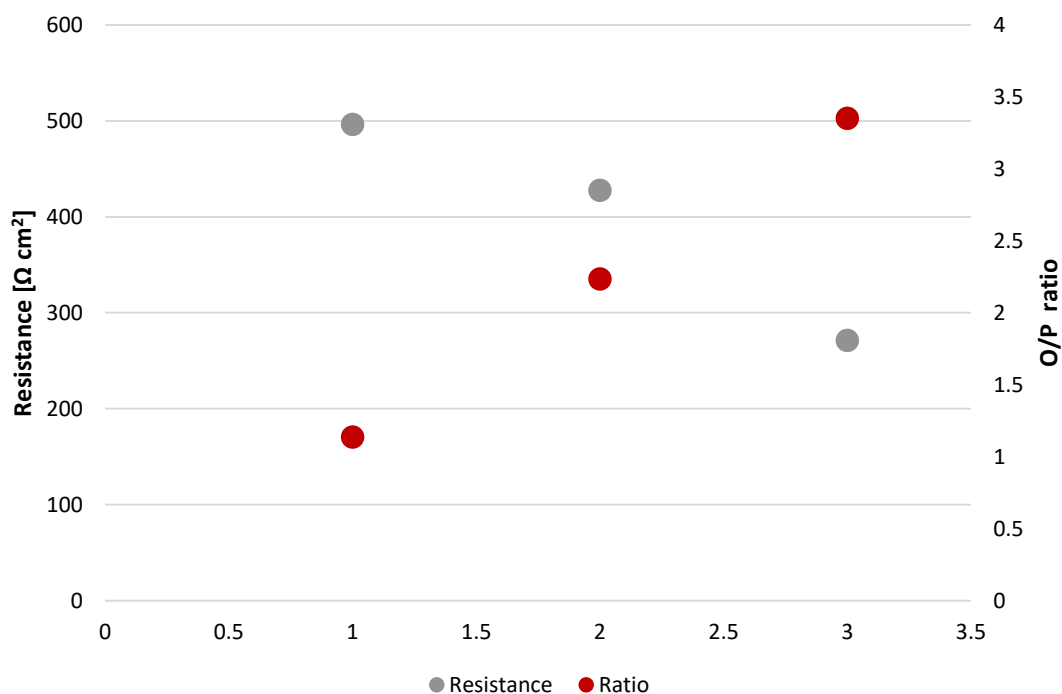


Figure 2.8. Resistance and oxygen-to-phosphorus ratio for MEA sample fabricated at 200°C and 92.68 MPa for 10 minutes. Resistance on the left-hand y-axis is area specific.

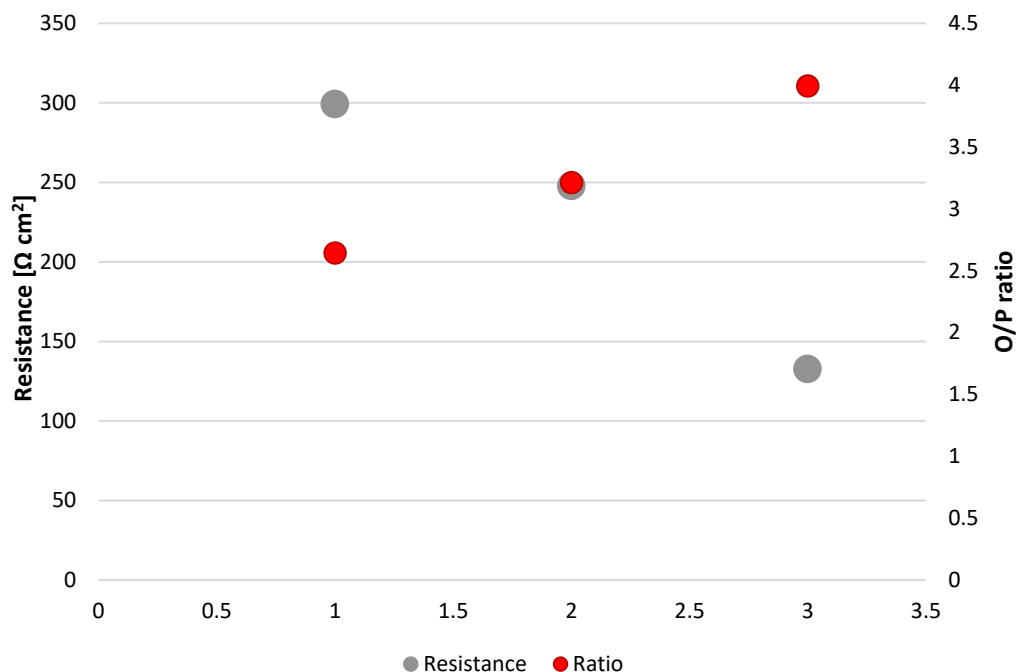


Figure 2.9. Resistance and oxygen-to-phosphorus ratio for MEA sample fabricated at 200°C and 7.72 MPa for 10 minutes. Resistance on the left-hand y-axis is area specific.

Impact of Catalyst Layer Thickness on Performance

Once the hot-pressing conditions had been optimized as described above, four functional 25.1 cm² MEA were prepared. Figure 2.10 shows the polarization curves of the MEAs prepared in-house compared against a commercially available HT-PEM MEA from Advent Technologies. The first in-house MEA was designed with a total loading of 1.8 mg/cm², utilizing a 20% platinum on carbon catalyst. The cell dropped to nearly 0 V around 0.5 A/cm², ending the test. The shape of the polarization curve indicates that the MEA was experiencing severe mass transport loss. In an attempt to minimize this loss, the electrode layer thickness was reduced by changing the percentage of platinum on carbon from 20% to 30%. By increasing the percentage of platinum on carbon, the electrode thickness was reduced, as a lower total volume of platinum on carbon catalyst was necessary to achieve the required loading of 1.8 mg/cm². Increasing the Pt percentage to 30%

resulted in a marked improvement in the MEA performance with maximum current density extending to about 0.85 A/cm^2 . With the improvements seen in increasing Pt/C from 20% to 30%, the electrode was made even thinner by increasing the percentage to 40% Pt/C. This resulted in a further increase in performance with the maximum achieved current density extending to at least 0.9 A/cm^2 . Increasing the percentage of platinum on carbon beyond 40% Pt/C would have become prohibitively expensive. However, to investigate the effect of further reduction in electrode thickness on MEA performance, the total platinum loading was reduced from 1.8 mg/cm^2 to 1 mg/cm^2 while maintaining the 40% Pt/C ratio from the previous run. Interestingly, this reduction in total platinum loading resulted in no significant change in the overall performance of the MEA fabricated with 40% Pt/C and total loading of 1.8 mg Pt/cm^2 .

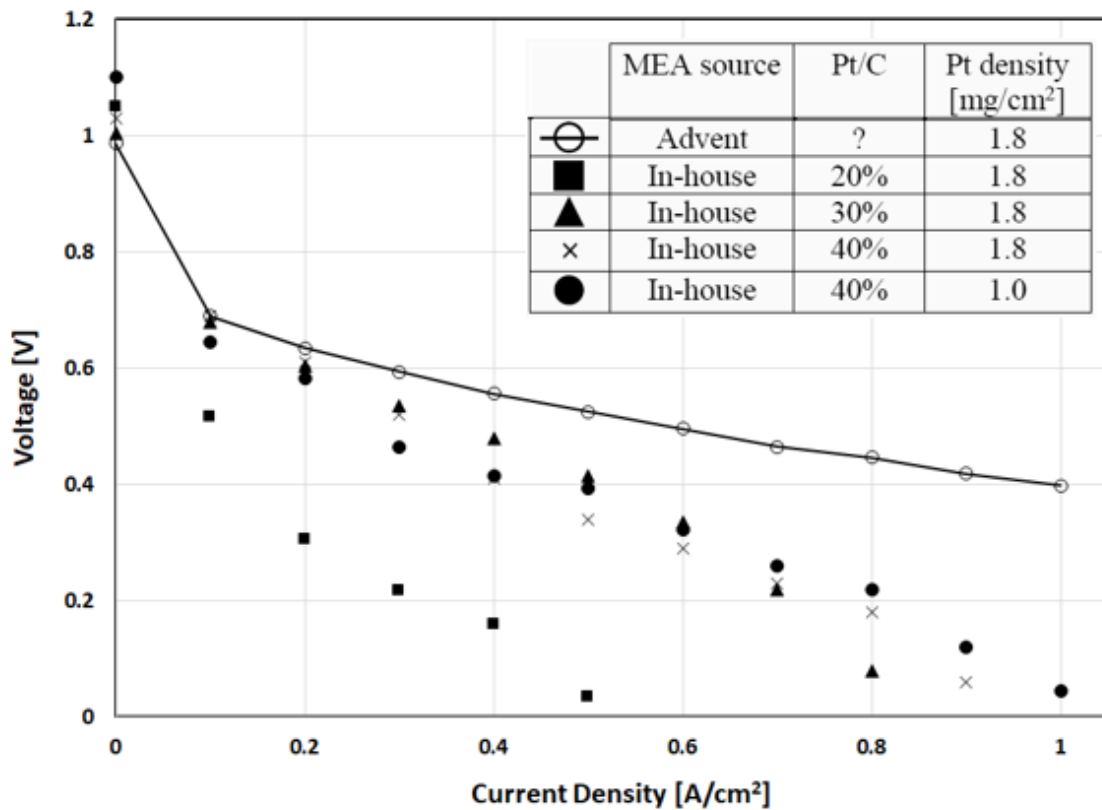


Figure 2.10. Polarization curves of in-house MEAs compared against commercial Advent PBI

Despite the adjustments made to electrode thickness, comparing the in-house MEAs with the commercially available Advent material indicates there is a persistent discrepancy between the performance of the two, particularly at higher current densities. It is possible that the micro-porous layer that came pre-coated on the GDL materials contributed to the performance loss of the in-house MEAs. Future research will involve material fabrication without micro-porous layers, because they are not critical to HT-PEM cell performance due to absence of water with higher operating temperature.

Conclusions and Implications

Through analysis of data for press failure rates, MEA resistance, and layer adhesion strength, we identified optimal HT-PEM MEA hot-pressing conditions of around 170°C and 23.1 MPa for 5 minutes. With these idealized fabrication conditions, four MEAs were prepared in-house to investigate the effect of electrode layer thickness on polarization curve performance, compared against a commercially available MEA. Through the use of SEM-EDX, a process was established to verify the dehydration of phosphoric acid within the membrane. It was shown that aggressive hot-pressing conditions can dehydrate the membrane within the MEA, increasing cell resistance. This dehydration was found to be reversible with post-process humidification recovering some of the lost conductivity. The presentation of this data can help to standardize and improve the future fabrication of HT-PEM MEAs.

Citations Chapter 2

1. P. Su, J. Cheng, J. Li, Y. Liao, T.L. Yu, *J. Power Sources*, **260**,131-139 (2014).
2. T. Søndergaard, L.N. Cleemann, H. Becker, D. Aili, T. Steenberg, H.A. Hjuler, L. Seerup, Q. Li and J.O. Jenson, *J. Power Sources*, **342**, 570-578 (2017).
3. C.I. Morfopoulou, A.K. Andreopolou, M.K. Daletou, S.G. Neophytides and J.K. Kallitsis, *J. Mater. Chem. A*, **1**, 1513-1622 (2013).
4. D. Share, L. Krishnan, D. Walczyk, D. Lesperence and R. Puffer, AMSE, *Eighth International Fuel Cell Science, Engineering and Technology Conference*, 44052 (2010).
5. K. Froelich, H. Rauner, F. Scheiba, C. Roth and H. Ehrenberg, *J. Power Sources*, **267**, 260-268 (2014).
6. A. Kannan, Q. Li, L.N. Cleemann and J.O. Jensen, *Fuel Cells*, **18**, 103-112 (2018).
7. D.F. Walczyk, Adaptive Process Controls and Ultrasonics for High Temperature PEM MEA Manufacture. United States: N. p., Web. doi:10.2172/1212771 (2015).
8. EN 12004-1:2017; Adhesives for Ceramic Tiles—Part 1: Requirements, Assessment, and Verification of Constancy of Performance. Classification, and Marking. European Committee for Standardization (CEN): Brussels, Belgium, 2017.
9. A. Schechter, R. Savinell, *Solid State Ionics*, **147**, 181-187 (2002).
10. C.E. Higgins and W.H. Baldwin, *Anal. Chem.*, **27**, 1780-1783 (1955).

Chapter 3 - Voltage Degradation of High-Temperature PEM Fuel Cells Operating at 200°C Under Constant Load

Materials and Methods

Commercially available P1100W MEAs from Advent Technologies were used for all the experiments. These 45.2 cm² active area MEAs were assembled within a fuel cell hardware kit procured from Fuel Cell Technologies, Inc. The PBI-based MEAs have a total catalyst loading of 1.75 mg/cm² using a phosphoric acid doped PBI membrane with woven gas diffusion layers. Data were not supplied by the manufacturer detailing the anode-cathode split of catalyst loading, nor for the specific composition of the catalyst. The fuel cell hardware was comprised of two aluminum endplates with ceramic heaters, two gold plated current collectors, and two pyro-sealed Poco graphite flow fields in a 4-channel quad serpentine pattern. The endplates compressed the entire assembly with 8 bolts torqued to 5.65 Nm (50 in-lbs). After each round of testing, the MEAs were stored in vacuum-sealed bags and the time between operations when exposed to ambient conditions was minimized.

Experimental Voltage Degradation Apparatus

All fixed-load degradation tests were performed on a modified Hydrogenics test stand under steady-state conditions of 200°C, 101.3 kPa and 0.4 A/cm², with anode and cathode stoichiometric ratios of 1.5 and 2, respectively. House compressed air was filtered and supplied to the cathode and pure hydrogen to the anode, neither with external humidification. All MEAs were subjected to a 24-hour break-in protocol at a temperature of 160°C and a current density of 0.2 A/cm², as per the manufacturer's recommendation. The test stand saturators were completely bypassed to ensure no added humidification of the inlet reactant streams. Heated inlet and insulated outlet hoses

prevented the formation of liquid water in the exhaust streams and minimized the formation of thermal gradients within the cell. The degradation test current density of 0.4 A/cm^2 is higher than many of the studies cited in Table 1.1 but is relevant to our intended mobile application as it should allow for a reduction in MEA active area and overall stack mass and volume.

A secondary testing setup was constructed to run extended durability tests. Using several mass flow controllers, a heating controller and a load bank, the cell temperature, gas flow rate and applied load could be managed in a way that minimized unexpected stand shutdown and failure. With this secondary test stand, an experiment was conducted at 160°C , 101.3 kPa and 0.2 A/cm^2 to use as a baseline to compare against values in literature. These conditions were selected as they are the most widely reported in the literature (Figure 1.1) and thus provided the best opportunity to verify our experimental setup and test procedure.

Figure 3.1 shows the voltage profile from this test (PBI 16), with an average degradation rate of $15.9 \mu\text{V/h}$ over the course of the 1588-hour run. This result is well within the range reported in literature and illustrated in Figure 1.2, and provided confidence that the experiments conducted at 200°C using the same test cell hardware and procedures would produce reliable data that will form the foundation of future research on HT-PEM operation under high temperature conditions that may be beneficial for reformat-based systems.

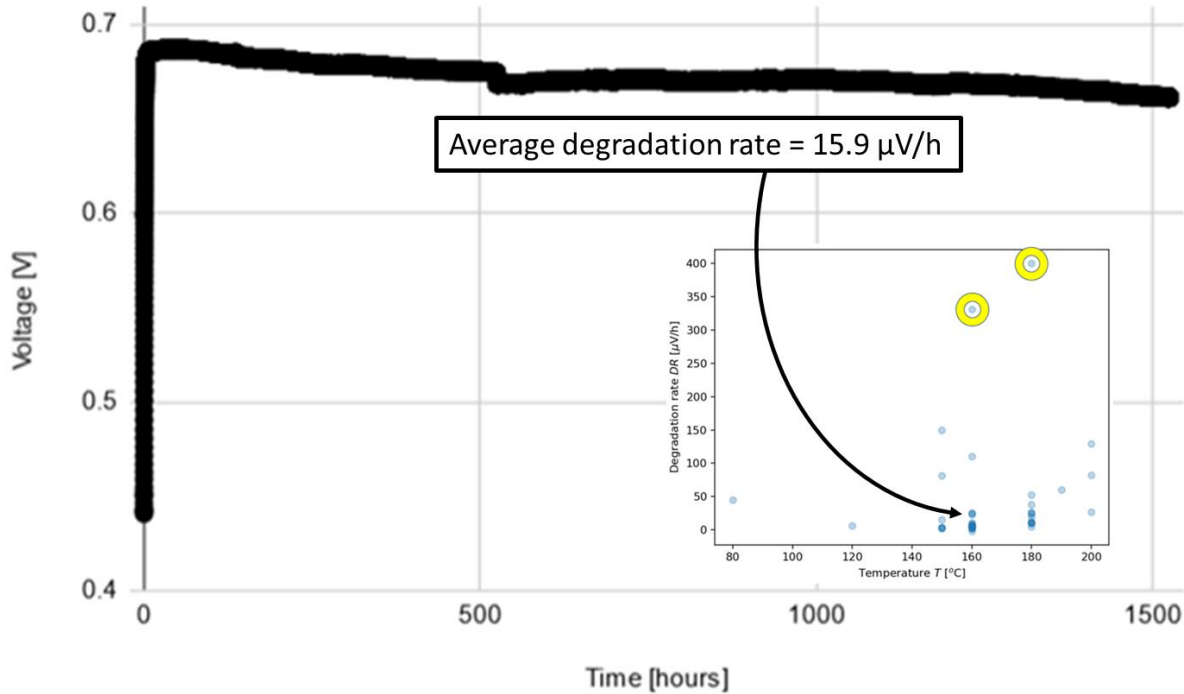


Figure 3.1 – In-house voltage degradation experiment with hydrogen/air at 0.2 A/cm^2 , 160°C and 101.3 kPa with H_2/air stoichiometric ratios = $1.5/2$. Inset plot from Chapter 1 indicates the measured voltage degradation rate is consistent with the majority of literature studies at the same nominal operating conditions.

From Figure 3.1, at roughly 500 hours into the test a slight step can be seen. With the goal of the 160°C , 0.2 A/cm^2 test in mind the step itself is not important. The trend shows a clear downward slope at a rate consistent with similar studies in literature, confirming the validity of our methods and setup. However, the reason behind the fluctuation in the trend is itself interesting. This issue occurred at the same time the nitrogen cylinder on the stand was changed. Nitrogen was not included in the reactants feeds but was kept on hand for safety and purging the cell. Due to a mechanical issue when the nitrogen tank was changed, nitrogen was introduced to the system for a short period of time. This caused a decrease in performance which was likely the result of temporary nitrogen dilution. It is interesting, however, to note that the voltage saw a slight

correction for a period of roughly 500 hours after the event, with the cell performance increasing then returning to a downward trend.

Results

Voltage Degradation Rate

Figure 3.2 presents the cell voltage results for the three MEAs run at 200°C and 0.4 A/cm² (PBI 1, PBI 2 and PBI 3), with numerical voltage degradation values also compared against the data acquired over approximately 1500 hours with a nominally equivalent cell run at 160°C and 0.2 A/cm² (PBI 16) in Table 3.1.

Table 3.1 – Constant load voltage degradation rates, run times, and times to peak voltage

MEA	Run Time [h]	Degradation Rate [μV/h]	Peak Voltage [V]	Time to Peak Voltage [h]
PBI 1 (200°C, 0.4 A/cm ²)	262	120.1	0.647	17.7
PBI 2 (200°C, 0.4 A/cm ²)	209	95.8	0.650	0.02
PBI 3 (200°C, 0.4 A/cm ²)	250	91.0	0.653	16.4
PBI 16 (160°C, 0.2 A/cm ²)	1588	15.9	0.687	50.2

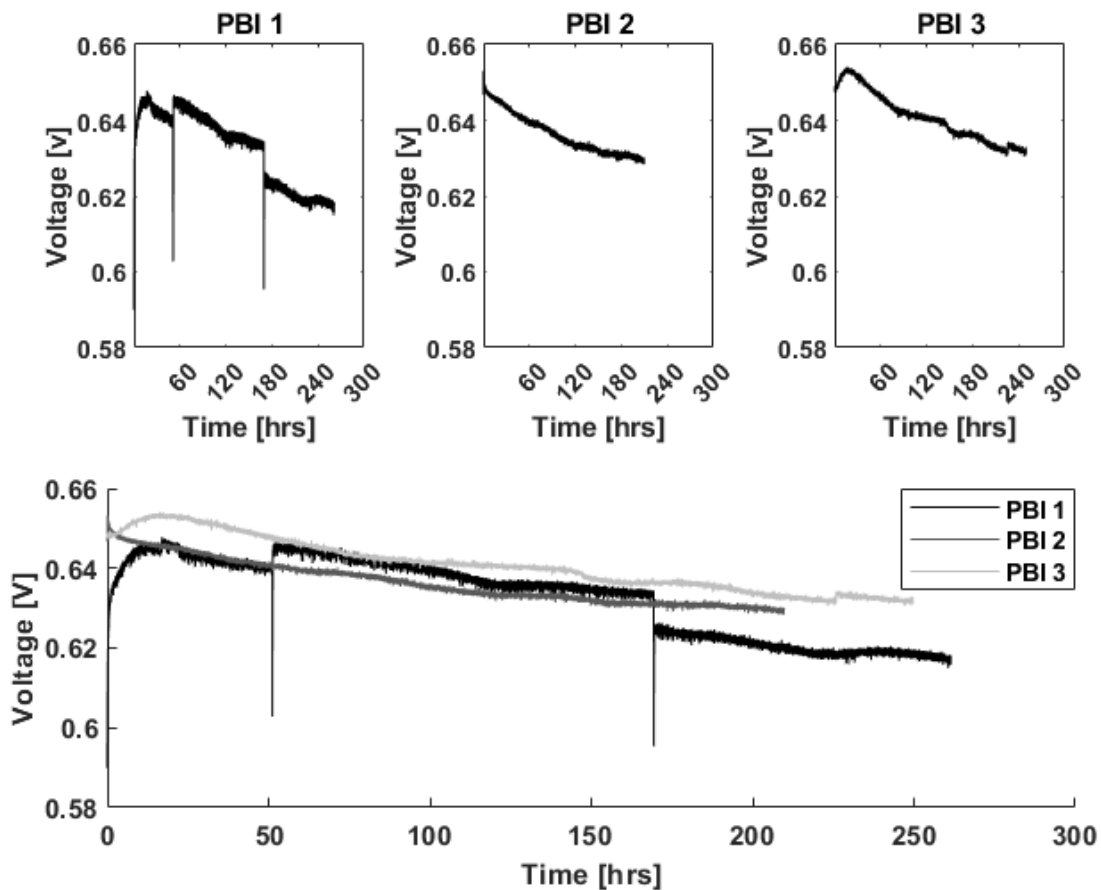


Figure 3.2 – Results of triplicate voltage degradation experiments run with Advent PBI materials at 0.4 A/cm^2 , 200°C and 101.3 kPa with H_2/air stoichiometric ratios = $1.5/2$

It can be seen that PBI 1 and 3 displayed similar trends, with a peak in voltage within the first 50 hours of operation. This trend has been reported in literature and is commonly observed for HT-PEM materials [1]. PBI 2 did not follow this same general trend, but further analysis of cell behavior during the break-in procedure showed that PBI 2 underwent a similar peak at around 5 hours into the break-in period. The reason for this profile is unknown, however, it is speculated that this result is due to a continued break-in of the MEA, potentially stemming from redistribution of phosphoric acid within the cell which is known to occur at higher rates during beginning-of-life operation [2][3].

Normalized Voltage

A normalized presentation of the voltage degradation behavior is provided in Figure 6. Here the data for each run were first truncated, with all discrete points occurring before peak voltage omitted. The data were then normalized by dividing each instantaneous voltage measurement by the peak voltage value.

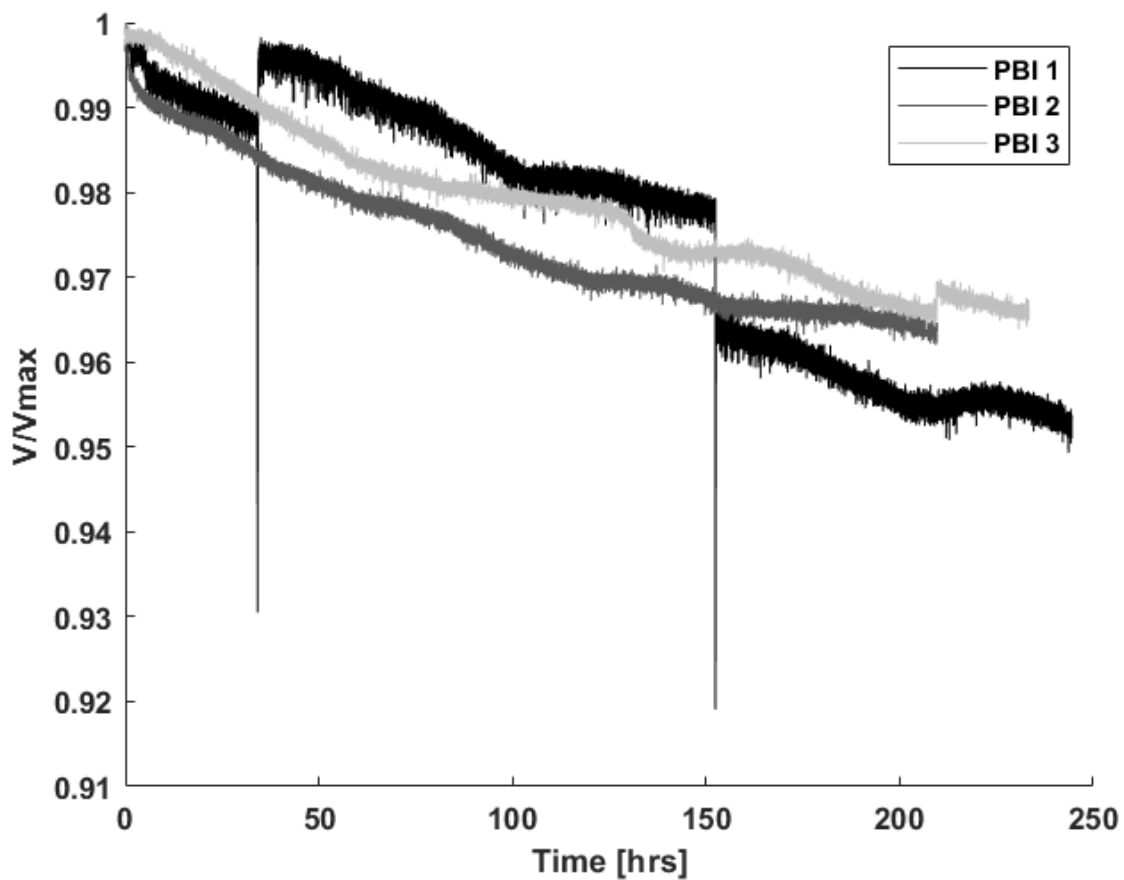


Figure 3.3 – Normalized voltage degradation profiles at 0.4 A/cm^2 , 200°C and 101.3 kPa with H_2/air stoichiometric ratios = $1.5/2$

These results show that the irregularities observed in the raw data presented in Figure 5 had little effect on overall MEA degradation rate. MEA performance relating to peak voltage and curve shape varied within each experimental run, but through analysis of normalized data the similarity in degradation performance between MEAs can be visualized. Because the cell assembly and test procedure were precisely replicated for each experiment, these performance variations are assumed to stem from material variations resulting from the membrane-electrode assembly manufacturing process. It is pertinent to reiterate that few of the prior studies summarized in Table 1.1 presented voltage degradation results based on duplicate or triplicate measurements, so the expected degree of performance variation for commercially procured HT-PEM MEAs is not well understood.

Voltage Degradation Rate Calculation

The voltage degradation rates were calculated using Equation 3.1, with 1-hour averages taken for 30 minutes on either side of the peak point near the beginning of the test and over the last hour at the end of the test. From these two values, the voltage decay (in volts) over the span of the test was calculated and this value was then divided by the difference in hours between time of peak voltage (t_{peak}) and end of test (t_{end}).

$$DR \left[\frac{\mu V}{hr} \right] = \frac{V_{peak} - V_{end}}{t_{end} - t_{peak}} \times 10^6 \quad (\text{Equation 3.1})$$

Discussion

The rate of degradation was relatively consistent, with minimum-to-maximum variation of 29.1 $\mu\text{V}/\text{h}$ among the three tests (Table 3.1). While variability in voltage exists and is clearly apparent in Figure 3.1, Figure 3.2 shows that the degradation behavior among the three MEAs was generally similar and each reasonably followed a linear profile.

The voltage profile of PBI 1 in Figure 3.1 shows two clear steps in the voltage occurring at roughly 50 and 125 hours. These anomalies correspond to two unplanned stand shutdowns. It is interesting to note that during the first shutdown a nitrogen purge was applied with the cell cooling to room temperature, resulting in a distinct increase in voltage. The second shutdown had no nitrogen purge and saw a step down in voltage while the cell cooled to around 100°C. While these shutdowns represent significant discontinuities in the test protocol, the voltage degradation rates across the three-time ranges remained fairly constant, and the effect on the overall test is considered insignificant. It is unknown what exactly the primary cause of the increase degradation rate seen here is when compared against other conditions reported in literature. There could be an agglomeration, diffusion and/or coarsening of the platinum catalyst particles during the testing, which may cause mass transport losses due to a reduction in active platinum surface area [4]. An increase in ohmic resistance or conversion of phosphoric acid into other forms of phosphorous acid that cause catalyst poisoning which can occur at high temperatures may also contribute to cell degradation [5]. Or it is possible that the materials utilized experience an increased mechanical degradation at increased temperature. Further work is required to identify the cause of and potential solutions to, the rate of performance loss identified in this study.

Conclusions

This study presents a review of HT-PEM voltage degradation studies, highlighting a gap in published data at relatively high current densities and temperatures, and the general lack of consistency among reported results. To address this research gap, degradation data for extended operation durability testing was acquired in triplicate with three MEAs operated under constant load conditions. The MEAs were subjected to over 200 hours of testing at constant operating conditions at 200°C and 0.4 A/cm². An average degradation rate of 102 μV/hr was recorded for these MEAs, which is significantly higher than rates reported in the literature for less aggressive conditions.

It is suspected that the high degradation rate is caused by an increase in phosphoric acid loss or catalyst deterioration resulting from the selected operating condition and parameters. While extended operation at 200°C, 0.4A/cm² does not encompass a full range of proposed high temperature PEM operating conditions, this study is useful in establishing a baseline for operation at previously understudied conditions and is a step in further developing high-temperature PEM fuel cells for novel applications. Further research is needed to improve understanding of the specific modes of degradation, and possible methods of mitigation through a combination of material design and operational control. Experimental work is underway to identify and quantify specific mechanisms responsible for HT-PEM fuel cell degradation at 200°C where relatively little research has previously been reported. This work will be continued in the next chapter.

Citations Chapter 3

- [1] Rastedt M, Büsselmann J, Klicpera T, Reinwald K, Pilinski N, Dyck A, and Wagner P. Determination of long-term stability and quality of HT-PEM MEAs. *ECS Trans* . 2018; 86.13:301–314 doi: 10.1149/08613.0301ecst.
- [2] Eberhardt SH, Toulec M, Marone F, Stampanoni M, Büchi FN, and Schmidt TJ, Dynamic operation of HT-PEFC: In-operando imaging of phosphoric acid profiles and (re)distribution, *J. Electrochem. Soc.* 2015;162.3:F310–F316. doi: 10.1149/2.0751503jes.
- [3] Hu J, Zhang H, Zhai Y, Liu G, and Yi B. 500 h Continuous aging life test on PBI/H 3 PO 4 high-temperature PEMFC. *Int. J. Hydrogen Energy.* 2006;31:1855–1862doi: 10.1016/j.ijhydene.2006.05.001.
- [4] Prokop M, Bystron T, Belsky P, Tucek O, Kodym R, Paider M, Bouzek K. Degradation kinetics of Pt during high-temperature PEM fuel cell operation Part III: Voltage-dependent Pt degradation rate in single-cell experiments. *Electrochim. Acta.* 2020;363: 137165. doi: 10.1016/j.electacta.2020.137165.
- [5] Orfanidi A, Daletou MK, Sygellou L, and Neophytides SG. The role of phosphoric acid in the anodic electrocatalytic layer in high temperature PEM fuel cells. *J. Appl. Electrochem.* 2013;43(11):1101-1116. <https://doi.org/10.1007/s10800-013-0626-2>

Chapter 4 - Assessment of Electrolyte Degradation of HT-PEM Fuel Cells at 200°C Under Constant Load.

HT-PEM fuel cells can experience performance loss over time stemming primarily from mechanical degradation, degradation of the electrolyte, or reduction of catalyst performance [3]. Mechanical degradation can take the form of degradation to the MEA, such as delamination of constituent MEA layers or the formation of pinholes within the assembly [4,5]. This mechanical degradation can also involve balance-of-plant components, a common issue being acid impregnation of graphite flow fields and acid buildup in gas channels. The most common electrolyte utilized in commercial HT-PEM systems is phosphoric acid, selected primarily for its high proton conductivity, but at temperatures above 160°C phosphoric acid can begin to “dehydrate”. This dehydration causes the formation of more concentrated forms of phosphoric acid within the orthophosphoric acid (H_3PO_4) transitioning to other forms such as pyrophosphoric acid ($\text{H}_4\text{P}_2\text{O}_7$) [6]. These more concentrated forms of phosphoric acid have lower conductivities which can lead to a reduction in performance of the cell. Additionally, phosphoric acid has been found to migrate out of the membrane into the gas diffusion layer over time [11] and even exiting the MEA materials entirely and moving to the flow fields, hardware connections, and ultimately residing in the water produced during operation [7]. Catalysts in HT-PEM may experience degradation due to particle agglomeration, electrochemical Oswald ripening, or occupation of active sites due to gas impurities such as carbon monoxide [8]. It is important to note that the presence of an aggressive acid such as a reduced form of ortho-phosphoric acid can have a negative impact on Pt based catalysts, further contributing to performance degradation [9]. From previous work it has been shown that the degradation rate of HT-PEM systems is strongly correlated to operating temperature. Higher temperatures lead to an increased rate of degradation, with

previously tested conditions of 200°C, 101kPa and 0.4 A/cm², resulting in an average degradation rate of 101.9 μV/hr over 200 hours [10].

Table 4.1 - Summary of prior studies of phosphoric acid loss in HT-PEM fuel cells

Year Reference	MEA	CD [A/cm ²]	Temp [°C]	Test duration [h]	PA measurement method	Sample prep	Measured PA range	Comments
2020 [Büselmann]	Fumapem® AM-40 Fumapem® AP-30	0.3	160	1000 - 9000	Titration	Punched sample soaked in 70% distilled water + 30% acetone, stirred for 30 min	~10 mg loss total or about 50%	
2018 [Halter]	Celtec MEA	0.2 - 0.8	160	1.2	X-ray tomographic imaging	In-operation	Reported in mm ³ /cm ² movement	Interesting work on the initial redistribution of PA
2018 [Kannan]	In-house	0.2	180	2000 - 5500	SEM-EDX and inductively coupled plasma optical emission spectroscopy	Water bath to separate out acid	0.22 - 150 ng cm ⁻² h ⁻¹ ; less than 6% collected in exhaust water	Tested different gas diffusion layers and PTFE content as a means of retaining acid within the membrane.
2018 [Søndergaard]	In-house	0.2 - 0.8	160 - 180	Up to 6000	Titration	Samples were die cut and leached in water	0-59 µg m ⁻² s ⁻¹	Embedded thermocouple used for internal temp measurements. Included 3D plots showing the effect of temperature, current density, and flow rate on acid loss. Increasing acid loss associated with larger values of all 3 parameters.
2018 [Søndergaard]	In-house	0.2 - 0.8	160-180	2,000 - 6000	Titration	150 mL ultrapure water, stirred overnight	0-59 µg m ⁻² s ⁻¹	Interesting insights into the effect of current density and temperature on acid loss.

2016 [Han]	20.25 cm ² active area Dongjin Semichem	1.1	150	84	Visual inspection and spectrometric measurement	Water samples collected from exhaust	0.35 - 0.45 μg h ⁻¹ cm ⁻²	Solutions made with exhaust water and different reagents used to change color depending on the quantity of acid present.
2015 [Eberhardt]	BASF Celtec	0.2 - 0.8	140- 160	0.5 – 4.3	In-operando synchrotron based X-ray tomographic microscopy	Redistribution of acid measured in real time		Virgin MEA used to calibrate greyscale image from the X-ray, from this image the volume of PA in the image was determined. Used to record migration of PA within the MEA in real time.
2015 [Pilinski]	Celtec® P1100W	0.3 - 1	160	500	Titration Ion chromatography	Leaching in water	449 – 457 mg total 200 - 6300 ng cm ⁻² h ⁻¹	Measured content of acid in MEA and flow fields; found ~1/3 of acid in cathode BP and the rest in MEA. Very little acid in the exhaust water during constant load test. However, increased at higher current densities and with load fluctuations.
2014 [Lang]	BASF P1000	0.2	120- 150	90 - 4600	Model	Created a model of acid loss	0.3 - 0.34 μg cm ⁻² h ⁻¹	Model used to simulate several runs at 120 and 150°C under humidified conditions.
2011 [Hartnig]	Celtec® P2100	0.35	180	1600	Titration	Samples boiled in water for 30 min with two repeats	Roughly 10% loss after 1600	Found that some flow field materials are better than others.

							hours for sealed graphite	
2009 [Li]	In-house	0.2	160	400	SEM, EDS	Exhaust water/ MEA sample	Found less phosphorus in sample after test	Initial pH of 4.3-6.0 in exhaust water, changed to 5.5-6.0 at around 150 hours. Used SEM to measure phosphorus movement within the MEA.
2009 [Oono]	In-house	0.2	150	450	Inductively coupled plasma mass spectroscopy and direct weight measurement	Exhaust water testing and membrane dimension measurement.	3E-0.6 to 5.8 E-0.6 mg	Found negligible amounts of acid in exhaust water. Reported acid loss in term of mass as the membrane measurement was based on the weight change. Looked into how doping level of membrane affected performance.
2009 [Wannek]	In-house	0.2	160	100	Optical emission spectroscopy with inductively coupled argon plasma	GDLs peeled off the membrane. Samples then leached 3 times in deionized water for one hour.	2-20 mg cm ⁻²	Measured quantity of acid within the membrane and both the anode and cathode GDLs separately. Performed experiments in adding PA to the GDL material.
2008 [Yu]	In-house	0.2	80-190	800 - 1000	Ion chromatography	Exhaust water collection bottles.	4.9 - 110 ng cm ⁻² h ⁻¹	Observed effects of both current density and temperature on PA content in exhaust water. PA loss at 190°C was an order of

								magnitude larger than at 160°C.
--	--	--	--	--	--	--	--	---------------------------------

Table 1 provides a summary of literature relevant to phosphoric acid degradation of HT-PEM. A variety of methods have been presented, ranging from in-situ imaging to post-mortem titration of MEA samples. The findings of Pilinski et al. (2015) had a significant impact on this research, particularly their findings on the use of exhaust water compared to direct MEA testing as a metric of acid loss [12]. Søndergaard et al. (2018) also influenced our understanding and assumptions on the mechanism of degradation for phosphoric acid within HT-PEM, as well as the effect of temperature and current density on acid loss [18]. In the present work, it was assumed that there are three factors at play driving acid loss the first being the dehydration of the acid. As the acid reduces from orthophosphoric to a more concentrated form such as pyrophosphoric acid the conductivity decreases, leading to a decline in fuel cell performance. The second mechanism, loss of acid due to the compression of the cell, is assumed to occur primarily at beginning of life and result from the compression of the MEA. The third mechanism is the loss of acid from the cell during operation as acid leaches out of the system. This is based on the general conceptual model of acid loss driving the HT-PEM fuel cell voltage reduction at high temperature, long term (> 200 hour) operation. Post-mortem material analysis were conducted in an attempt to quantify the relative contributions of the different mechanisms.

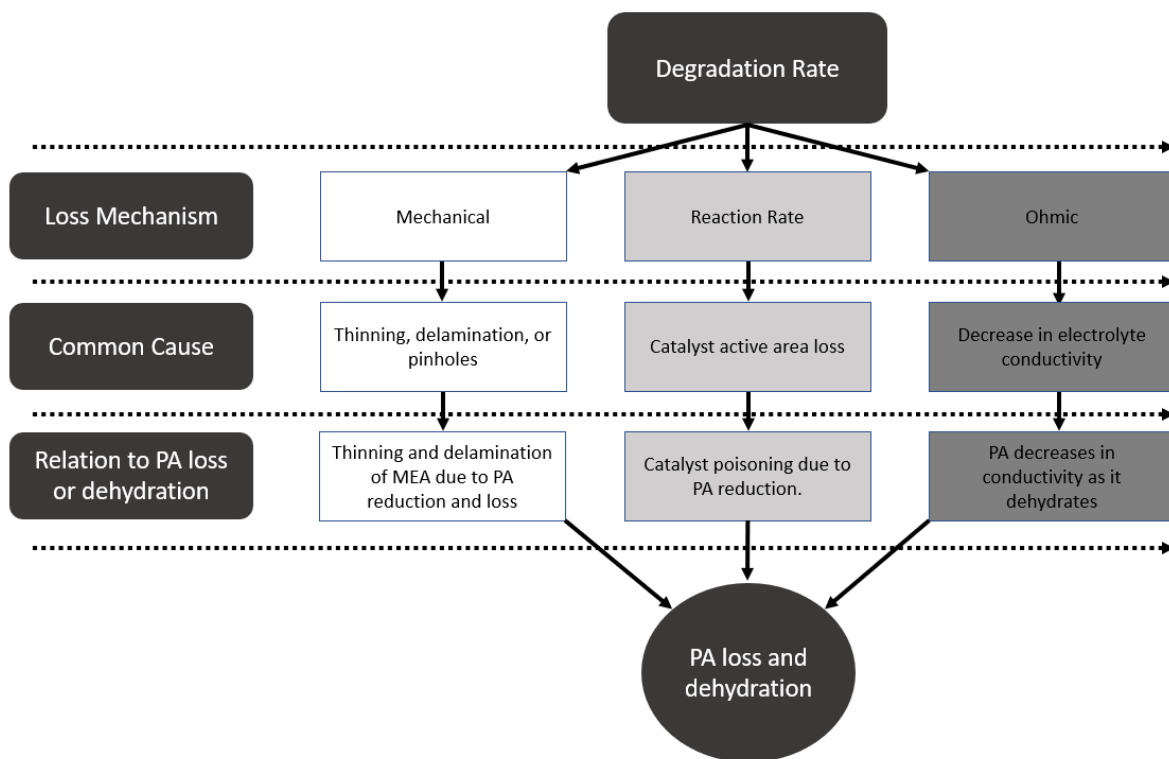


Figure 4.1- Conceptual map of HT-PEM degradation modes and their relation to phosphoric acid loss and dehydration

In the present work, we've attempted to delineate voltage loss associated with dehydration of phosphoric acid from loss of acid due to physical migration out of the MEA. Figure 4.1 provides a conceptual map of HT-PEM degradation modes and how the cause across several possible modes may stem from the common source of phosphoric acid dehydration and/or loss. Due to the results of our previous experiments conducted at 200°C (Leader et al., 2022), as well as the findings of our review and conceptual map, it was decided to focus our research on phosphoric acid loss as potentially the dominate degradation mode of HT-PEM under these operating conditions [10].

Experimental Materials and Methods

All experiments employed commercially available 45.2 cm² P11000W MEAs sourced from Advent Technologies (Boston, MA, USA). These MEAs utilize a phosphoric acid doped membrane and feature a total catalyst loading of 1.75 mg/cm² combined between the anode and cathode electrodes. The composition of the catalyst and the allocation of catalyst between anode and cathode was not provided by the supplier. The MEAs were assembled in commercially available testing hardware consisting of two Poco sealed graphite flow fields with serpentine channel structure oriented in counter-flow, two gold plated current collectors and compressed using two aluminum backing plates with 8 bolts torqued in pattern to 5.65 N-m (50 in-lbs.); Figure 4.2.

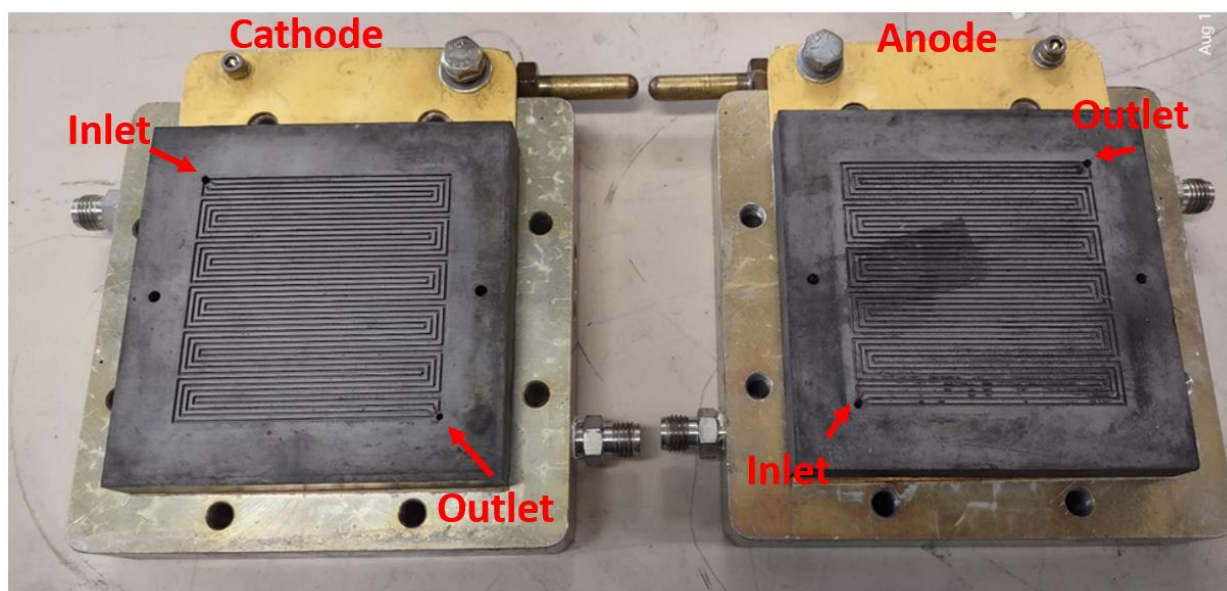


Figure 4.2: Flow fields used in fuel cell testing, operated in counter-flow orientation

Performance and Durability Testing Protocol

A custom fuel cell testing apparatus was configured for the extended durability tests, comprised of a temperature controller, load bank, N₂ purge setup, mass flow controllers and water collection system, all designed to minimize unintended shutdowns during the 200+ hour experiment durations. The MEAs underwent an initial break-in period of 24 hours at 160°C and 0.2 A/cm² as per the manufacture's specifications. After the break-in period, a series of polarization curves were acquired, this was then repeated after durability testing to establish beginning- and end-of-life performance. Durability tests were then run under constant conditions in galvanostatic mode at 0.4 A/cm², 200°C, atmospheric pressure, and with anode/cathode stoichiometric ratios of 1.2 and 2, respectively. The voltage was recorded every second with the average values calculated over one minute.

The degradation rate (*DR*) was calculated using Equation 4.1, based on the difference between peak and end voltage divided by the elapsed time. The value for peak voltage was calculated by identifying the maximum voltage out of the data set and averaging for 1 hour about that point. This process was repeated to calculate the end voltage by averaging the last hour of cell run time. Averaging the voltage values over one hour was done to reduce the impact of discrete outliers on the computed degradation rate. The resulting value was then scaled to report in units of microvolts per hour.

$$DR \left[\frac{\mu V}{hr} \right] = \frac{V_{peak} - V_{end}}{t_{end} - t_{peak}} \times 10^6 \quad (\text{Equation 4.1})$$

pH Measurement

A review of literature relevant to the measurement of phosphoric acid loss in HT-PEM fuel cells was introduced earlier in Table 4.1. A common method of phosphoric acid loss measurement has been to utilize the pH of the water produced by the electrochemical reaction to relate to acid concentration. From there, the quantity and effect of that migration of acid from the cell can be postulated. In the present study the pH of cell water was measured, but as reported by Pilinski et al. (2015) using pH is not a reliable method of quantifying the lost acid [12]. This is due to a significant portion of the migrated acid remaining in the flow fields and fittings of the testing hardware. The results of our research support this finding, with the cell hardware requiring cleaning after each use to remove phosphorus containing contamination accumulated in exhaust fittings and lines.

While there exist acknowledged limitations to the method of measuring acid content from the pH of the produced water, this measurement was still taken for two of the MEAs tested in the current campaign (PBI 5 and 6). In each case, the water was allowed to condense from the exhaust in a water trap and removed with the pH measured every 24 hours. For measurements of pH, a SevenCompact model S220 pH/Ion benchtop meter with pH electrode model LE348 from Mettler Toledo was used. Prior to each round of testing the device was calibrated and each pH measurement per sample was repeated in triplicate.

Phosphoric Acid Content Measurement

A Shimadzu EDX-8100 energy dispersive X-ray fluorescence spectrometer (EDX) was used to measure the content of phosphoric acid (PA) remaining within the MEAs after completion of durability testing. This method has been reported as a suitable method for phosphorus measurement in aqueous systems (Marvin and Ives, 1983; Yada and Ichimaru, 2018) [28,27]. A helium purge was used to increase the sensitivity of the device to lighter elements. Samples were prepared by placing two 6.4 mm (¼ inch) diameter punch cut samples and 7 ml of deionized water within a vial, then placed in an oven at 30°C for 48 hours. A total of six MEAs were tested, including three subjected to 200+ hour durability testing (PBI 4, 5, and 6) as well as three virgin MEAs (V1, V2 and V3) which had not undergone testing and were included as a baseline for beginning-of-life PA content.

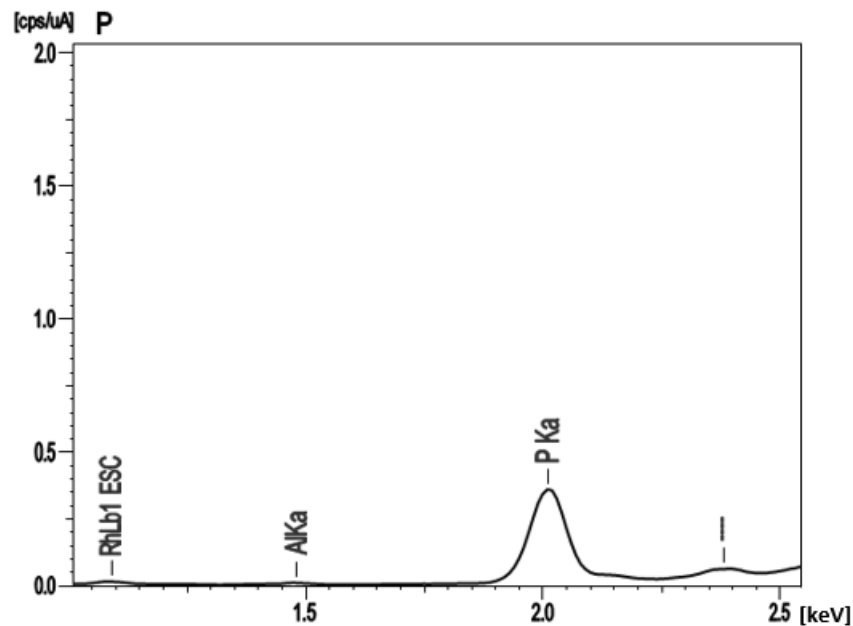


Figure 4.3- Example spectrum from phosphorus quantity measurement on Shimadzu EDX 8100

For each of these six MEAs, samples were taken from the anode inlet, center of MEA, and anode outlet. Each sample was then measured 3 times with the results averaged for presentation. Several calibration points were then prepared in vials by adding a known volume of orthophosphoric acid to 7 ml of deionized water. An example of the EDX spectrum is provided in Figure 4.3 which shows the profile for a prepared calibration sample with a known quantity of 0.05 ml of phosphoric acid in 7 ml of deionized water. This was then compared to a standard of pure deionized water and the sample holder to identify the source of the other peaks seen within the sample spectrum profile apart from the phosphorus.

As seen in Figure 4.3 the EDX operation returned results in units of CPS/ μ A. To relate this to quantity of phosphoric acid, a custom calibration curve was made by adding exact quantities of phosphoric acid (0.05 ml, 0.025 ml, 0.0125 ml, 0.00625 ml, and 0.003125 ml) to 7 ml of deionized water and recording the output of the EDX operation. From these data, a calibration curve was made and found to be linear. The equation produced from a best fit line was used to relate the sample measurements from the MEAs to a quantity of acid lost (Figure 4.4).

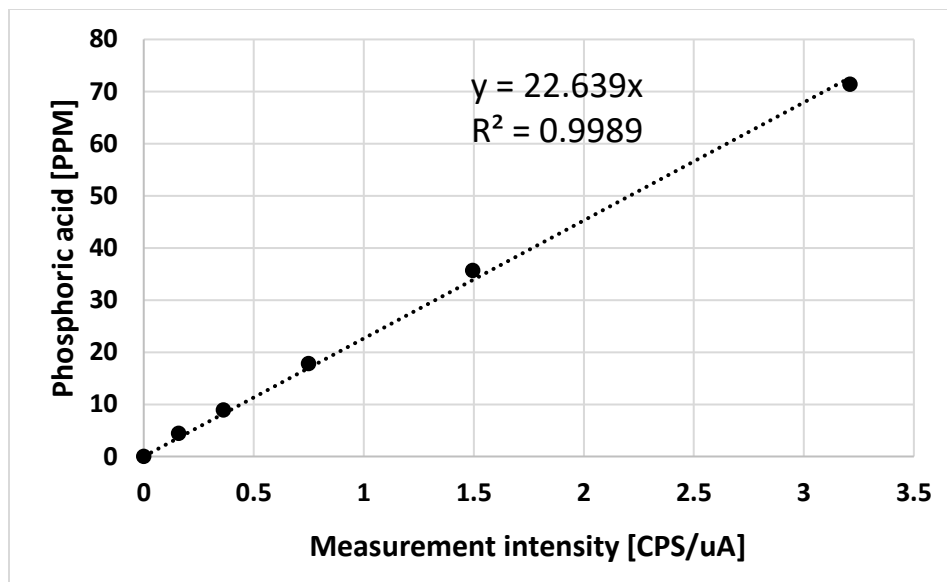


Figure 4.4 - Calibration curve relating phosphoric acid content to counts per second per micro-amp [CPS/μA]

Oxygen-to-Phosphorous Ratio Measurement

A scanning electron microscope (SEM) with EDX function was employed to measure the molar ratio of oxygen to phosphorus (O/P) immediately after the completion of durability testing. This ratio was used to determine the “hydration” level of the phosphoric acid remaining in the MEA at the end-of-life in comparison to three untested virgin MEAs from the same manufacturer and production lot as the tested MEAs. Samples were taken from the anode inlet, center, and anode outlet regions of the MEA. These samples were then fixed within a custom sample holder allowing the SEM to image the MEA in cross-section. Using a voltage of 10 keV, the MEA sample was scanned in the SEM EDX and the ratio of oxygen to phosphorus was recorded.

While the measured O/P value could not be used to determine the exact form of the phosphoric acid, it has been found to be directionally correct, with a lower value indicating some degree of

acid dehydration . Two or more orthophosphoric acid molecules (H_3PO_4) with O/P = 4.0 can be combined via condensation into larger molecules by the elimination of water. These larger molecules, for example pyrophosphoric acid ($\text{H}_4\text{P}_2\text{O}_7$) and triphosphoric acid ($\text{H}_5\text{P}_3\text{O}_{10}$), have lower O/P ratios of 3.5 and 3.3 respectively. However, it is unknown what percentage phosphoric acid was used in the doping of the commercial MEAs in this study. Typically, phosphoric acid is sold as an 85 wt% aqueous solution and there exists published studies on MEA fabrication using this concentration (Yang,2014) [29]. This extra oxygen bound in the water would show up in the EDX measurement, potentially skewing results toward a higher level of hydration. Accounting for the water content of the 85% solution, we should have an oxygen to phosphorus ratio of approximately 5.

To confirm the viability of this method, a series of tests was performed on samples of PBI membrane designed for fuel cell use procured from Celazole® PBI. Two samples of the membrane were cut from the larger roll. The first of these samples was immediately placed in the SEM for EDX analysis, looking for any pre-existing phosphorus or oxygen within the PBI material. No evidence of either element was found. The second sample was submerged in an 85% orthophosphoric aqueous solution for 6 hours. The doping timeframe of 6 hours was used as the material had shown peak acid uptake after 6 hours in previous work. (Leader,2022) [10].

After doping, the sample was removed from the acid, patted dry with a Kimtech wipe, and placed within the SEM for EDX measurement. The doped sample had an oxygen to phosphorus ratio of 5.1, close to the expected ratio of 5 for 85% ortho-phosphoric acid. This indicates that the 15% water content of the 85% acid solution had a significant impact on the measurement of O/P. The second half of the doped sample was placed in an oven at 200°C for 200 hours to simulate the conditions of the durability testing. After baking in the oven, the membrane yielded an oxygen-

to-phosphorus ratio of 1.8. To the naked eye, the sample had changed as well. Prior to entering the oven, the doped sample had been a light honey color and was highly flexible, while after the oven drying the sample had turned a dark brown color and became brittle and stiff. The results of this initial test showed a decrease in the oxygen-to-phosphorus ratio corresponding to dehydration of the acid. Therefore, measuring O/P in HT-PEM membranes provides information on the relative hydration state of the phosphoric acid, which in turn relates to the level of proton conductivity in the aged materials.

Results and Discussion

The voltage degradation profiles for PBI 4, 5 and 6, collected while running at constant conditions of 0.4 A/cm², 101 kPa and 200°C are presented in Figure 4.5. The timeline starts at zero hours indicating the beginning of the experiment, not including the 24-hour break-in period. PBI 6 in the top right of Figure 4.5 shows a small step in the voltage around 170 hours.

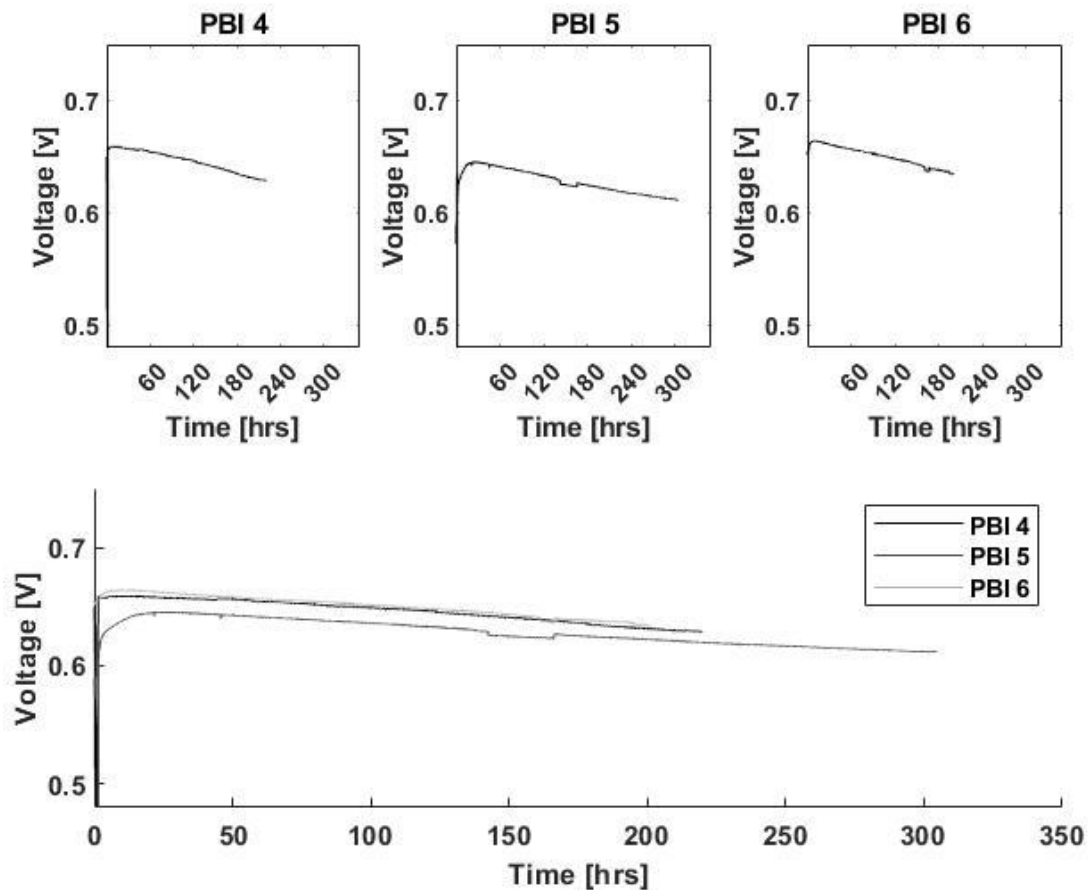


Figure 4.5– Results of triplicate voltage degradation experiments run with Advent PBI materials at 0.4 A/cm^2 , 200°C and 101.3 kPa with H_2/air stoichiometric ratios = $1.5/2$

It is not known what caused this, however, it is likely that it was a minor test stand issue and its effect on the degradation rate was assumed to be minimal as the voltage shortly returned to a level consistent with earlier measurements. It is also important to note that the y-axis range has been adjusted to $0.55 - 0.70 \text{ V}$ for better clarity which also has the effect of amplifying slight fluctuations in the data.

Table 4.2 - Comparison of voltage degradation rates for three tested MEAs

MEA	Time to peak V [h]	DR [$\mu\text{V/h}$]	Peak 1 hr avg [V]	End 1 hr avg [V]	Test duration [h]
PBI 4	12.9	133.4	0.659	0.629	235.2
PBI 5	24	119.3	0.645	0.612	304.8
PBI 6	13.1	156.4	0.664	0.634	200.5

Table 4.2 summarizes the results of the steady state degradation testing showing the degradation rate, time to peak voltage, and peak voltage value. The data demonstrate that variability exists in the performance of the nominally identical MEAs operated under identical conditions, assumed to stem from variations in the manufacturing of the MEAs.

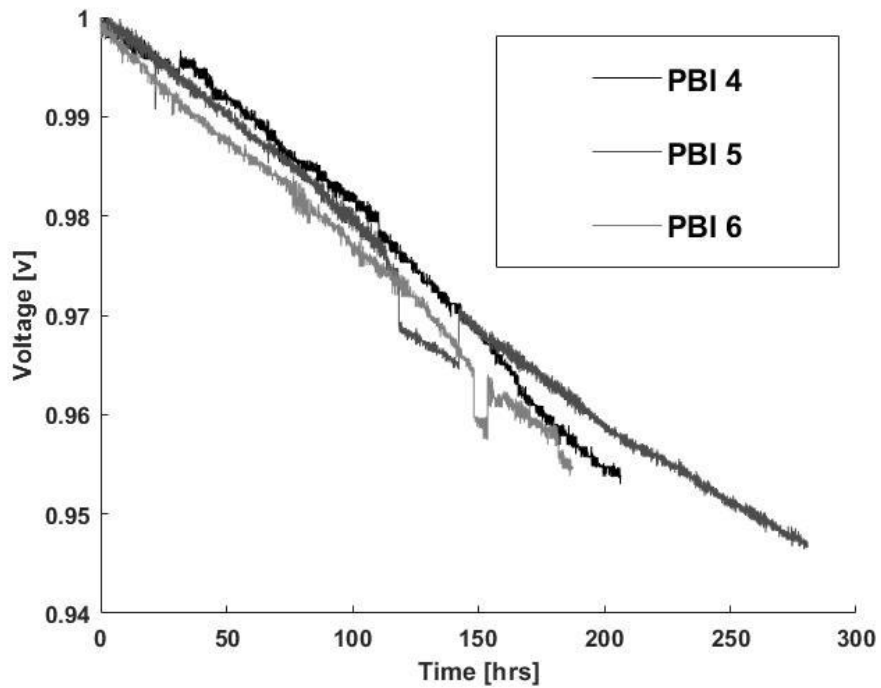


Figure 4.6 – Normalized voltage degradation profiles at 0.4 A/cm^2 , 200°C and 101.3 kPa with H_2/air stoichiometric ratios = $1.5/2$

Normalizing the data via Equation 4.2 and shown in Figure 4.6 visually reduces the effect of performance variability and enables the consistency of the degradation data to show.

$$\text{Normalized voltage} = \frac{V}{V_{Max}} \quad (\text{Equation 4.2})$$

For both PBI 5 and 6, beginning-of-life polarization curves running out to 1.6 A/cm² with a resolution of every 0.1 A/cm² were taken after break-in and end-of-life curves were recorded after the end of durability testing. From the curves in Figure 4.7, both PBI 5 and 6 a slight translation downwards can be seen with a more pronounced decrease at higher current densities, indicating an increased mass transport loss over the life of the test.

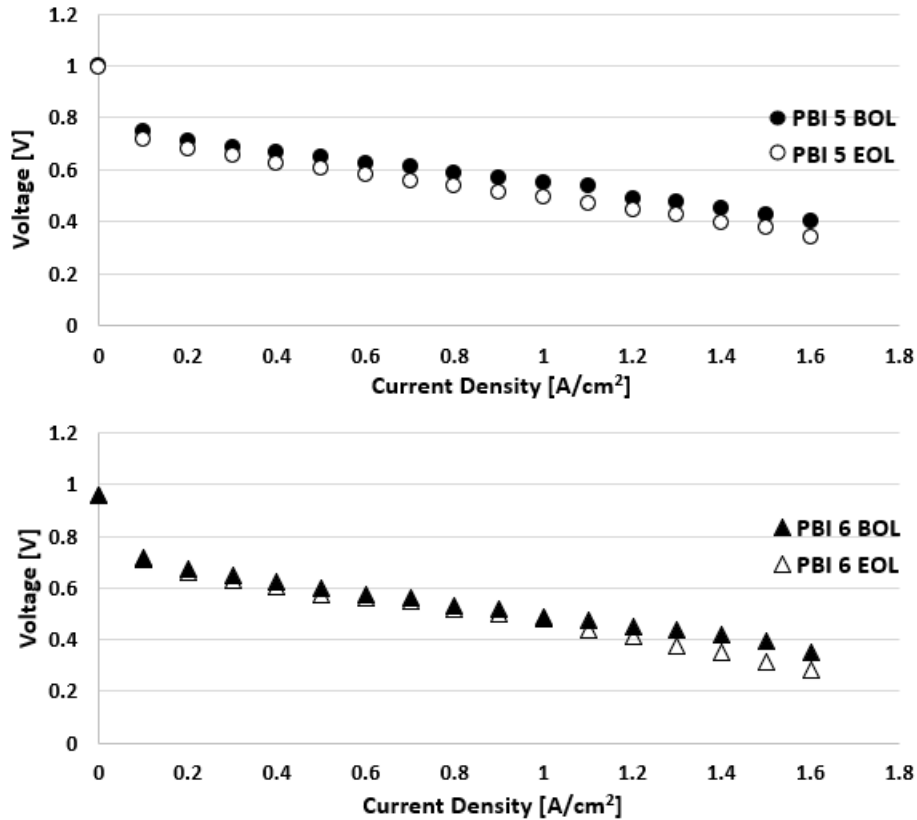


Figure 4.7 -Polarization curves for PBI 5 and 6 measured at beginning-of-life (after break-in) and end-of-life (at completion of durability testing)

Over the span of the test the pH of the product water was tested every 24 hours and recorded for both the anode and cathode. While the majority of the water was collected at the cathode water trap as expected, a relatively small quantity was collected from the anode exhaust. Both of these MEA water samples showed fairly consistent data over the span of the test, with a general trend of increasing pH and then leveling off to a generally constant level over time. This trend of increasing at beginning of life held true for all but the cathode of PBI 6 which has an outlier in the first measurement with the pH dropping from 4 to 3 (Figure 4.8).

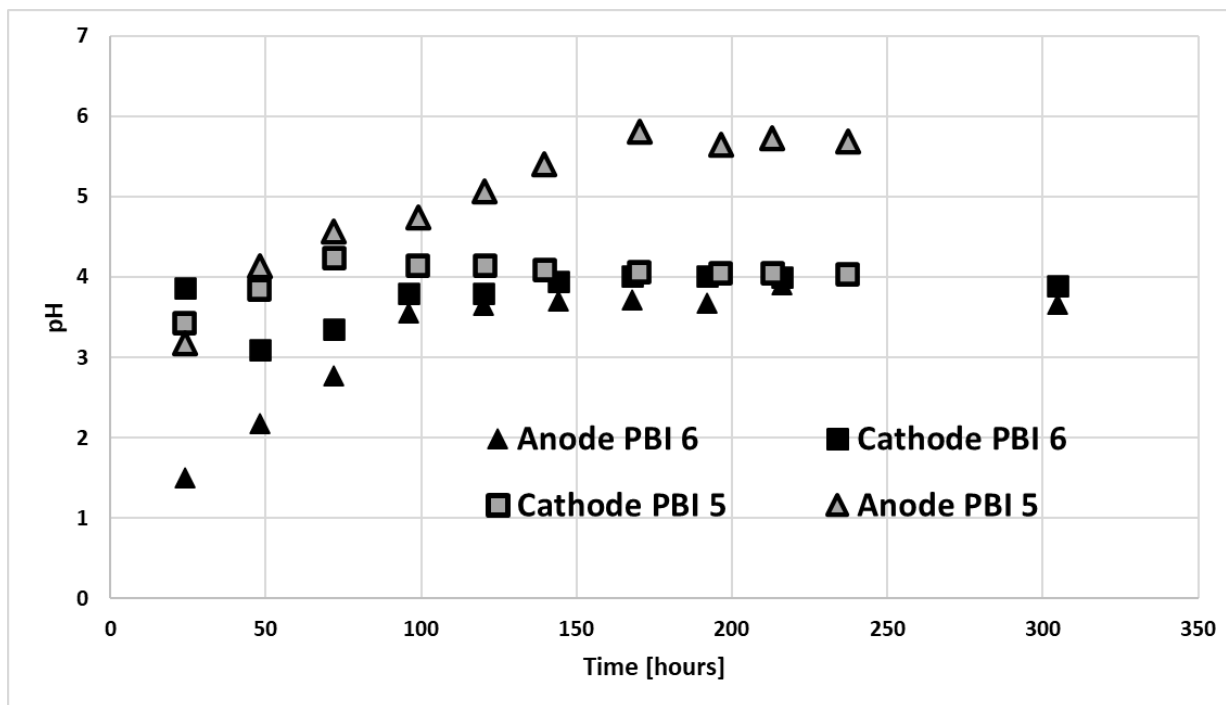


Figure 4.8 - pH of water collected at both cathode and anode exhaust for PBI 5 and 6

After this first measurement the cathode of PBI 6 conforms to the general trend with the pH rising from 3 to 4 over the next 3 measurements. While the anode of PBI 5 takes roughly 175 hours to reach a steady state pH of around 5.5, the other lines converge to a pH of around 4 after roughly 100 hours. It is not known exactly what caused these variations, however, it is suspected that beginning-of-life compression of the MEA within the hardware can cause an initial redistribution of phosphoric acid within the MEA, and potentially allow for more acid to be transferred into the product water stream. On the anode side, where the volume of water collected was in the range of a few millimeters, this may have impacted the measurement of the anode of PBI 5 resulting in the higher pH value.

As previously noted, pH measurement is not a complete or sufficient indication of the severity of acid loss. However, from these pH measurements it was determined that some amount of acid was

exiting the system, thus motivating further investigation. This was further substantiated by a visual observation made post testing while cleaning the hardware between runs. The outlet gas lines on both the anode and cathode had a buildup of some material in shades of blue to green, varying across tests and location in color. Upon scraping it out and collecting the resulting powder, further investigation in the EDX revealed it contained high concentrations of phosphorus. This confirms the assumption that pH results, while useful, do not tell the whole story on phosphoric acid loss due to accumulation of acid in fitting and lines which is then not represented in the pH measurement.

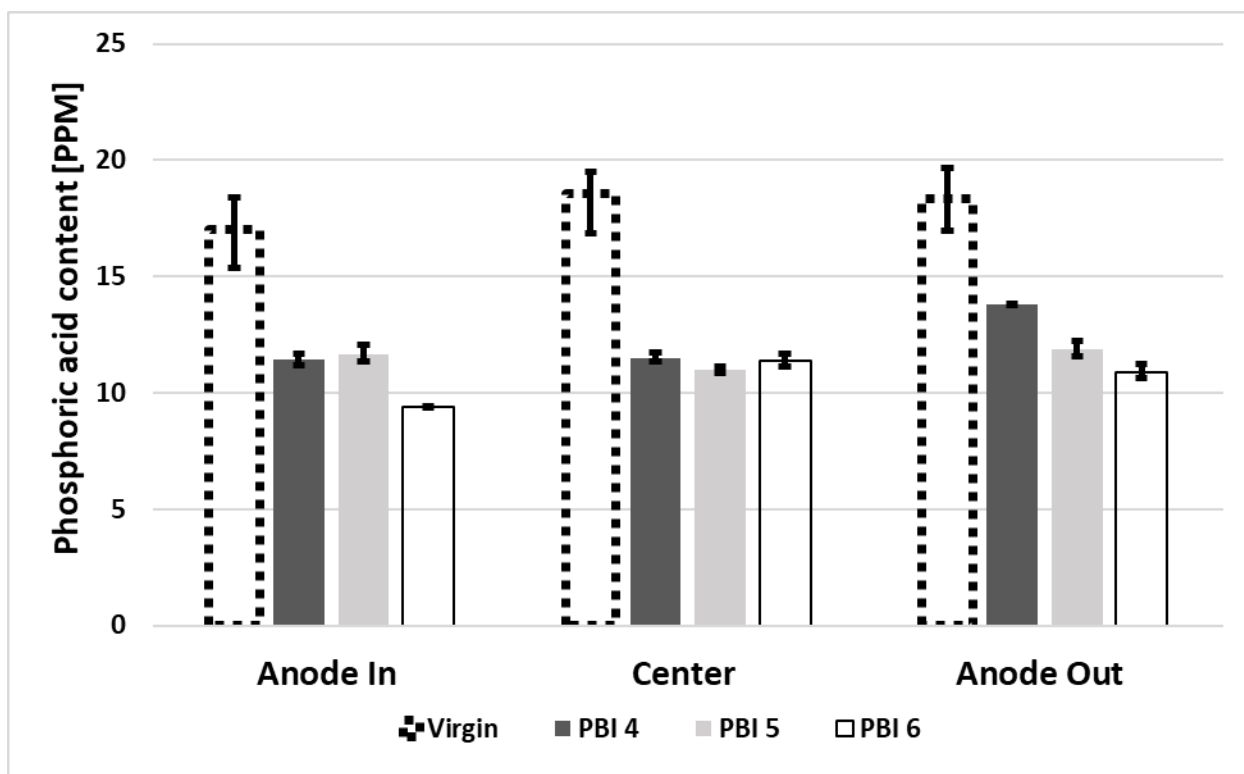


Figure 4.9 - Phosphoric acid content of degraded vs virgin MEAs

Figure 4.9 shows the results of the EDX measurements acquired to better understand the nature of the phosphoric acid loss. The sample locations reference the anode side of the MEA and with the

cell oriented in counter-flow mode, the anode in location corresponds to cathode out and vice versa. For each column in Figure 4.9, the bars indicate the minimum and maximum value among the 9 discrete measurements taken at that point. There is a marked decrease in the phosphoric acid content of the degraded samples vs the virgin samples. An ANOVA analysis was performed on this data set and there was found to be a statistically significant difference between the virgin and degraded MEAs as well as between each individual degraded MEA. From table 2 above, the run times of the 3 MEAs can be seen to vary from 200.5 to 304.8 hours. With this range of testing duration, it would be expected that the acid loss would vary between tests.

The mass change of the MEAs over the span of the durability tests is presented in Figure 4.10. Here the measured column represents the mass change of the MEA over the span of the test measured by using a scale prior to and after testing. This indicates an average mass reduction of about 0.4 g over the 200+ hour experiment duration.

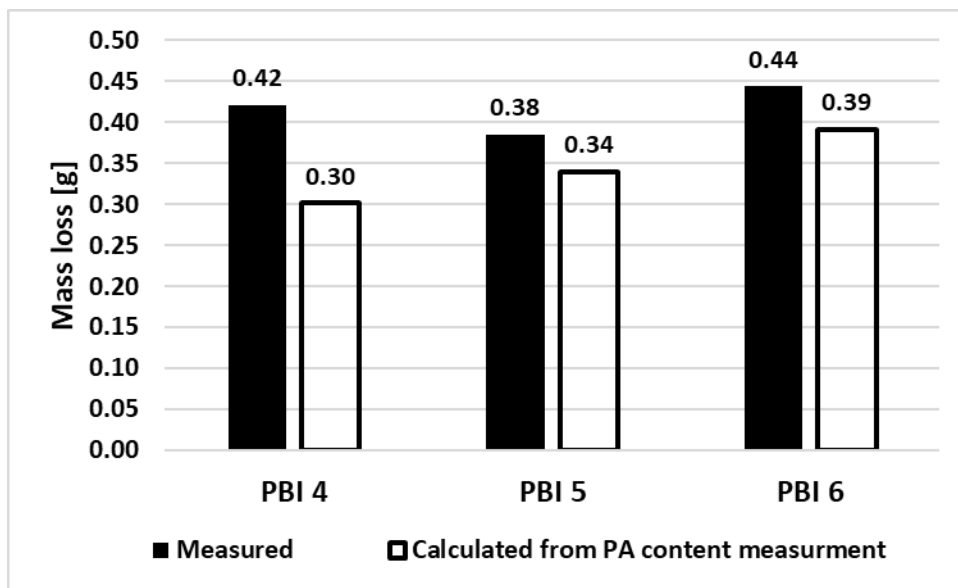


Figure 4.10 – MEA mass loss between beginning and end of testing for PBI 4, 5, and 6

The hydrophilic nature of the MEA is an important potential source of error in this measurement. When exposed to humid air in the ambient environment, droplets begin to form almost immediately on the surface of the MEA. It is assumed these are water droplets condensing on the surface. When placed on a scale in an attempt to measure the mass of the MEA the effect of this condensation can be seen. As the MEA sits on the scale the weight will slowly but consistently increase as more water condenses. To reduce this effect, during the end of testing while the system was being shut down the cell was purged with nitrogen and the connections capped before removal from the test stand. From there the MEA exposure to atmospheric conditions was limited and the MEA was stored in a vacuum-sealed bag. The initial measurement of the weight of the MEA was used and it was quickly removed from the scale to minimize water uptake.

In Figure 4.10, the hollow column titled “calculated from phosphoric acid content measurement”, uses the means of the data from the phosphoric acid measurement tests shown in Figure 4.9 to calculate the mass of acid lost over the course of testing. There is a slight discrepancy between the mass loss as measured by scale and through the acid loss calculation. Across the three tests the calculated loss was found to be lower than the measured loss. Several possible explanations for this exist. It may be that the water condensation discussed above impacted the measurement causing a larger loss to be recorded. Alternatively, it may result from a slight error in the phosphoric acid measurement process. This could potentially exist in the leeching phase of the sample preparation. If the virgin MEA material is less willing to release the imbibed phosphoric acid when compared against the degraded material, an under estimation of the acid loss and in turn mass loss could occur. Regardless, the greater mass loss seen on the scale versus the acid measurement results makes sense. In our acid leaching process, it was known going in that some amount of acid would remain within the MEA sample rather than leach into the water. This would

cause an underreporting of the amount of acid in the MEA and therefore an underestimation of mass loss.

Comparing the results for PBI 4-6 from the mass loss calculated from acid loss in Figure 4.10. It can be seen that the values range from 0.3 to 0.39 grams. A variation in mass loss is to be expected as the tests ranged in length from 200.5 to 304.8 hours as seen in table 2. However, what is interesting is that the greater mass loss does not coincide with the longer duration of tests.

In a similar fashion to the previous phosphoric acid content measurements, samples were taken from the anode inlet, center and outlet and measured in a SEM with EDX capabilities to determine the ratio of oxygen to phosphorus within the MEA sample.

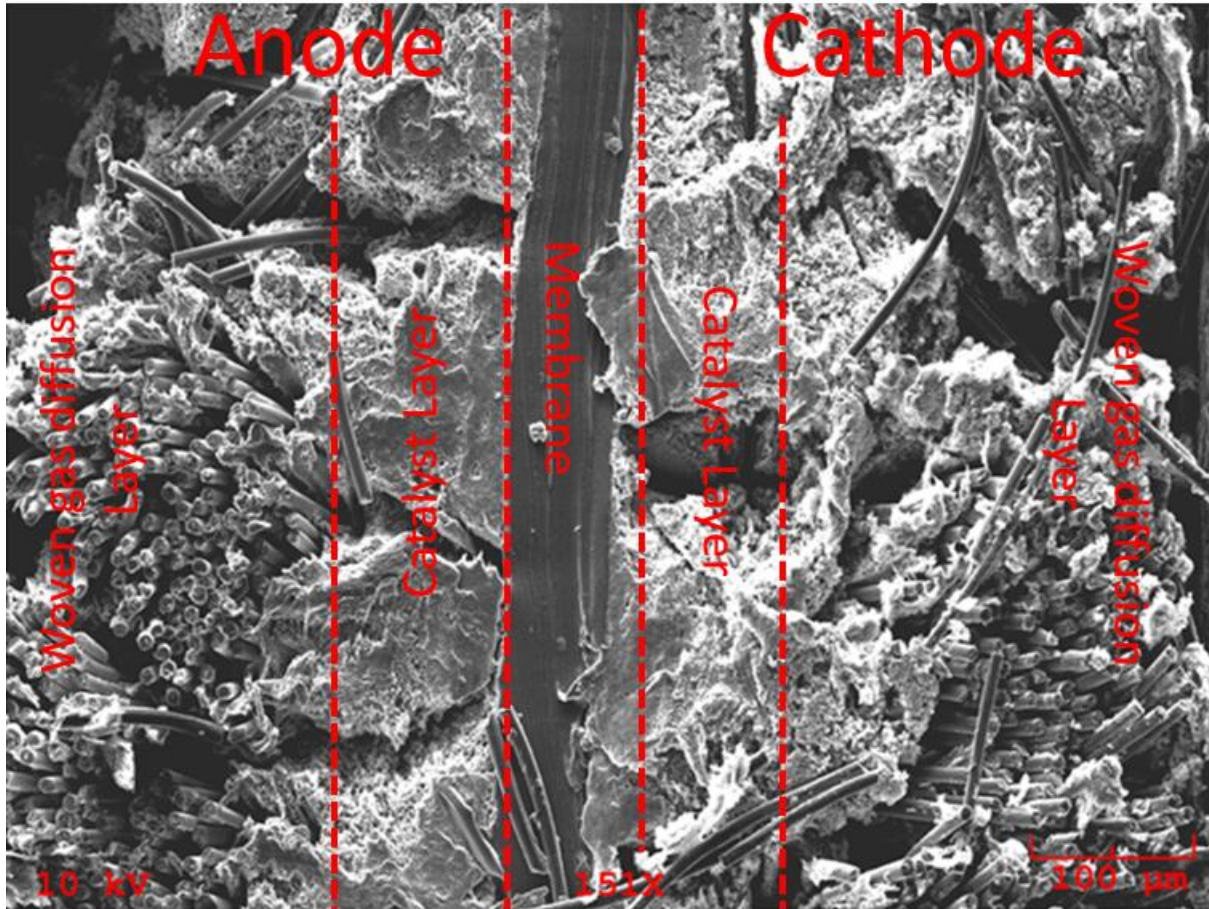


Figure 4.11 – Cross-sectional SEM image of PBI 4, highlighting different layers of the MEA

An example of the cross section of the MEA can be seen in Figure 4.11. In the outer most layers the individual fibers of the woven gas diffusion media can be seen. Within the gas diffusion media, the catalyst layer is recognizable as the brighter layer. Sandwiched within, at the center of the 4 layers is the membrane itself. In the figure the right side is the anode, and the left side is the cathode. For this analysis measurements, were made solely of the membrane itself not the other MEA components. This was done due to the nature of the woven fibers causing the SEM to experience issues returning inconsistent results with the variation in sample depth. The gaps

between cracks in the catalyst layer and the gas diffusion layer fibers presented an issue skewing the results. The location of the 3 samples is shown in Figure 4.12.

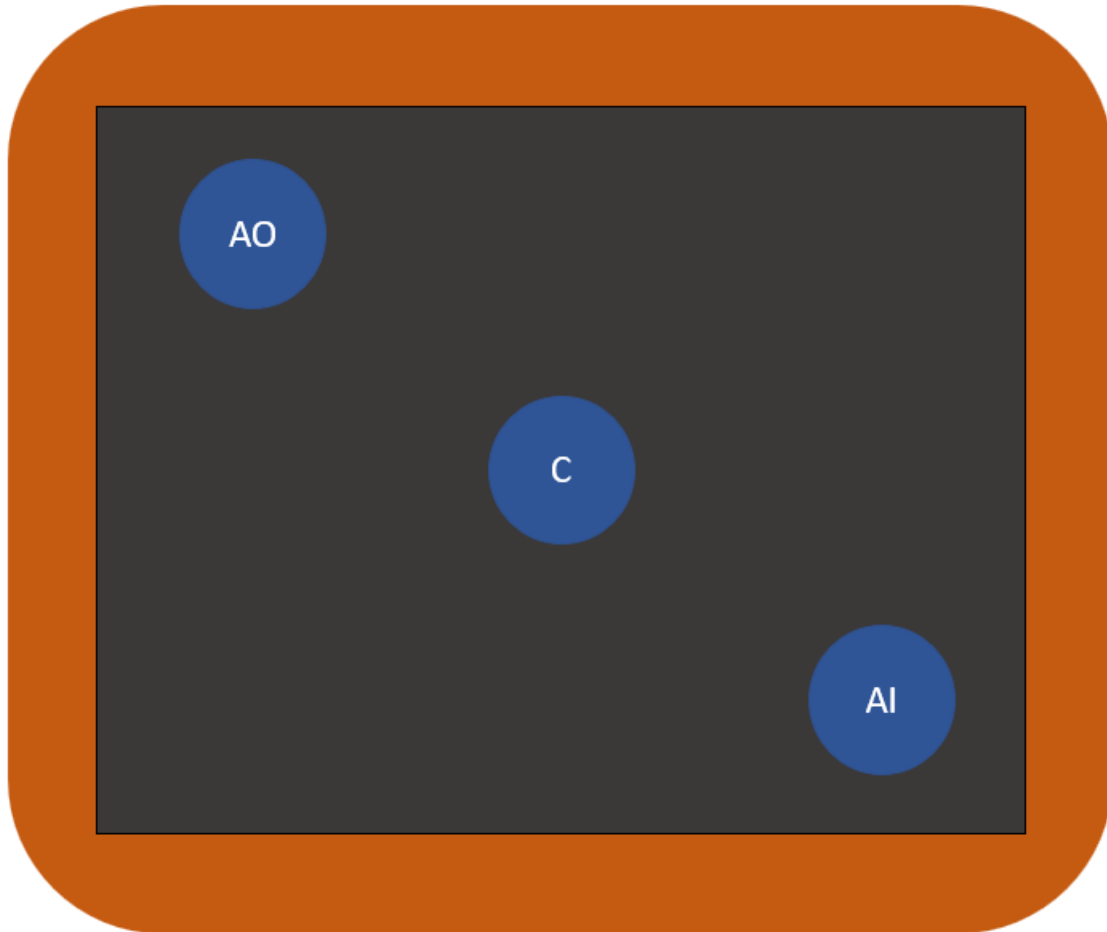


Figure 4.12 - MEA sample locations for the SEM EDX measurement of oxygen-to-phosphorus ratio. AO = anode outlet, AI = anode inlet, and C = center, figure not to scale

Table 4.3 - Comparison of oxygen to phosphorus ratios for the virgin MEA and PBI4, 5, and 6 post-durability testing

O/P Ratio	Anode Out	Center	Anode In
Virgin	4.1	4.7	3.9
PBI 4	2.5	3.2	2.8
PBI 5	2.9	3.6	3.1
PBI 6	3.0	3.6	3.8

The results of the oxygen to phosphorus ratio measurements can be seen in table 3 above. The virgin MEA shows the average of the 3 virgin MEAs measured. It was not anticipated that this measurement method would return results allowing for the identification of the exact phase of the phosphoric acid. For example, if the acid had reduced from the ortho to the pyro phosphoric acid phase, but rather that is would be directionally correct and indicate dehydration had taken place. For a fully humidified 85 wt% phosphoric acid one should expect the ratio of oxygen to phosphorus to be 4.97. The virgin material in this study reported values lower than the expected 4.97. This may be because of the hot pressing of the MEA in the fabrication process causing an initial dehydration of the acid before testing, or from the fabrication process using a different solution of phosphoric acid. From table 3 the ratio of oxygen to phosphorus shows a decrease from the degraded samples to the virgin ones. Across all the degraded samples (PBI 4, 5, and 6) the anode out location shows the lowest ratio of oxygen to phosphorus. This is interesting to note as the

anode out corresponds to the inlet of the cathode where the highest volume of dry gas is introduced to the MEA. It was expected that this location would yield the lowest oxygen to phosphorus ratio having the most dehydrated acid. While the anode out location shows the most reduced phosphoric acid, this trend is not seen in the measurements of the content of acid (Figure 4.9). This may indicate that the migration of the acid out of the MEA is not dependent on the reduction of acid to more concentrated forms.

From the findings in this study, it is now understood that phosphoric acid loss is occurring and is a likely culprit behind the increased degradation of the cell at 200°C. This phosphoric acid loss takes the form of both the physical migration of acid out of the active fuel cell system and the loss of electrolyte efficacy due to dehydration. It is understood from the pH results seen in Figure 4.8 that the acid migration out of the MEA is greatest at the beginning of life. This is most likely driven by the initial compression of the cell squeezing the acid out. Acid migration is assumed to continue at a reduced rate over the span of the tests which can be seen by the leveling out of the pH measurements over time. The acid migration over time is believed to stem from a steam distillation process as the cell produces water rather than the physical deformation of the MEA assembly. Over time the dehydration of the MEA membrane is understood to be the dominant mode of degradation as seen in the SEM EDX measurements in Table 3 and due in part to the known effect of temperature on phosphoric acid.

Conclusions

HT-PEM fuel cells are desirable and offer unique advantages in performance, simplified water management, and tolerance to fuel impurities. Unfortunately, many of these benefits are more pronounced at higher operating temperatures where increased degradation rates prevent long term operation. This work represents a step towards understanding the cause of the increased degradation observed at higher temperatures. Through the 200 hours testing a degradation rate was established, these 3 MEAs then underwent several post processing operations to determine the loss of performance, the state of phosphoric acid dehydration, and the loss of acid from the system. From this it can be seen that the MEA undergoes a significant loss of phosphoric acid as well as dehydration of the remaining acid which can explain the loss in performance. Of the two modes of phosphoric acid loss, migration, and dehydration, investigated here. The findings of this study indicate that the dehydration of the acid, not the migration of acid out of the system is the cause of the relatively large performance loss seen over time. Future work is needed to address the root cause of acid dehydration, possibly through rehydration via water addition or through the adjustment of operational parameters.

Citations Chapter 4

1. Rosli, R. E., et al. "A review of high-temperature proton exchange membrane fuel cell (HT-PEMFC) system." *International Journal of Hydrogen Energy* 42.14 (2017): 9293-9314.
2. Li, Qingfeng, et al. "The CO poisoning effect in PEMFCs operational at temperatures up to 200 C." *Journal of the Electrochemical Society* 150.12 (2003): A1599.
3. Prokop, Martin, et al. "Degradation kinetics of Pt during high-temperature PEM fuel cell operation Part III: voltage-dependent Pt degradation rate in single-cell experiments." *Electrochimica Acta* 363 (2020): 137165.
4. Zhang, Shengsheng, et al. "A review of accelerated stress tests of MEA durability in PEM fuel cells." *International journal of hydrogen energy* 34.1 (2009): 388-404.
5. Chandan, Amrit, et al. "High temperature (HT) polymer electrolyte membrane fuel cells (PEMFC)—A review." *Journal of Power Sources* 231 (2013): 264-278.
6. Higgins, Cecil E., and WILLIS H. Baldwin. "Dehydration of orthophosphoric acid." *Analytical Chemistry* 27.11 (1955): 1780-1783.
7. Aili, David, et al. "Exceptional durability enhancement of PA/PBI based polymer electrolyte membrane fuel cells for high temperature operation at 200 C." *Journal of Materials Chemistry A* 4.11 (2016): 4019-4024.
8. Araya, Samuel Simon, et al. "A comprehensive review of PBI-based high temperature PEM fuel cells." *International Journal of Hydrogen Energy* 41.46 (2016): 21310-21344.
9. Orfanidi, Alin, et al. "The role of phosphoric acid in the anodic electrocatalytic layer in high temperature PEM fuel cells." *Journal of applied electrochemistry* 43.11 (2013): 1101-1116.

10. Leader, J. O., et al. "Voltage degradation of high-temperature PEM fuel cells operating at 200° C under constant load and start-stop conditions." *International Journal of Hydrogen Energy* (2022).
11. Halter, J., et al. "Breaking through the cracks: on the mechanism of phosphoric acid migration in high temperature polymer electrolyte fuel cells." *Journal of The Electrochemical Society* 165.14 (2018): F1176.
12. Pilinski, Nadine, Maren Rastedt, and Peter Wagner. "Investigation of phosphoric acid distribution in PBI based HT-PEM fuel cells." *ECS Transactions* 69.17 (2015): 323.
13. Kannan, Arvind, et al. "Acid Distribution and Durability of HT-PEM Fuel Cells with Different Electrode Supports." *Fuel Cells* 18.2 (2018): 103-112.
14. Halter, J., et al. "Breaking through the cracks: on the mechanism of phosphoric acid migration in high temperature polymer electrolyte fuel cells." *Journal of The Electrochemical Society* 165.14 (2018): F1176.
15. Becker, Hans, et al. "Probing phosphoric acid redistribution and anion migration in polybenzimidazole membranes." *Electrochemistry Communications* 82 (2017): 21-24.
16. Lin, H. L., et al. "Durability and stability test of proton exchange membrane fuel cells prepared from polybenzimidazole/poly (tetrafluoro ethylene) composite membrane." *Journal of Power Sources* 193.1 (2009): 170-174.
17. Yu, S., L. Xiao, and B. C. Benicewicz. "Durability studies of PBI-based high temperature PEMFCs." *Fuel Cells* 8.3-4 (2008): 165-174.
18. Søndergaard, Tonny, et al. "Long-term durability of PBI-based HT-PEM fuel cells: effect of operating parameters." *Journal of the Electrochemical Society* 165.6 (2018): F3053.

19. Oono, Yuka, Atsuo Sounai, and Michio Hori. "Influence of the phosphoric acid-doping level in a polybenzimidazole membrane on the cell performance of high-temperature proton exchange membrane fuel cells." *Journal of Power Sources* 189.2 (2009): 943-949.
20. Hartnig, Christoph, and Thomas J. Schmidt. "On a new degradation mode for high-temperature polymer electrolyte fuel cells: How bipolar plate degradation affects cell performance." *Electrochimica acta* 56.11 (2011): 4237-4242.
21. Wannek, Christoph, et al. "Redistribution of phosphoric acid in membrane electrode assemblies for high-temperature polymer electrolyte fuel cells." *International journal of hydrogen energy* 34.23 (2009): 9479-9485.
22. Han, Seungyoon, et al. "Spectrophotometric analysis of phosphoric acid leakage in high-temperature phosphoric acid-doped polybenzimidazole membrane fuel cell application." *Journal of Sensors* 2016 (2016).
23. Lang, Sebastian, et al. "Experimental investigation and numerical simulation of the electrolyte loss in a HT-PEM fuel cell." *International Journal of Hydrogen Energy* 40.2 (2015): 1163-1172.
24. Eberhardt, Sebastian H., et al. "Dynamic operation of HT-PEFC: in-operando imaging of phosphoric acid profiles and (re) distribution." *Journal of the Electrochemical Society* 162.3 (2015): F310.
25. Søndergaard, Tonny, et al. "Long-term durability of PBI-based HT-PEM fuel cells: effect of operating parameters." *Journal of the Electrochemical Society* 165.6 (2018): F3053.
26. Büsselmann, Julian, et al. "Analysis of HT-PEM MEAs' Long-Term Stabilities." *Energies* 13.3 (2020): 567.

27. Yada, S. and Ichimaru, N., "X-ray fluorescence analysis of light elements in liquid samples – EDX-8100 and helium purge unit," Shimadzu Corporation, Application News No. X267, June 2018.
28. Marvin, D. C., & Ives, N. A. (1983). "Real time chemical analysis of phosphoric acid using energy dispersive x-ray fluorescence. *X-Ray Spectrometry*", 12(3), 106-110.
29. Yang, J. S., et al. "High molecular weight polybenzimidazole membranes for high temperature PEMFC." *Fuel Cells* 14.1 (2014): 7-15.

Chapter 5 - Mitigating Degradation of HT-PEM Systems Operated at 200°C

Introduction

The experiments in this section focus on the mitigation of cell degradation, through either periodic recovery of loss performance or through the elimination of degradation modes. The two primary methods employed here were the humidification of the cell with the injection of liquid water or the humidification of reactant flows. The second method applied pressurization of the cell in an attempt to suppress dehydration of the ortho-phosphoric acid electrolyte.

Experimental Materials and Methods

High-frequency resistance (HFR) measurement

A Solartron 1260A impedance gain phase analyzer was used in conjunction with the load bank connected to Stand 2 (described in Chapter 1) for the measurement of the cell resistance. HFR uses a high frequency sinusoidal wave superposed on the DC fuel cell components to measure the impedance of the system. This allows for the measurement of the resistance of the system in-situ without impacting the experiment.

pH measurement

The pH measurements in this section were performed in a similar way as in Chapter 4. An adjustment was made to the water collection apparatus part of the way through the work in this study. The change allowed the collection of a full 200 hours test worth of water in the stand water

reservoir, to reduce the impact of water collection that had previously been done at regular intervals throughout the test. The impact this had on testing and what prompted this decision will be covered the results and discussion section below.

Results and Discussion

Raw data

The voltage data plotted over time for the six PBI MEAs included in this study is shown in Figure 5.1 where each subplot shows the individual performance of each PBI-based fuel cell run. The composite figure at the bottom includes all six MEAs in the subplots for comparison against each other. Unlike in Chapters 3 and 4, here the measurements were not repeated in triplicate. These curves represent the outcome of several distinct operating parameters changes that can in part explain the greater spread in the data when compared against previous voltage plots. The only experiments performed under duplicate operating parameters were PBI 9 and 10. However, there are some slight differences between these two studies as discussed further below.

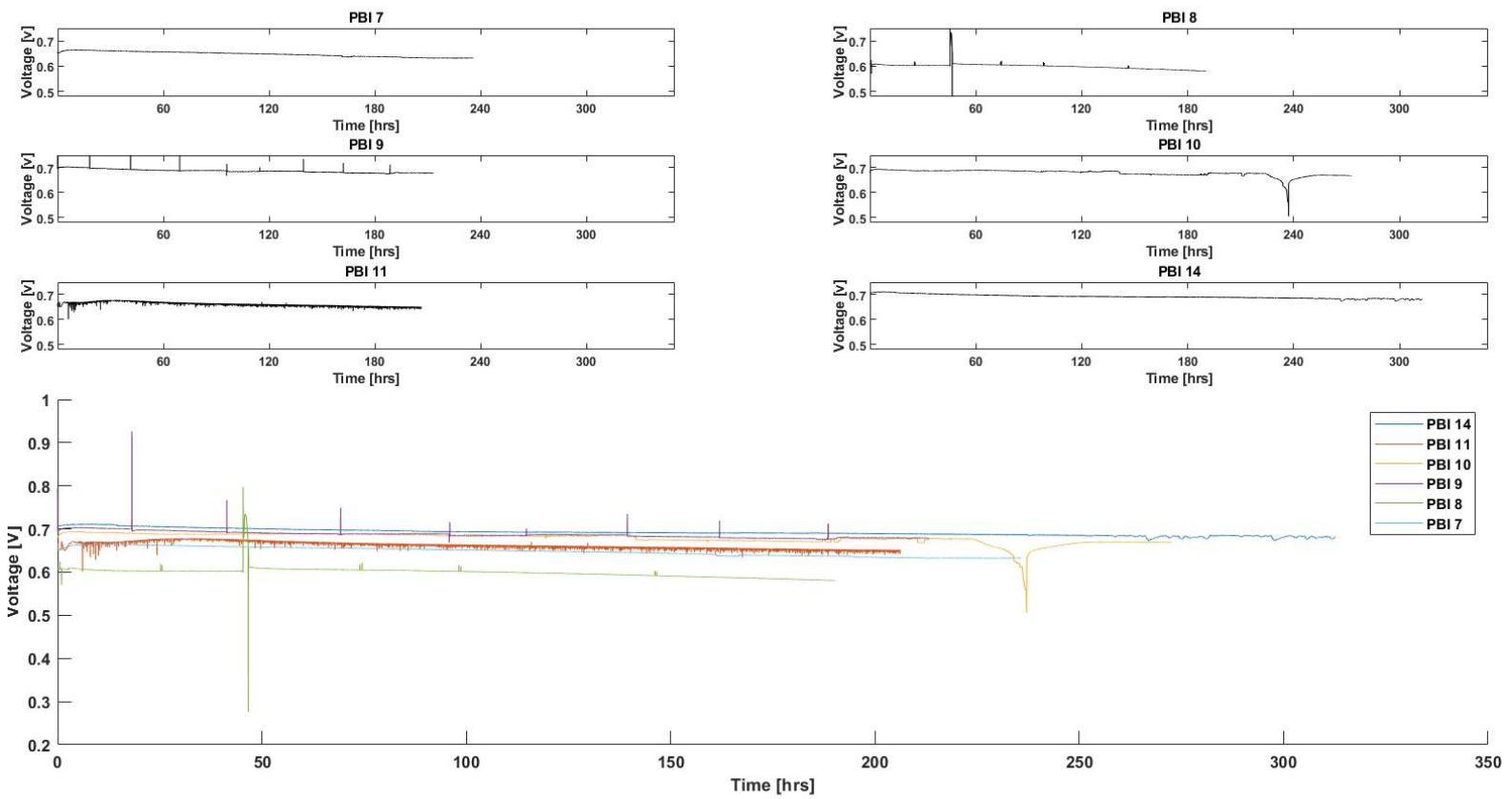


Figure 5.1: Results of voltage degradation experiments run with Advent PBI materials at 0.4 A/cm^2 , 200°C and atmospheric pressure (PBI 7,8), 200 kPa (PBI 9-11), and 300 kPa (PBI 14) with H_2/air stoichiometric ratios = $1.5/2$

The variations between the different testing conditions are outlined in Table 5.1. The goal for each study was to obtain a minimum of 200 hours of runtime data. For all but PBI 8 this was achieved. Testing ended early for PBI 8 due to a stand failure which resulted in damage to the MEA preventing further testing. As seen in Table 5.1 these experiments were run to investigate the impact of pressure and humidity on the voltage degradation of HT-PEM MEAs over time. Pressures tested here included 101 (atmospheric), 200 and 300 kPa. The humidity varied from 0-100% referenced at 85°C and was tested in both transient and continuous operation.

Table 5.1: Summary of durability tests and operating parameters

MEA	Test Setup	Pressure [kPa]	Temp [°C]	RH [@ 85°C]	Peak voltage [V]	Test duration [h]	Time to peak voltage [h]	Degradation rate [$\mu\text{V/h}$]
PBI 7	Stands1 + 2	101	200	0-100%	0.634	243.7	13.1	156.4
PBI 8	Stand 2	101	200	0-100%	0.607	190.1	0.6	140.0
PBI 9	Stand 1	200	200	0%	0.703	213.2	3.5	116.0
PBI 10	Stand 1	200	200	0%	0.693	272.6	5.6	92.3
PBI 11	Stand 2	200	200	30%	0.669	206.3	5.8	96.0
PBI 14	Stand 1	300	200	0%	0.711	312.7	5.0	103.0

Normalized Data

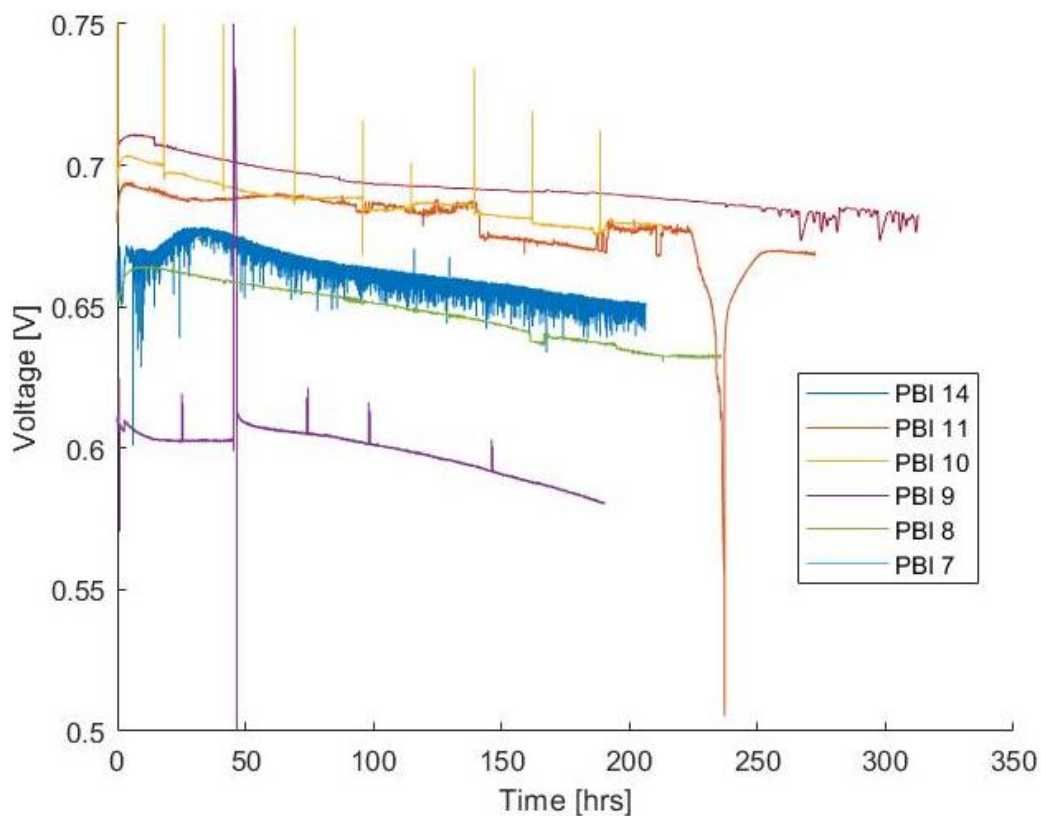


Figure 5.2: Normalized voltage degradation profiles at 0.4 A/cm^2 , 200°C with H_2/air stoichiometric ratios = 1.5/2, atmospheric pressure (PBI 7,8), 200 kPa (PBI 9-11), and 300 kPa (PBI 14)

Following the process outlined in Chapter 3 for normalizing and plotting the data, the profiles in Figure 5.2 were obtained. Normalizing the data in this way allows us to account for variations in MEA performance due to operating conditions or manufacturing variability. As seen in Figure 5.2, the variations in the peak voltages between each MEA in Figure 5.1 are eliminated. From this analysis, the slopes of the curves can be more easily compared to one another.

From the previous Chapters 3 and Chapter 4 we established a baseline voltage degradation rate of $136.4 \mu\text{V/hr}$ at the target operating conditions of 0.4 A/cm^2 , 200°C , atmospheric pressure and anode/cathode stoichiometric ratios of $1.5/2$. Table 5.1 shows a distinct decrease in the degradation rate related to increasing pressure. This can be seen in the results for PBI 9 through 11 operated at pressures at or above 200 kPa. PBI 7 and 11 were tested to assess the impact of humidity. The testing for PBI 11 included both a continuous humidity and a pressurization to 200 kPa, whereas PBI 7 varied several levels of humidity in both transient and continuous humidity modes. PBI 7 is an extension of the previously studied PBI 6 presented in Chapter 4. The results for each MEA are explained further with independent plots in the section below.

PBI 7

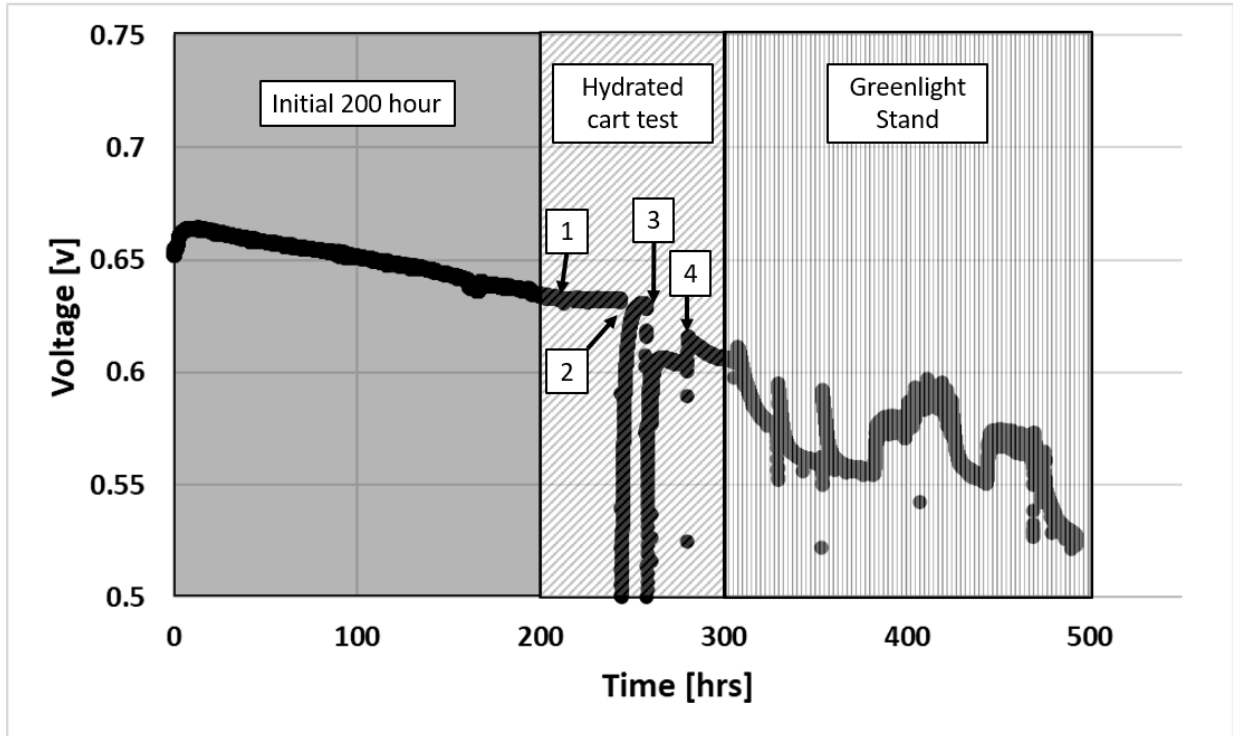


Figure 5.3: Voltage profiles of PBI 7 on stand 2 and stand 3 under varying operational conditions

The complete voltage profile for PBI 7 is presented in Figure 5.3 with three sections of the graph shaded with a different greyscale pattern and each corresponding to a different phase of the testing. From left to right there is the dark grey section labeled “Initial 200 hour”, the angled light grey hash marks labeled “Hydrated Cart Test”, and the grey vertical lined section titled “Greenlight Stand”.

Testing of this MEA began after the break in period with the conditions stated in the Chapter 4 for PBI 6: 200°C, 0.4 A/cm², atmospheric pressure, H₂/Air stoichiometric ratio of 1.5/2, and over 200 hours of runtime. The initial 200 hours of data can be seen in the first section of Figure 5.3 and

shows a typical linear decrease in performance over time, consistent with what we established for these conditions in the previous chapters.

After the initial 200 hours measurements it was decided to attempt to rehydrate the MEA. For this phase in the testing, which lasted about 100 hours, the MEA was renamed to PBI 7 to differentiate from the earlier testing under standard voltage degradation conditions as PBI 6. However, it is important to emphasize that this is the same physical MEA operated with a different testing protocol. In the second phase of the testing (i.e., middle zone in Figure 5.3), we looked at the impact of liquid water injections using the upgrades made to the in house fuel cell stand, referred to as Stand 1 in the Introduction section. Each of the boxes numbered 1-4 is a reference to a times of four different water injections.

Table 5.2: Liquid water injections for PBI 7

Injection	Volume [mL]	Injection method
1	0.1	Manual
2	0.3	Pneumatic
3	0.3	Pneumatic
4	0.3	Manual

Injection 1 was conducted by manual operation of a 1 mL plastic syringe to inject deionized (DI) water directly into the cathode gas line immediately upstream of the cell hardware inlet port. The Pneumatic method employed a automated dispensing device to accurately add DI water to the cathode gas line at the same location as the manual method. As seen in Figure 5.3, the impact of the first manual water injection can be seen as a flattening of the curve for several hours prior to

injection number 2. Based on these initial results, it was decided to increase the quantity of water for Injections 3 and 4 to 0.3 mL.

For Injection 2, the method was altered to utilize the pneumatic dispenser. It was anticipated that the device would simplify the injection process and provide a more repeatable result. Unfortunately, this method did not work as desired, while the root cause was not determined we speculated that it was due to an error made during the setup. Injection 2 resulted in a sharp decrease in voltage corresponding to the exact time the injection occurred. While the cell made a recovery to previous voltage levels in the hours following Injection 2 this was neither the desired outcome, nor what we had expected due to the previous success of Injection 1.

Believing that we had made a mistake during the setup of the pneumatic dispenser, we removed, retested, and reinstalled the system prior to repeating the test with Injection 3, however this attempt yielded even worse results, with voltage decreasing all the way to a negative voltage for a brief period. After this quick voltage drop, the voltage slightly increased and then began to decrease again, all at a voltage lower than prior to the injection.

At this point, we were unsure if the issue lay with the method, or the quantity of water used. The earlier manual injection method as repeated with the increased quantity of 0.3 ml of water for the 4th and final water injection. Unlike for Injection 1 but similar to 2 and 3 there was a slight decrease in the voltage immediately after injection, smaller in magnitude than the voltage drops seen in either Injections 2 or 3 but none the less is still observable. It was suspected that this decrease in voltage was due to a dilution or mass transport loss as the water reached the cell hardware, rapidly heated to 200°C and vaporized. Immediately after the decrease in voltage, Injection 4 resulted in a voltage increase of several millivolts.

After these injections, the profile of the voltage curve changed from linear to a nonlinear shaped curve with the voltage decreasing rapidly post injection. The issues with the liquid injections were suspected to stem from the rapid vaporization of water within the cell hardware. To overcome this hurdle the cell was cooled, purged with nitrogen, and the gas lines capped off to transfer the cell to Stand 2, as this apparatus was equipped with gas saturators while Stand 1 was not. The saturators allowed the humidification of the reactant gases without subjecting the cell to a sudden volume of liquid water as seen in the previous setup.

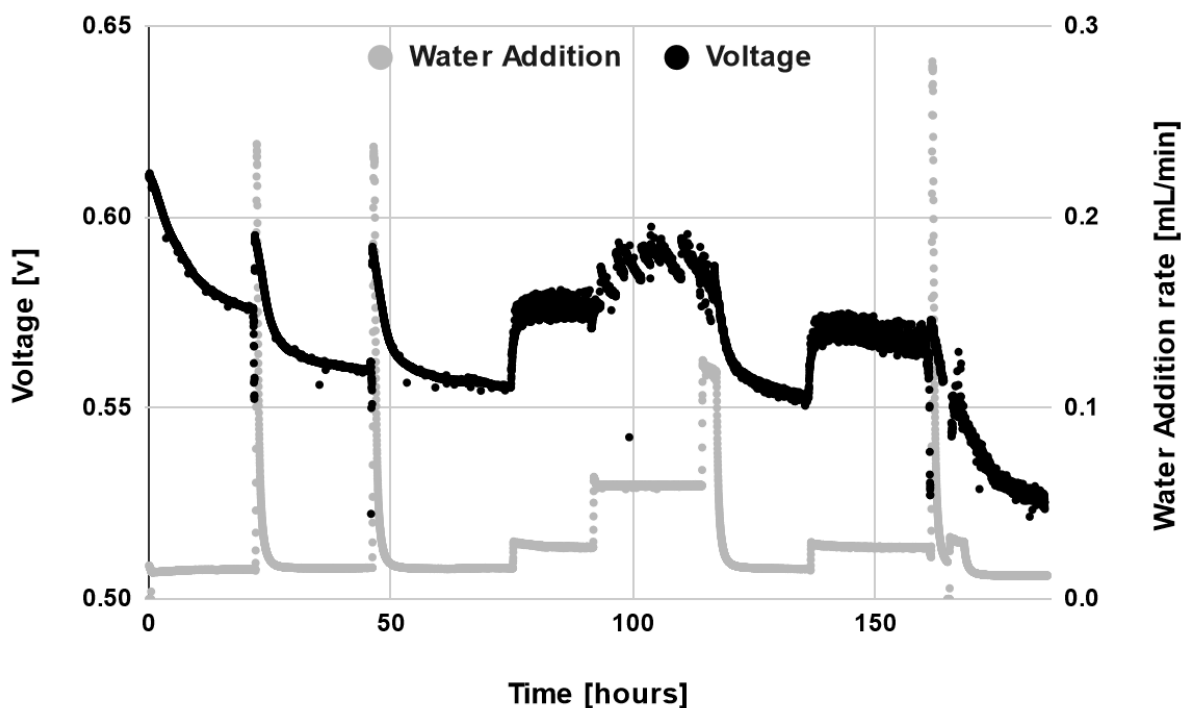


Figure 5.4: PBI 7 humidified operation expanded operation on stand 2

The data of the third shaded section in Figure 5.3 “Greenlight Stand” is expanded in Figure 5.4. The left-hand axis in Figure 5.4 shows the cell voltage and corresponds to the dark black symbols.

It is important to note that the scale of the voltage axis has changed to better display the data. The right-hand axis shows the water additions rate in mL/min and refers to the grey symbols.

After placing the cell on Stand 2, it was allowed to equilibrate for 24 hours. After this normalization period, the experiments on the transient addition of water undertaken previously on Stand 1 (first and second shaded zones in Figure 5.3) were continued. The water addition rate on the new setup was maxed out for 30 minutes then reduced back to zero and monitored for 24 hours. This was repeated twice and can be seen in Figure 5.4 as the 2 spikes in the water addition rate occurring at roughly 24 and 50 hours. The non-linear decay of the voltage seen after the two water additions is very similar to that of the Injection 4 in the previous experiments run on Stand 1.

One notable difference between the results of the previous experiments performed on Stand 1 and the current experiments presented in Figure 5.4 is the temporary decrease in voltage post water addition. While both setups saw an initial drop in voltage, the first setup saw a drop all the way to a negative voltage, the second setup only saw a drop of roughly 2.5 mV. This observation supports the hypothesis that the direct injection of liquid water was leading to obstruction of the reactants and that the switch to Stand 2 resolved the issue. The small drop in voltage in the second setup is attributed to the flow of gas through the saturators. When the saturators are engaged, the reactant gases are rerouted through a heated bubbler, and this change in gas flow is believed to account for the brief drop in voltage.

Interestingly, the voltage profile seen after these two additions is similar to the profile observed during the initial 24-hour equilibrium period. It is possible that during the cool-down and transfer between test stands some water was introduced or allowed to condense within the cell hardware and contributed to the unique shape of the voltage profile seen in Figure 5.4.

Moving away from the transient addition of water, we introduced a constant stream of humidified reactants after 50 hours in Figure 5.4, and varied the rate from 0.03 to 0.06, and finally 0.11 mL/min. The continuous addition of small amounts of water had a beneficial impact on the cell voltage. The addition of 0.03 mL/min resulted in a voltage increase of roughly 20-25 mV. The doubling of this rate to 0.06 mL/min also resulted in an increase in voltage, however, there was a decreasing benefit with the voltage only increasing a further 20 mV, with increasing level of voltage instability. Further increasing the water addition to 0.11 mL/min produced no voltage increase over the 0.06 mL/min rate. Under the continuous flow of 0.06 mL/min occurring around the 100-hour mark in Figure 5.4 the voltage becomes more unstable, and this trend will be explained in detail further in connection with PBI 11 where the effect becomes even more pronounced.

Through the associated increase in cell voltage, the addition of water under continuous or transient modes has been shown to have a beneficial impact on the performance of the HT-PEM fuel cell. While this is an interesting development as HT-PEM cells are often touted as not requiring external humidification, the improvement in performance was not the goal of this set of experiments. Here we set out with the goal of increasing the lifespan of a HT-PEM cell through the rehydration of the electrolyte. In Figure 5.4, after roughly 135 hours, we returned to a continuous rate of 0.03 mL/min with the intention of running under this condition for an extended period to determine a new (presumably lower) voltage degradation rate. Unfortunately, after roughly 165 hours the stand experienced an unexpected shutdown that can be seen by the increase in the water addition rate. It is unknown why the shutdown caused this spike in water addition, but upon restarting the stand the cell's performance seemed to have been permanently altered and the cell began degrading

rapidly. Testing on PBI 7 was completed after a second stand shutdown at 185 hours that resulted in the effective failure of the MEA.

PBI 8: Intermittent humidification

Following the experimentation on humidification with PBI 7, PBI 8 utilized a transient water addition method. Initially every 24 hours then every 50 hours after 100 hours total elapsed time, the cell was humidified with water for 30 minutes at a rate of 0.3 ml/min. This was done to investigate the effect of intermittent humidification on the cell over the course of a 200 hours run. The interval period of 24 hours was chosen to emulate a once daily humidification cycle that could be achievable for a commercial system. PBI 8 operated at 200°C, 101.3 kPa and 0.4 A/cm² for 190.1 hours. The full 200 hours was not completed due to an unintended stand shutdown at that damaged the cell as a result of an issue with the heater set up on Stand 2. Although the stand itself went into an unplanned emergency shutdown, the heating element of the cell continued to draw power. This caused the cell to sit with no gas flow or current draw at a temperature of 200°C for several hours. After baking in the cell hardware, attempts were made to restart the system but it was clear the MEA was no longer operational.

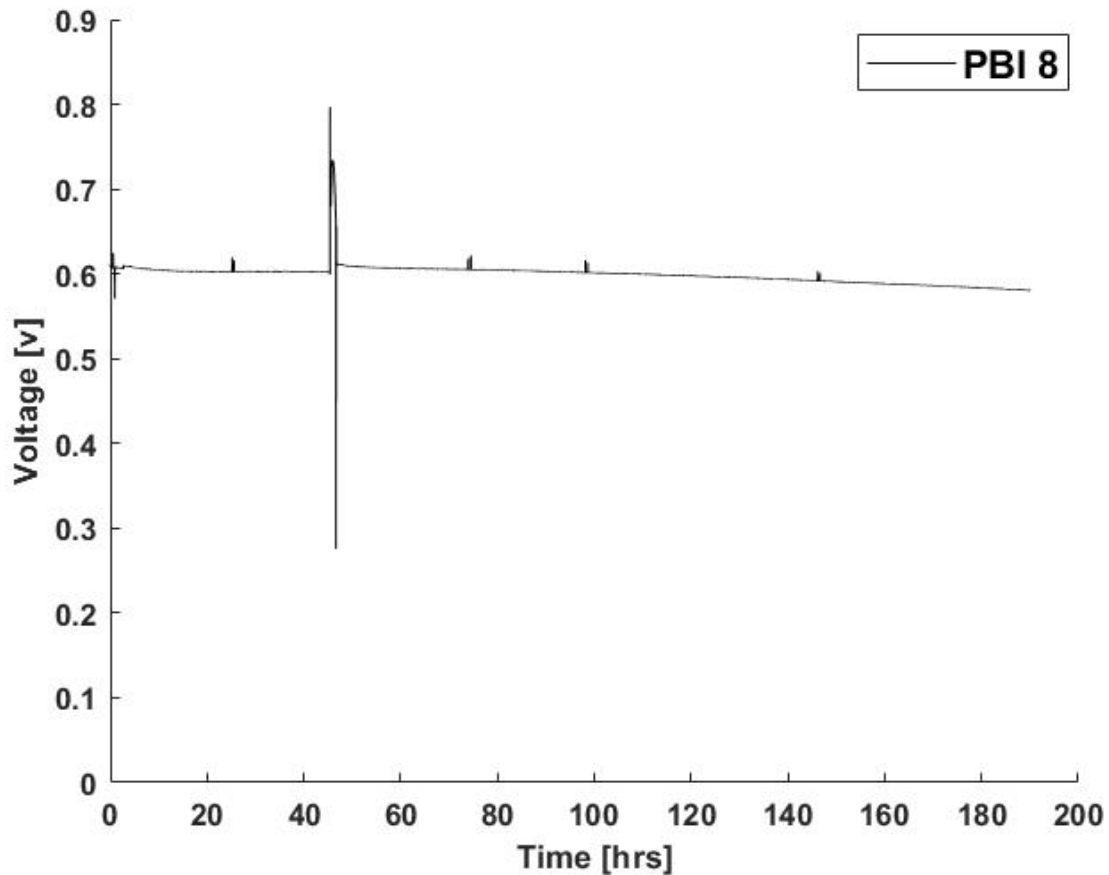


Figure 5.5: voltage degradation profiles of PBI 8 at 0.4 A/cm^2 , 200°C , 101.3 kPa with H_2/air stoichiometric ratios = $1.5/2$, and intermittent humidification

In Figure 5.5 at 48 hours there is a large fluctuation in voltage. This fluctuation corresponds to the second, 30-minute humidification period. It is unknown what caused this voltage change as nothing unique happened during this event when compared to the other humidification periods. During the 30-minute period, the voltage varies from a low of roughly 0.28 V to a high of around 0.81 V . The 24 hours humidification interval was derived from the initial success of the transient water experiments in PBI 7. It was hypothesized that the humidification of the cell would rehydrate the MEA, improving the conductivity and recovering/preventing performance loss. However, the

measured degradation rate of 140 $\mu\text{V}/\text{h}$ showed no improvement over the previously established rate of degradation for PBI-based HT-PEM cells run at the same nominal operating conditions.

PBI 11 Continuous Humidification and pressure

With the results of minimal performance or durability improvements from transient and intermittent humidification observed for PBI 8, a continuous humidification regime was tested with PBI 11. It was expected that as the intermittent humidification had not yield any observable results, being neither better nor worse than the baseline operation, continuous humidification would introduce more water to the system and generate some response from the cell. Here the same nominal temperature and current density conditions of 200°C and 0.4 A/cm² were used, however the cell was humidified at a rate of 0.09 mL/min with increased pressure of 200 kPa. Testing was performed on the Stand 2 setup. Unfortunately, as can be seen in Figure 5.6, the voltage fluctuated widely during this test, bringing the validity of the results into question.

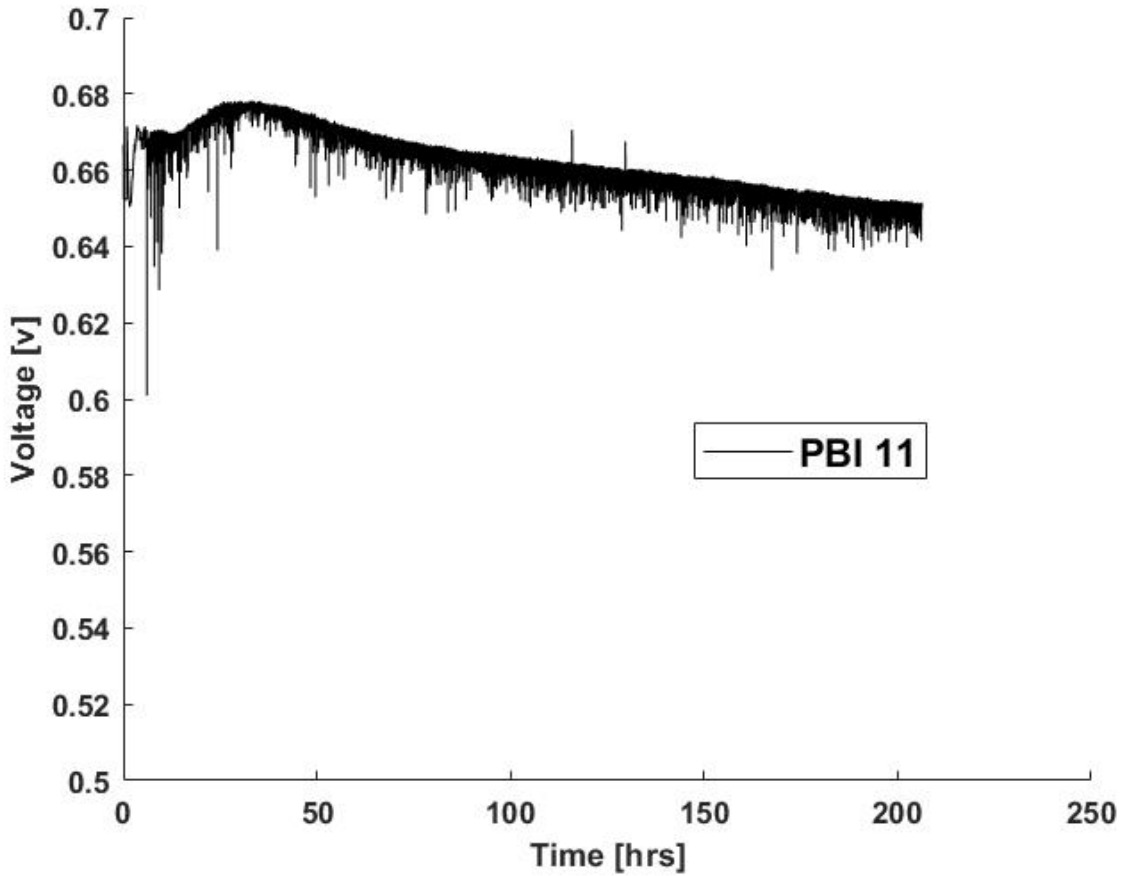


Figure 5.6: voltage degradation profiles of PBI 11 at 0.4 A/cm^2 , 200°C , 0.09 ml/min , and 200 kPa with H_2/air stoichiometric ratios = $1.5/2$

To identify the cause of the voltage fluctuations observed in Figure 5.6, each parameter logged from the test was plotted against the cell voltage over time. There were many parameters logged by the stand including pressure, temperatures, humidity, and flow rates all representing different locations and components of the stand. Among these parameters, an anomaly was identified in the cathode inlet pressure, and it was discovered to coincide with the fluctuations in voltage.

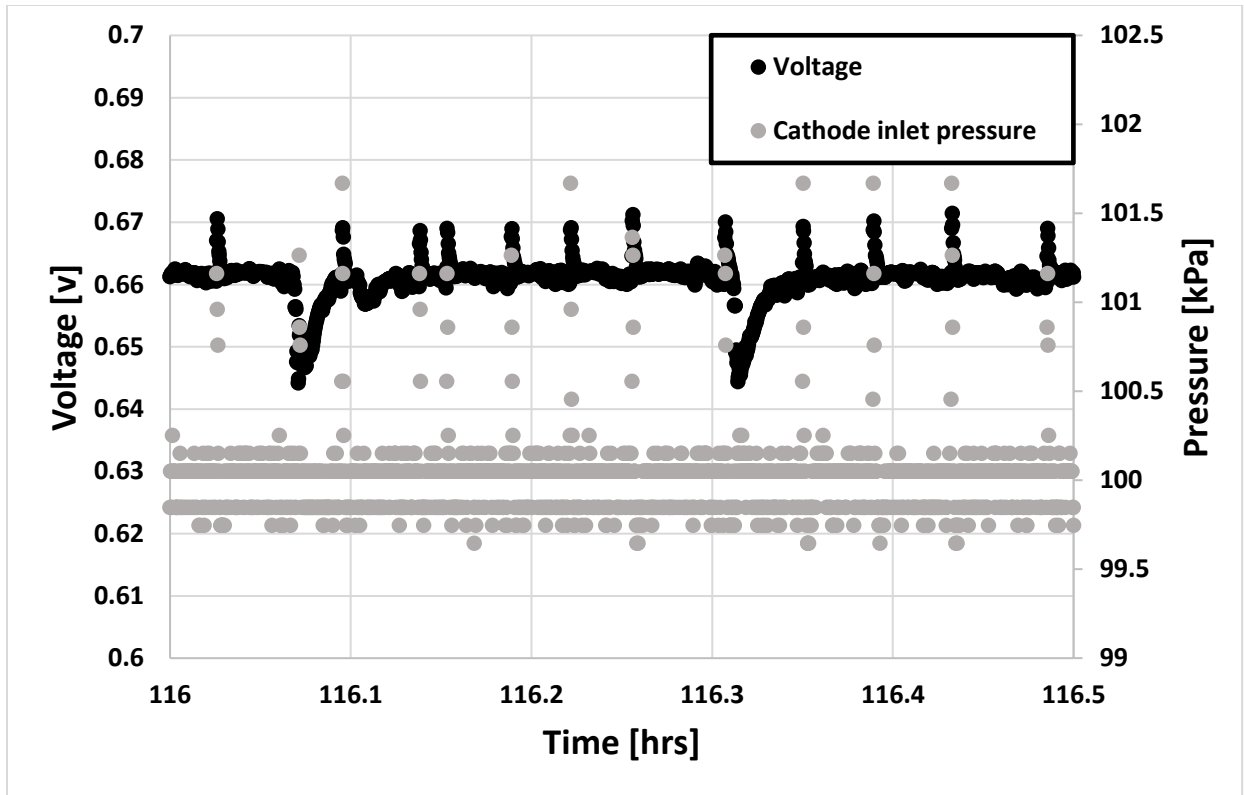


Figure 5.7: Impact of pressure fluctuations on voltage, PBI 11

Figure 5.7 presents the cell voltage with the black symbols (left y-axis) and cathode inlet pressure with grey (right axis). The x-axis ranges from 116 to 116.5 hours due to the resolution required to observe the pattern in fluctuations. This time period does not have any significance and was chosen arbitrarily to observe the correlation between cathode pressure and voltage fluctuations that occurred during all stages of the test. The noise in the voltage signal observed during the testing period was found to coincide with a clicking sound emanating from the rear of the fuel cell stand. Further investigation found that the clicking sound originated from a solenoid controlling the inlet water to the cathode saturator. Based on the recorded data and the observed noise, it is believed that the opening of the solenoid to maintain water level in the cathode saturator caused an increase in the pressure resulting in the fluctuation in the cells voltage seen in Figures 5.6 and 5.7.

Effect of Pressure

The dehydration of phosphoric acid, identified previously as a suspected driver behind the increased degradation rate of these cells at 200°C, prompted the experiments at above ambient pressure. The effect of pressure on a fuel cell is well understood and increases in pressure are known to result in increased voltage as per Equation 1[1].

$$\Delta V = V_2 - V_1 = \frac{RT}{4F} \ln \left(\frac{P_2}{P_1} \right) + A \ln(B) + C^{Di} \quad (\text{Eq 5.1})$$

In practice, the increase in voltage gained due to pressurization comes at the cost of the higher power draw of the associated air machinery. The discussion in this section does not focus on the performance impact of pressurization as the findings of this research agree with the established work on the performance impact of pressurization. This section will focus on the impact of approaching the vapor pressure of phosphoric acid at 200°C on the degradation of a HT-PEM cell.

PBI 9 and 10

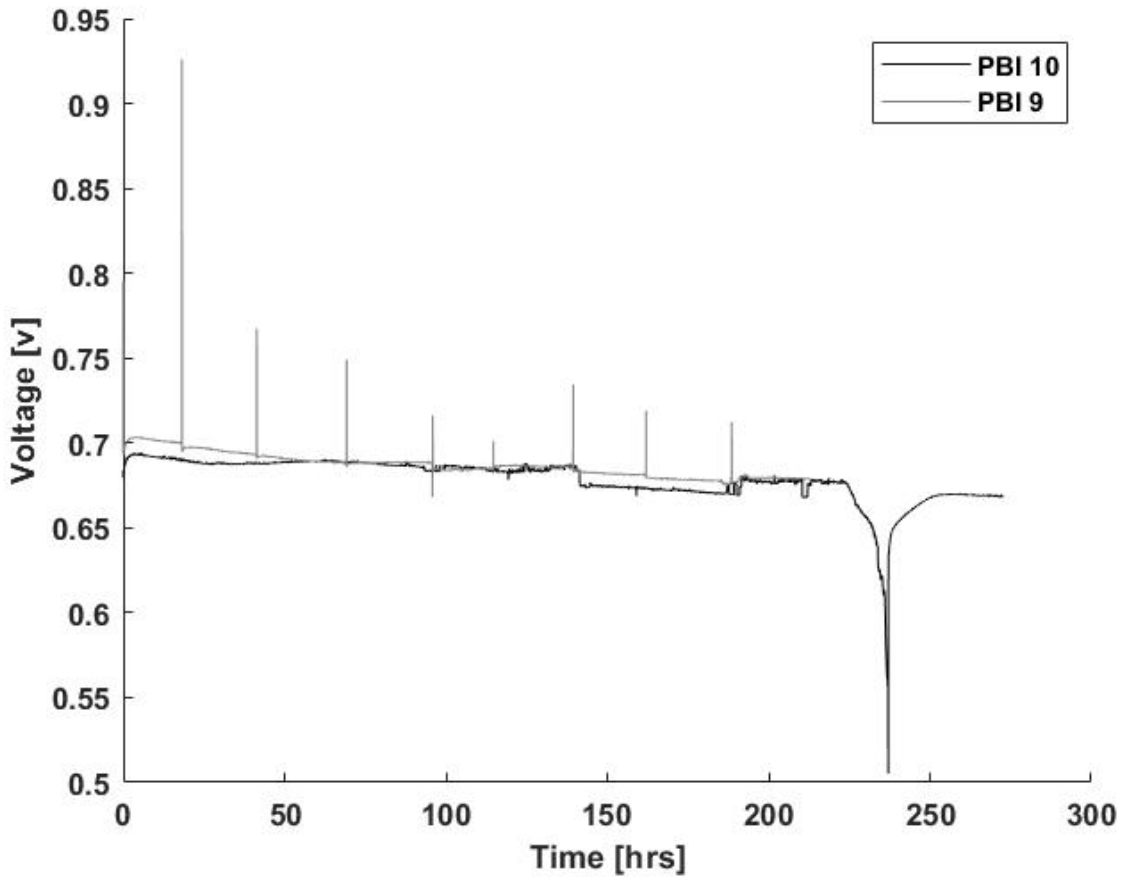


Figure 5.8: voltage degradation profiles of PBI 9 and 10 at 0.4 A/cm^2 , 200°C , 200 kPa with H_2/air stoichiometric ratios = $1.5/2$

For the data presented in Figure 5.8, both PBI 9 and 10 were operated at 200°C , 0.4 A/cm^2 , and 200 kPa for $200+$ hours on Stand 1. PBI 9 can be differentiated from PBI 10 in Figure 5.8 due to the fluctuations seen every 24 hours. This difference between the two data sets stemmed from the testing protocol, not a difference in MEA type or operational parameters. During testing for PBI 9, the water collection vessel used for pH and water quantity data was emptied every 24 hours along with a daily HFR measurement. A two-valve airlock style setup was designed and employed to minimize pressure fluctuations during this daily event. However, from the voltage profile of

PBI 9 in Figure 5.8 it seems that this setup did not entirely reduce the pressure fluctuation/ impact of HFR on the cell during testing. For testing of PBI 10, which actually preceded PBI 9, the stand was reconfigured to hold all product water for the duration of the testing and HFR measurements were made only at the beginning and end of testing.

In Figure 5.8, PBI 10 shows a gradual decline and then recovery in voltage after roughly 225 hours. This was due to a lab issue that resulted in a loss of hydrogen flow. As the hydrogen supply gradually lost pressure and flow in the line decreased, the voltage dropped. The quantity of flow was not known over that period, however, after the hydrogen supply was restored, the voltage increased to match previous values before the loss of hydrogen supply. The degradation rate was calculated using values prior to the hydrogen supply issues and the remainder of the test after 225 hours was only continued and included here as an interesting point on the impact of stoichiometry on fuel cell operation.

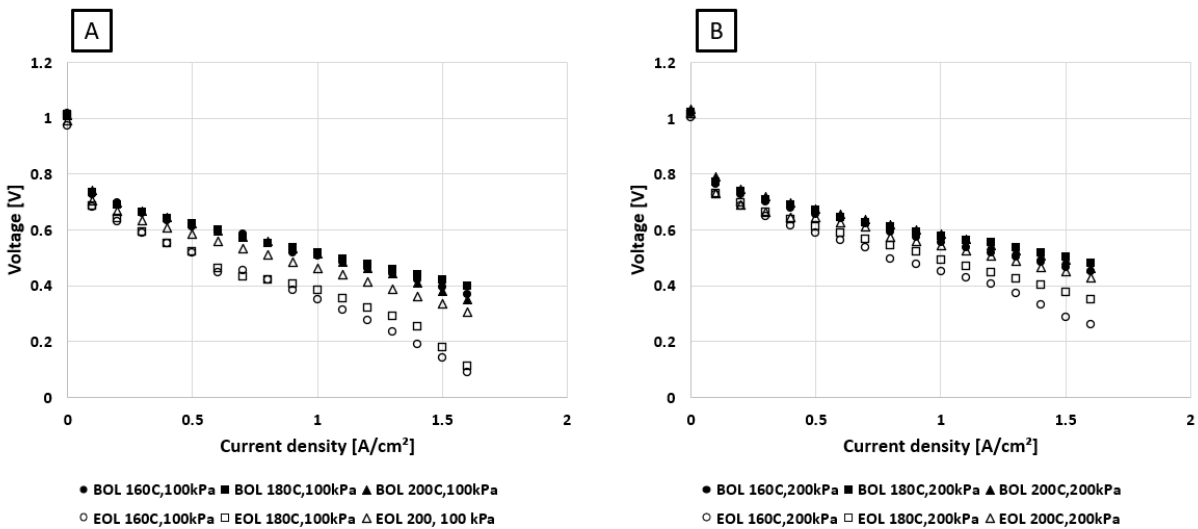


Figure 5.9: Polarization curves for PBI 9 measured at beginning-of-life (after break-in) and end-of-life (at completion of durability testing) for temperature of 160, 180 and 200°C at 101.3 kPa (figure A) and 200 kPa (figure B)

The polarization (POL) curves in Figure 5.9 above cover three different temperatures and two different pressures for beginning-of-life (BOL) and end-of-life (EOL). Measurements were taken after the break-in and before cooling the stand at the end of testing, respectively. The order of the POL curve testing was: 160,180, and finally 200°C at 100kPa, then the same order of temperatures at 200kPa during BOL testing. At EOL this order changed to 200, 180 and finally 160°C at 200 kPa. After the 200 kPa tests, the cell was depressurized to 100 kPa and the polarization curves proceeded first with 160, then 180 and finally 200°C. This order was chosen to minimize the temperature and pressure fluctuations on the cell. As expected, a trend of higher voltage performance at higher temperatures can be seen across all curves with the end-of-life POL curves in Figure 5.9A (101.3 kPa) showing greater change over life than Figure 5.9B (200 kPa). This may indicate more about the effect of depressurization on the cell than a loss of performance due to MEA degradation over time. For POL curves at both 100 and 200 kPa, Figure 5.9 shows a downward translation indicating an increasing ohmic loss in the system as well as an increase in performance loss at higher current density that is indicative of a mass transport effect. The mass transport loss appears to be more pronounced in the 100kPa curves (Figure 5.9A).

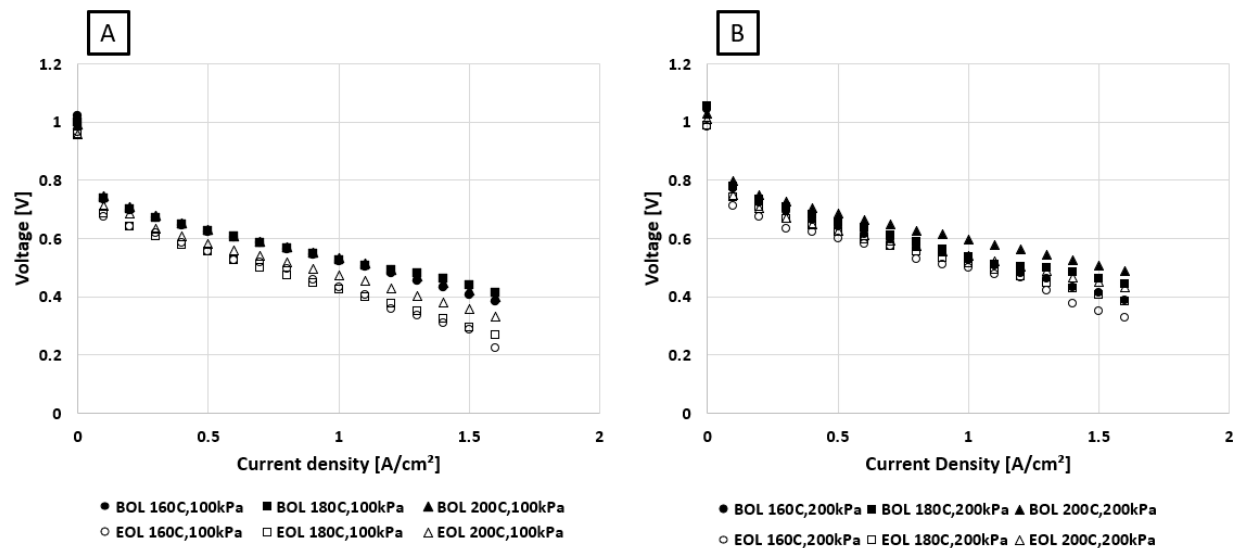


Figure 5.10: Polarization curves for PBI 10 measured at beginning-of-life (after break-in) and end-of-life (at completion of durability testing) for 3 temperature 160,180,200°C at 100 kPa (figure A) and 200 kPa (figure B)

The POL curves were repeated using a similar protocol for PBI 10 (Figure 5.10). The same trends with temperature and pressure seen for PBI 9 previously were observed for PBI 10. A key difference between the two cells is the reduction in the voltage loss at higher current densities, indicating a reduced mass transport effect in addition to a lower ohmic loss over the entire range of current densities. This may be due to the difference in testing protocols, with PBI 9 undergoing a slight depressurization due to water collection and a current fluctuation due to HFR measurement every 24 hours, while PBI 10 was not subjected to these periodic measurement cycles. The larger performance loss seen in the POL curves of PBI 9 compared against PBI 10 is also reflected in the calculated degradation rate of the cell over time in Table 1: 116 $\mu\text{V/h}$ for PBI 9 versus 92.3 $\mu\text{V/h}$ for PBI 10.

PBI 14

Chapter 4 previously reported an average voltage degradation rate of 136.4 $\mu\text{V/h}$ using the same test apparatus . PBI 9 and PBI 10 both showed improvements against the baseline test data in Chapter 4. With the relatively small magnitude of the change and small sample size with only two tests to draw from, it is difficult to state confidently that the observed improvement is statistically significant. However, building off the apparent improvement in durability observed with increasing system pressure to 200 kPa (PBI 9 and PBI 10 PBI), cell PBI 14 was operated with pressure further increased to 300 kPa (Figure 5.11).

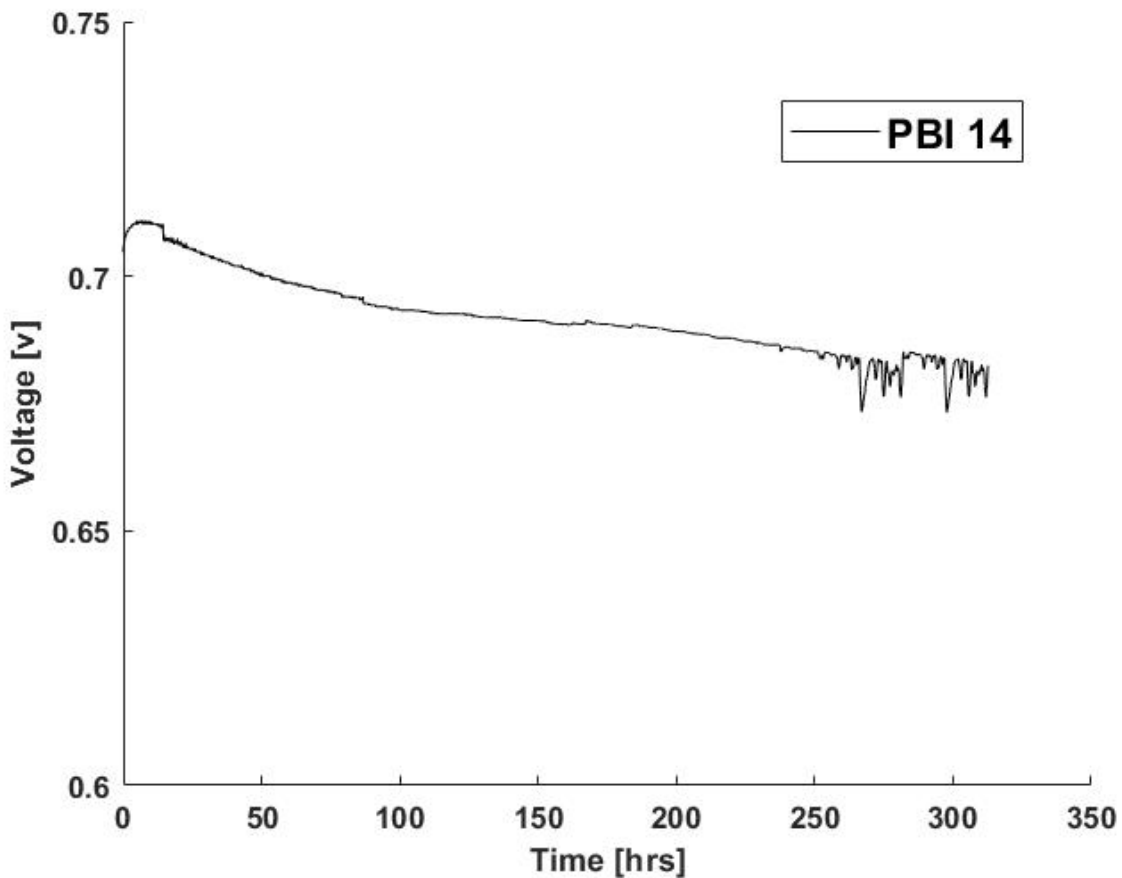


Figure 5.11: voltage degradation profiles of PBI 14 at 0.4 A/cm², 200°C, and 300 kPa with H₂/air stoichiometric ratios = 1.5/2

Two inconsistencies jump out immediately in the voltage profile presented in Figure 5.11. The first is the step down the voltage takes at roughly 20 hours. It is unknown what caused this downward voltage change, and it most certainly had a negative impact on the degradation rate calculation.

The second major inconsistency is the voltage fluctuation beginning after an elapsed time of 225 hours, about 75 hours from the end of testing. This resulted from a buildup of water in the anode exhaust water trap. Figure 1.4 in the Introduction outlines the construction of the stand where the water trap can be seen. As the water trap filled, the anode exhaust flow became submerged and resulted in bubbling. With the pressure building in the system, a bubble of gas would be pushed out of the anode exhaust, lowering the pressure in the stand and causing voltage fluctuations. The purpose of the trap was to allow the collection of the water exiting the anode of the system.

As seen by the inconsistencies in voltage every 24 hours in PBI 9 (Figure 5.8) the water could not be drained from the stand during pressurized testing. The water trap was designed to be as small as possible to limit the volume of hydrogen present in the stand for safety purposes. The rate of water collected from the anode during past experiments was used to calculate the size of the water trap needed for a 200-hour run. As can be seen in Figure 5.11, this worked well as the cell made it past 200 hours before filling the water trap. The data beyond 225 hours, when the voltage fluctuations begin, was not used in the degradation rate calculation and was only included to demonstrate the significant effect of varying back pressure on the cell performance and voltage stability.

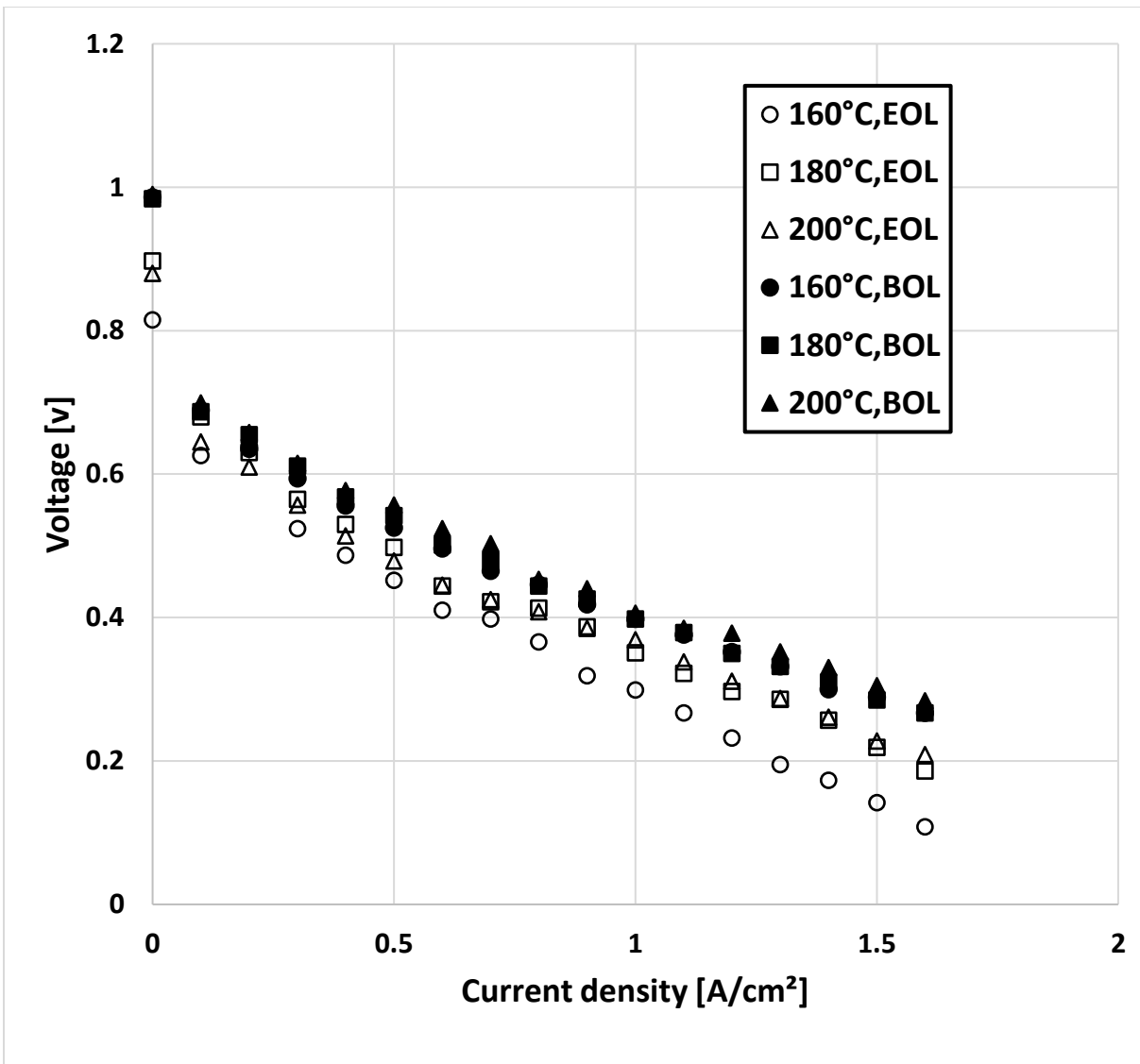


Figure 5.12: Polarization curves for PBI 14 measured at beginning-of-life (after break-in) and end-of-life (at completion of durability testing) for 160,180,200°C at atmospheric pressure

Figure 5.12 shows the POL curves for PBI 14. Due to the pressure of 300 kPa the stand could not handle both the flows of running at higher current densities and the pressure. No pressurized POL curves were run here. The MEA showed a trend of increasing performance across the board with increasing temperature, and a decrease in performance between BOL and EOL. For PBI 14 an ohmic loss appears to be dominating the performance loss of the cell over the run time.

Impact of pressure fluctuations

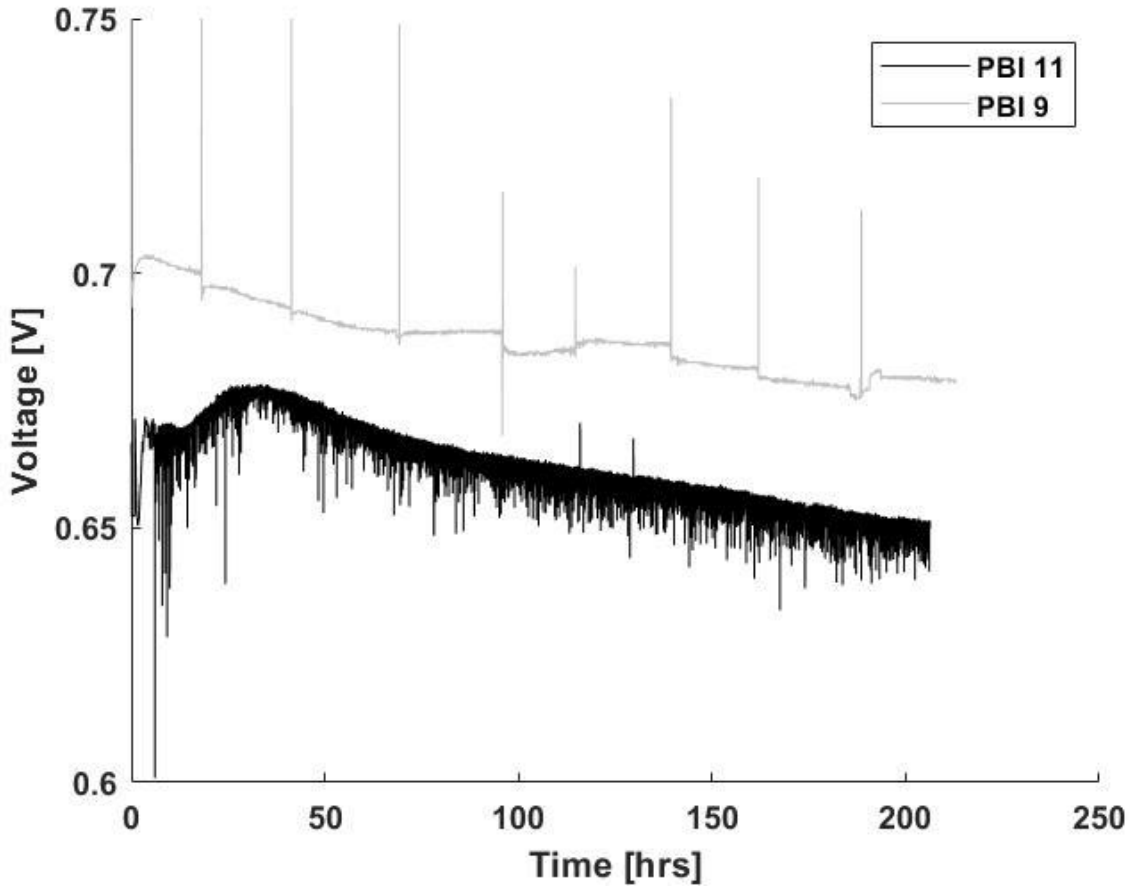


Figure 5.13: PBI 11 vs PBI 9 effect of pressure fluctuations

In both PBI 11 and PBI 9 pressure fluctuation played a significant role in the visible noise of the voltage profiles. Figure 5.13 contrasts the voltage profiles of both MEAs to further investigate the impact of this pressure change on the cell performance. Both MEAs underwent a 200 kPa testing cycles and had reduced voltage degradation rates when compared against the previously established baseline (Chapter 4). Comparing these two against the other pressurized experiments run shows that the impact of the pressure fluctuations on cell durability must not be significant. This conclusion stems from the fact that all the pressurized tests had comparable degradation rates regardless of the degree of pressure fluctuations.

For PBI 9, we do not have any pressure data to compare the voltage noise against. For the first three spikes in voltage leading to the fourth event at roughly 100 hours, the voltage returns to a value consistent with the previous trend. After 100 hours, this seemingly changes with the daily procedure creating a permanent translation and the profile becomes more erratic. As we do not have pressure data for this test, it can only be speculated what may be the underlying cause. It may be that the repeated opening of valves introduced a leak somewhere in the system allowing a slight change in pressure over time.

Returning to Figure 5.7 and the impact of pressure fluctuation on PBI 11, a change in pressure of around 2 kPa corresponds to a change in voltage of around 0.01 V. In fact, over the course of the test for PBI 11, there is never a recorded pressure change of more than 2.2 kPa. However, this may be where the error lies. Fuel cell Stand 2 internally averages the values for each data point over a one-minute interval. For a parameter which may vary rapidly with an activated solenoid valve, the pressure would momentarily jump then re-adjust allowing neither the magnitude of the voltage change nor the pressure swing to be accurately recorded.

Water and pH measurements

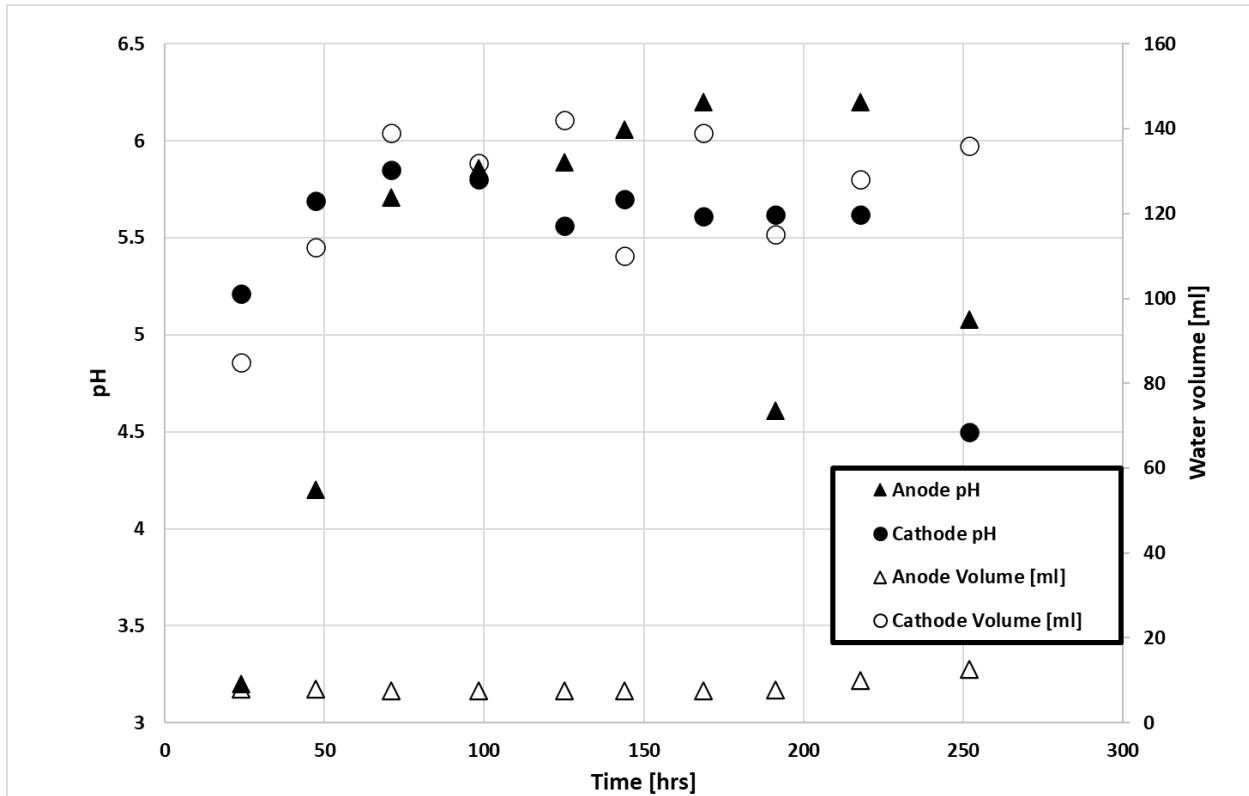


Figure 5.14: pH and volume of water collected at both cathode and anode exhaust for PBI 9

The pH and water volume data collected during testing of PBI 9 is presented in Figure 5.14. The solid symbols correspond to the pH and the left-hand axis, while the open symbols correspond to water volumes and the right axis. Both the anode and cathode pH show a similar trend with initially low values that level off to around 5.75. The first measurement on the anode side had a lower pH of around 3.25, and twice near the end of the test dropped to lower values. Even with the lower pH on the anode side, the majority of the phosphoric acid is assumed to migrate out the cathode due to the far greater quantity of water collected at that side.

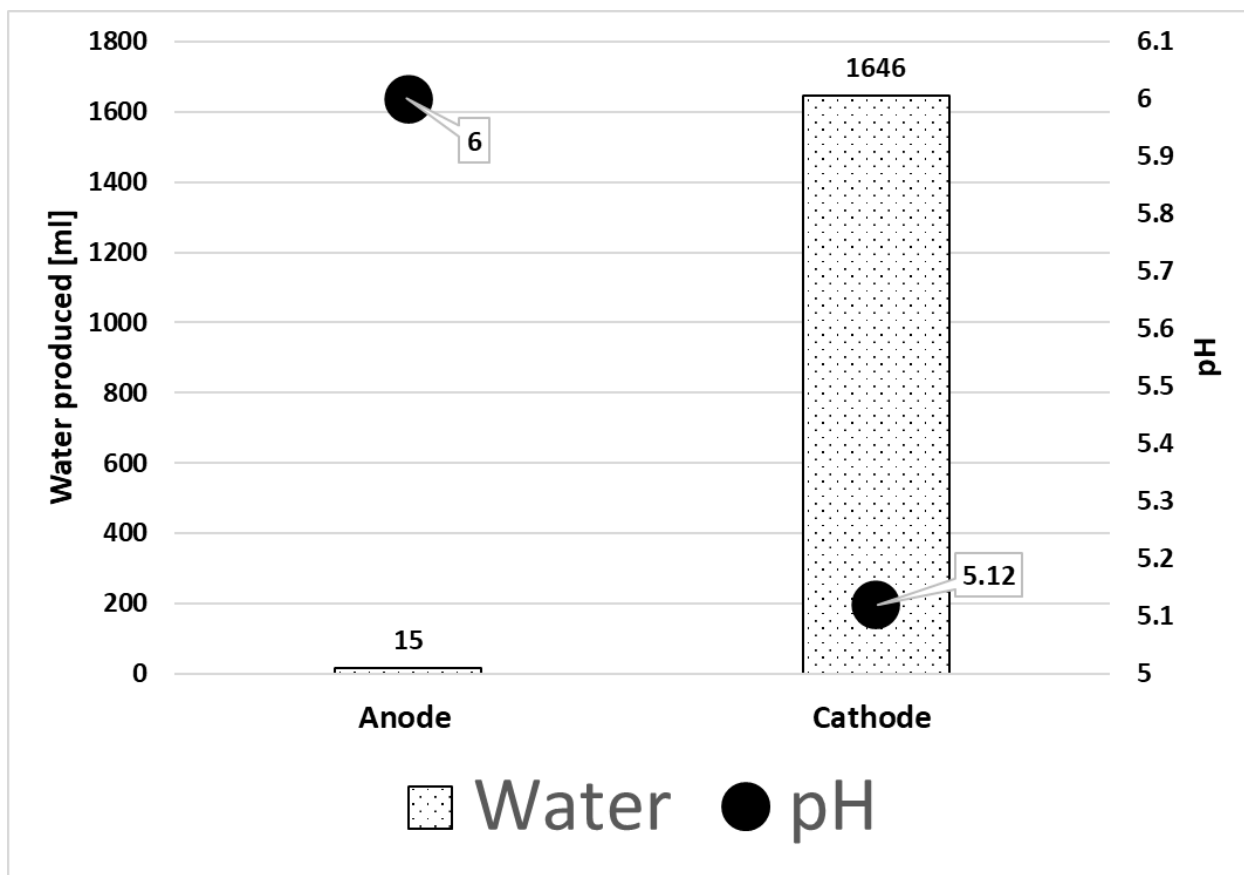


Figure 5.15: pH and volume of water collected at both cathode and anode exhaust for PBI 10

Unlike PBI 9 (Figure 14), for PBI 10 (Figure 5.15) we did not periodically collect and measure the water samples during testing. Here the dots represent the pH on the right-hand axis and the shaded bars are the volume of water produced on the left axis. The water was allowed to collect in traps and then removed after the completion of testing. Unlike in the previous pH measurements with PBI 9, PBI 10 saw a lower pH on the cathode side however a far greater volume of water was still collected on the cathode side.

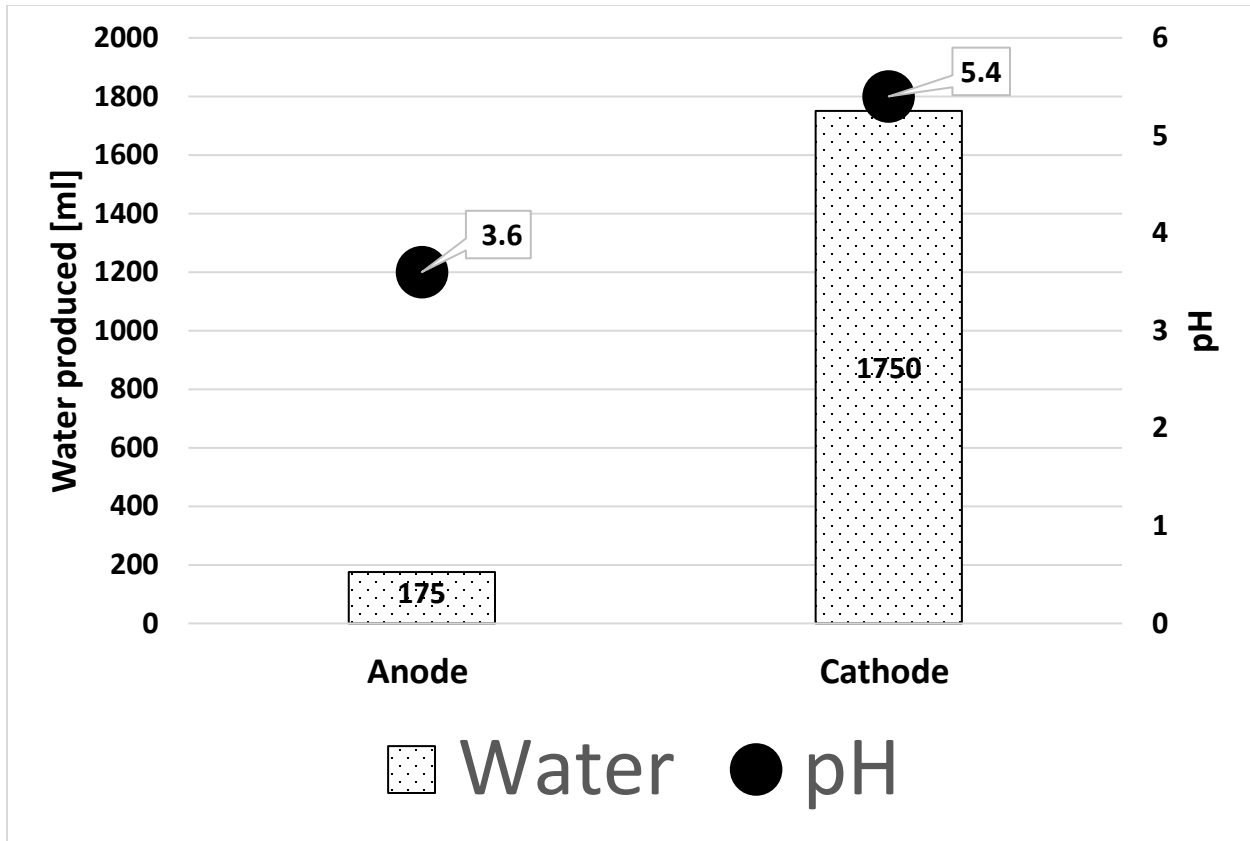


Figure 5.16: pH and volume of water collected at both cathode and anode exhaust for PBI 14

For PBI 14 (Figure 5.16), an increase in anode water content was observed over that collected for PBI 10, in line with the volume collected from the anode of PBI 9. The differences between PBI 10 and PBI 14 include both the increased volume of water in the anode and the anode pH, lower in this run indicating a greater loss of acid out of the anode than in PBI 10. It is believed that the relatively small amounts of water collected at the anode exhaust result from the net back diffusion effect working against electro-osmotic drag within the MEA.

$$\text{Water production } \left[\frac{\text{mL}}{\text{hr}} \right] = 0.3348 \times \frac{P_e}{V_c} \quad (\text{Eq 5.2})$$

Using equation 5.2 above the rate of the water production from the electrochemical reaction can

be calculated during steady state operation for our given operating parameters [2]. Here P_e represents the power production of the cell and V_c is the voltage of the cell.

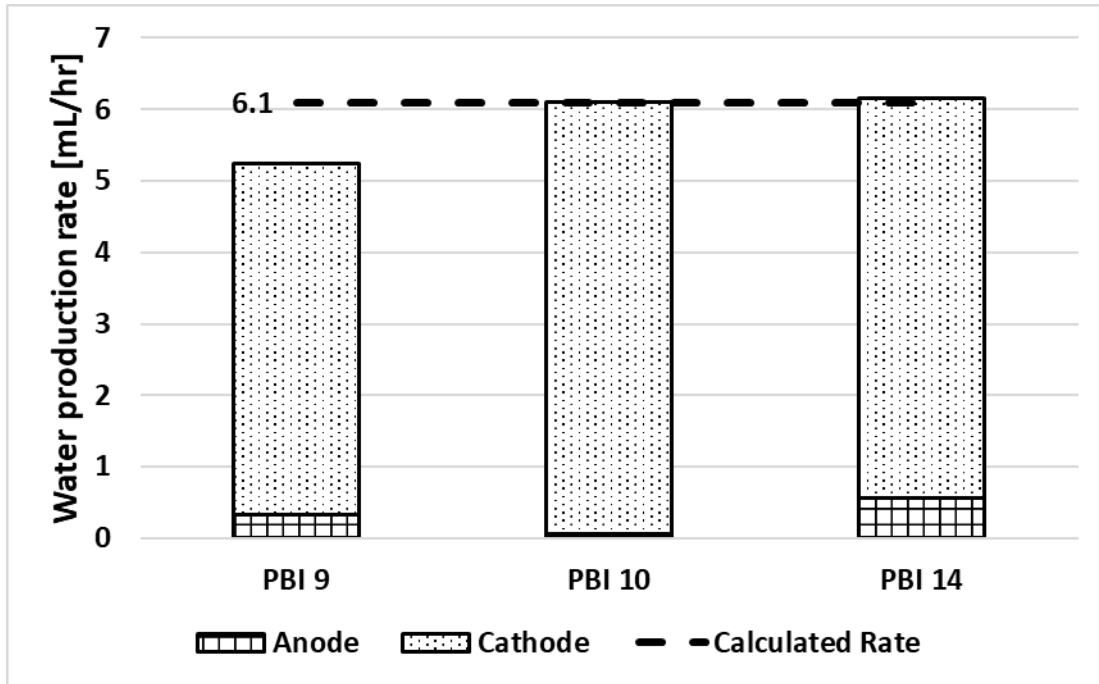


Figure 5.17: Net volume of water collected compared against calculated water production rate for PBI 9, 10, and 14

Figure 5.17 compares the value for the water production rate from equation 5.2 above with the measured rate of water production. This was done by taking the total volume of water collected and dividing it by the run time. The value for the calculated water production rate is 6.1 mL/h and is represented in Figure 5.17 as a dashed line with the value 6.1 mL/h. The columns present the total measured water production rates, with separate contributions from anode and cathode sides. While PBI 10 and 14 agree closely with the calculated rate of water production, the experimental result for PBI 9 is about 15% lower than the computed value. This is likely due to the distributed measurement method for the test that divided the water measurement into smaller sample sizes, thus compounding the error over the span of the test.

High-frequency resistance (HFR)

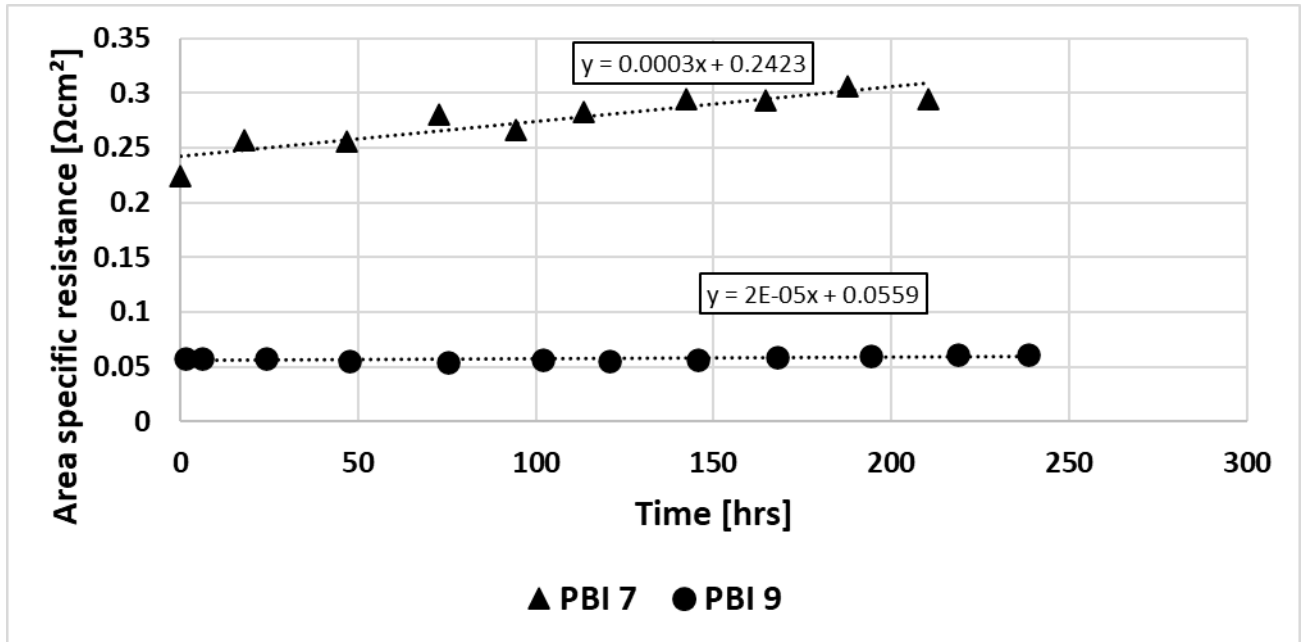


Figure 5.18: High-frequency resistance (HFR) as a function of time for PBI 7 and PBI 9

Following the same time interval as the water sample collections, the resistance of the cell was measured using high-frequency resistance (HFR) for both PBI 7 and 9 (Figure 5.18). For PBI 7, an upward trend in resistance over time was observed and assumed to be linear with a best fit line and equation displayed with the data. The data for PBI 7 were acquired during the baseline durability experiment prior to any water injection testing. Compared to PBI 7, PBI 9 showed little to no increase in resistance over a similar testing period. This was an interesting result, as PBI 9 was run at 200 kPa. It is worth noting that among the baseline measurements, PBI 7 had the highest degradation rate at 156 $\mu\text{V/h}$ which may exaggerate the effect of pressure on cell conductivity change seen here.

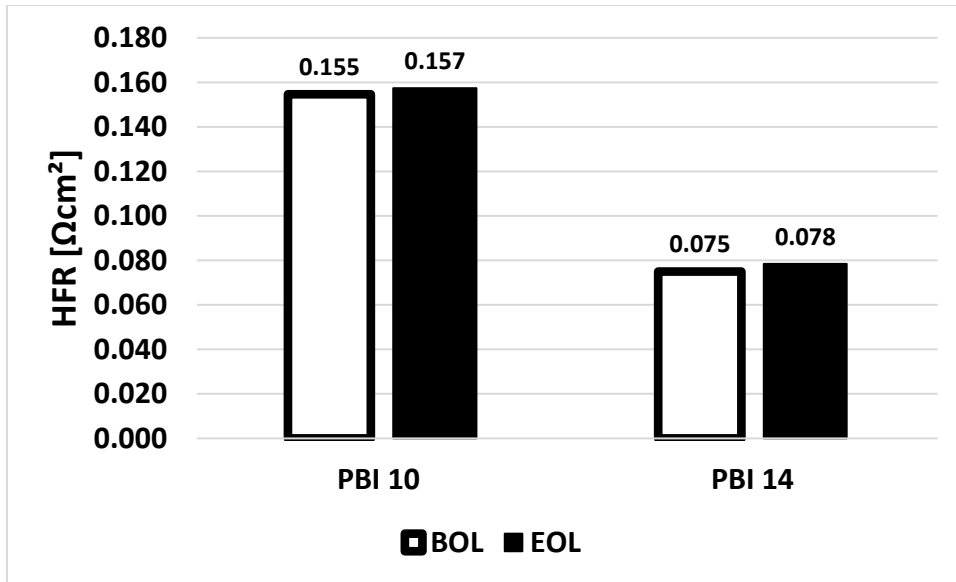


Figure 5.19: BOL and EOL measurements of HFR for PBI 10 and 14

The HFR measurement followed the procedure used for water sample collection. For PBI 10 and 14, the measurements were taken only at the beginning of testing after the break-in procedure, and at the end of testing. This was done to minimize the impact of the HFR measurement on the cell durability test as seen with the voltage fluctuation of PBI 9. For PBI 10 and PBI 14 shown in Figure 5.19 there was only a slight increase in resistance over the course of the test.

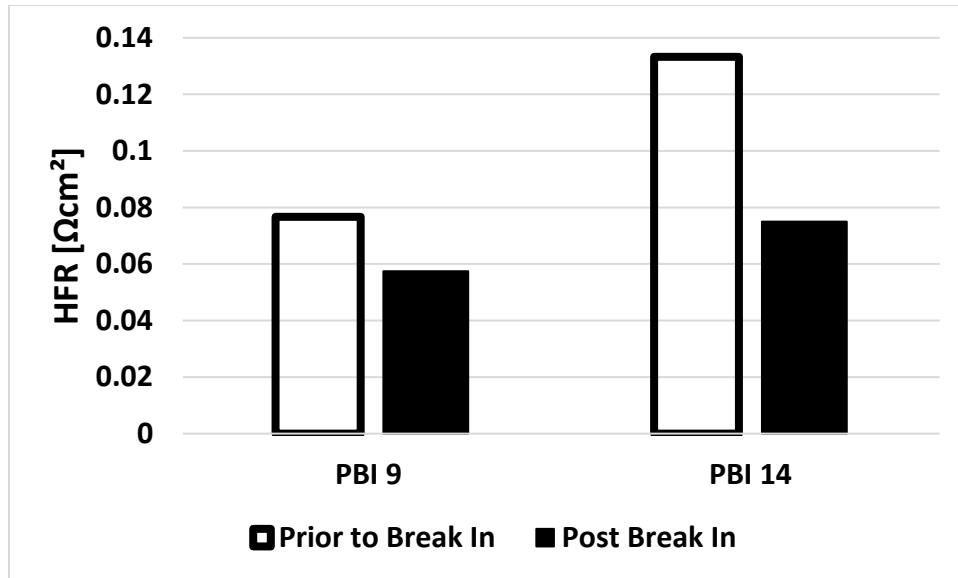


Figure 5.20: Effect of break in procedure on HFR for PBI 9 and 14

Figure 5.20 shows the impact of the break-in procedure on the HFR measurement of the cell for PBI 9 and 14, by measuring the HFR immediately before and after the 24-hour break-in cycle at 0.2 A/cm², 160°C and 101.3 kPa. In both cases, there was a significant decrease in the HFR over this period which in magnitude is greater than the increase seen over the course of testing previously discussed in Figures 5.18 and 5.19. It is believed that the reduction of the HFR measurement of the cells was due to an initial redistribution and rehydration of phosphoric acid within the MEA. This change in the concentration and distribution of the phosphoric acid increases the conductivity of the MEA decreasing the HFR measurement.

Phosphorus acid content

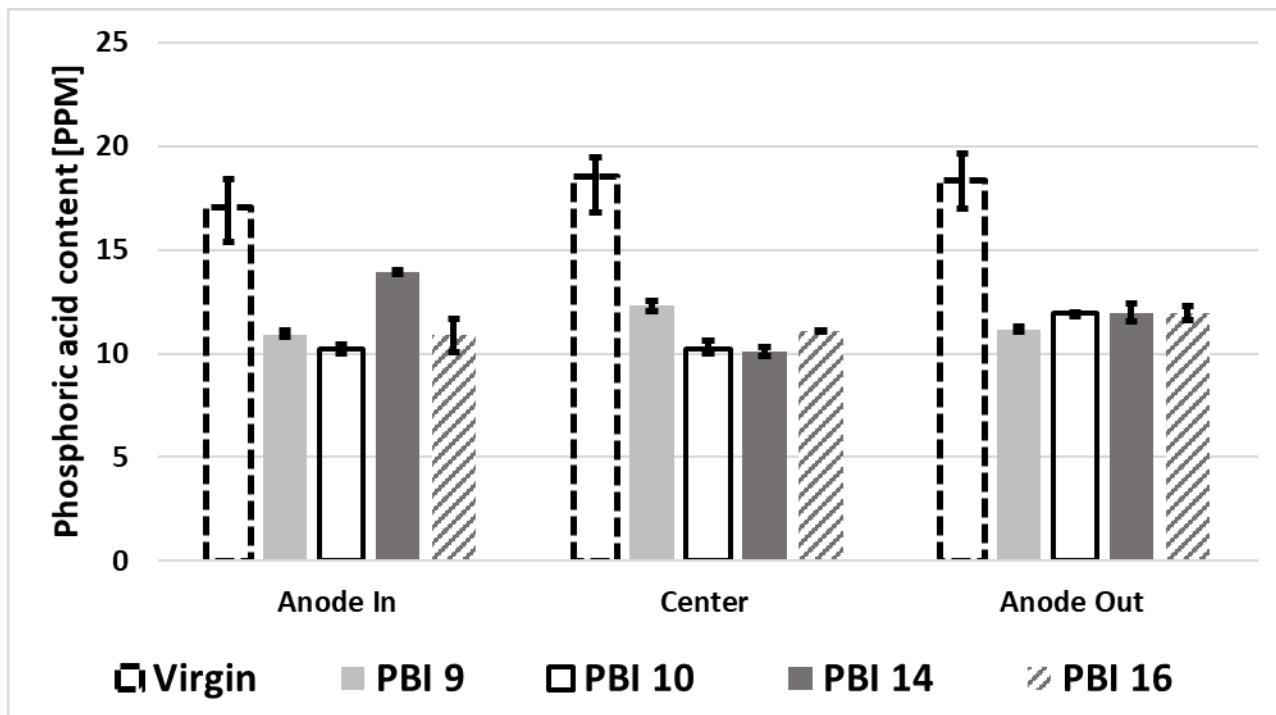


Figure 5.21: Phosphoric acid content of virgin MEAs vs PBI 9, 10, 14, and 16 at EOL

Using the same method as the phosphoric acid content measurements undertaken previously in Chapter 4, the acid contents of four MEAs from this chapter were calculated and compared against the same virgin MEA samples as the previous chapter. An ANOVA analysis of the presented data showed a statistically significant variation between the degraded and virgin sample sets. However, there was a significant variation between the degraded samples within and between the sample locations. The source of the variation was identified to be PBI 14 at the inlet and PBI 9 at the center. It is unknown why these MEAs and locations yielded outlying results. Each degraded sample shows a decrease in the extracted phosphorus acid when compared with the virgin sample set and is in close agreement with the previous findings in Chapter 4.

Returning to the work in Chapter 3, PBI 16 which was operated at 160°C and 0.2 A/cm² for 1588 hours was included in the ex-situ, post-test measurements. The original intention of this MEA was to confirm that the accelerated degradation seen in this work was due to our chosen operating parameters and not the testing setup. This was done by running at widely studied and previously reported conditions (160°C and 0.2 A/cm²) and confirming the results lined up with the published results in literature. The results from the phosphorus content measurement of this MEA are interesting as it has a comparable phosphorus content to the other MEAs while having been run for far longer. Considering the total voltage performance loss over testing period and not just the length of testing maintains the difference between PBI 16 and the other PBIs tested. With these established differences between the PBI 16 and the shorter 200-hour tests, the loss of acid is believed to stem not from the effects of elapsed operation time, temperature or pressure, but rather from beginning of life compression during cell assembly.

Membrane mass change

Figure 5.22 compares the mass loss between beginning and end of testing, determined via two different methods. The direct measurement method is represented in Figure 5.22 with the black column, and was determined by weighing the MEA prior to and after testing, using a laboratory scale. The open columns represent the mass loss calculated using the values of phosphoric acid loss derived from Figure 5.21. The methodologies used here are explained further in the Methods section of Chapter 4.

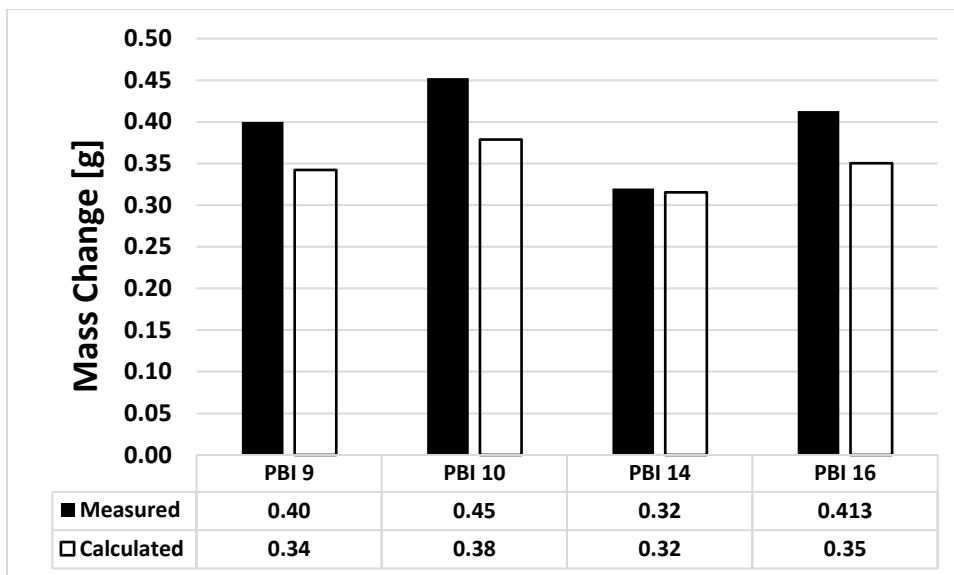


Figure 5.22: MEA mass loss between beginning and end of testing for PBI 9, 10, 14 and 16

From the results for PBI 9, 10, and 16, the mass change measured by the scale is consistent at 0.4 to 0.45 grams while the calculated mass loss from the acid content measurements for all MEAs averages around 0.35 grams. Unlike the other three MEAs, PBI 14 does not have a lower value for the calculated mass measurement. It was assumed that the measured mass change would be greater than the calculated mass change due to the acid remaining in the sample after the extraction process. The outlying measurement for PBI 14 may be associated with uncertainty in the direct MEA weighing method.

Membrane thickness change

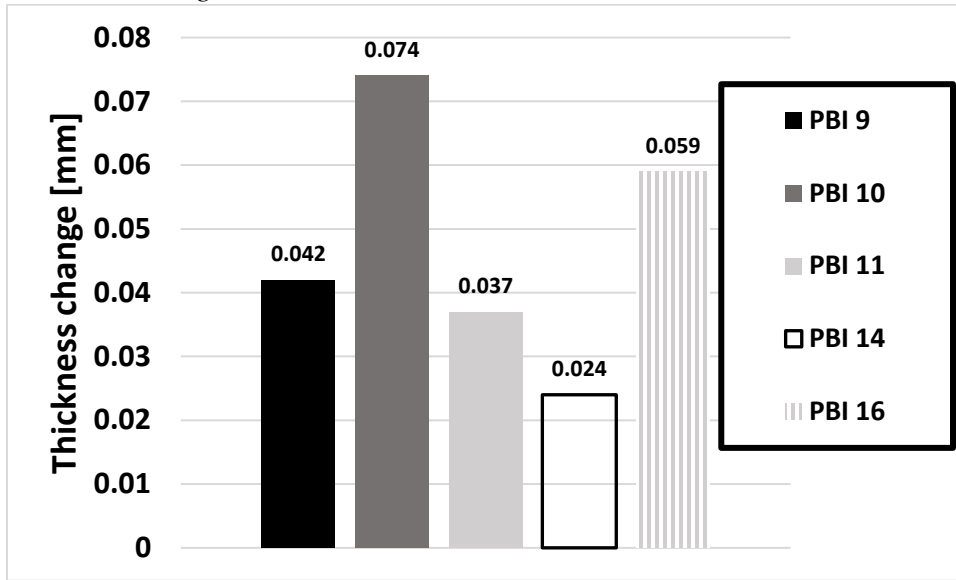


Figure 5.23: Thickness change over testing period of PBI 9,10,11,14, and 16

The thicknesses of the MEAs were also measured prior to and after testing (Figure 5.23). Due to the physical structure of the MEAs with easily compressible gas diffusion layers it was difficult to obtain accurate thickness results. A drop gauge with a set resistance was used in the measurements to accurately measure the thickness. However, from the variation in the data between the tests, it cannot be said that these data are very accurate and therefore not a lot of weight was placed on the findings of this measurement.

Oxygen-to-Phosphorus Ratio

Measurement

Table 5.3: Molar oxygen-to-phosphorus (O/P) ratio measurements

MEA tested	Anode Out	Center	Anode In
Virgin	4.1	4.7	3.9
PBI 4	2.5	3.2	2.8
PBI 5	2.9	3.6	3.1
PBI 6	3.0	3.6	3.8
PBI 9	3.4	3.6	3.4
PBI 10	3.1	3.5	3.6
PBI 11	1.8	2.9	2.9
PBI 14	3.7	3.9	3.9
PBI 16	4.7	4.9	4.8

The molar oxygen-to-phosphorus ratio (O/P) measurements in Table 5.3 give an indication of the hydration level of the acid within the membrane of the fuel cell MEA. Here the ratio of oxygen to phosphorus for the MEAs in this chapter is compared against the same set of virgin MEAs reported in previous chapters. The results in Table 5.3 show an increase in this ratio for PBI 9, 10, and 11 over the baseline established in the previous chapter, indicating a higher level of phosphoric acid hydration at EOL was achieved by operating at 200 kPa. PBI 14 built on the success of these runs

and was operated at 300 kPa which resulted in an even higher O/P ratio. Across all degraded MEA measurements, the anode outlet (which corresponds to the cathode inlet) had the lowest ratio of oxygen-to-phosphorus. This was expected, as the cell was oriented in counter-flow and thus the anode outlet aligns with the cathode inlet. The cathode inlet carries a great volume of relatively dry hot gas into the cell and was expected to be the site with the greatest dehydration of phosphoric acid in the MEAs.

The O/P ratio for the experiments isolating the effect of pressure (PBI 9, 10 and 14) show an increase over the ratio reported in the baseline testing (Chapter 4). Even among the pressurized experiments PBI 14 which operated at the highest pressure of 300 kPa had the highest O/P ratio. Nonetheless, even in PBI 14 some dehydration against the virgin material was observed. This may be due to the vapor pressure of the electrolyte at 200°C being above 300 kPa or the actual temperature of the cell being higher than 200°C. The cell temperature has been shown in other setups to exceed the setpoint of the temperature, particularly at the catalyst layer where the reaction is taking place.

PBI 16, first introduced in Chapter 3, was operated at 160°C, 0.2 A/cm² for 1588 hours. In the O/P ratio testing, PBI 16 demonstrated a ratio higher than that of the virgin MEA. Initially, this was believed to be a mistake, based on measurements conducted early in the research campaign to develop the oxygen to phosphorus ratio (Chapter 2), it was shown that pure orthophosphoric acid doped membrane samples prepared in-house also had ratios above that of the virgin MEA. This was to be expected based on the 85% aqueous solution of the acid with the calculated molar ratio of oxygen-to-phosphorous to be about 5.

Break-in

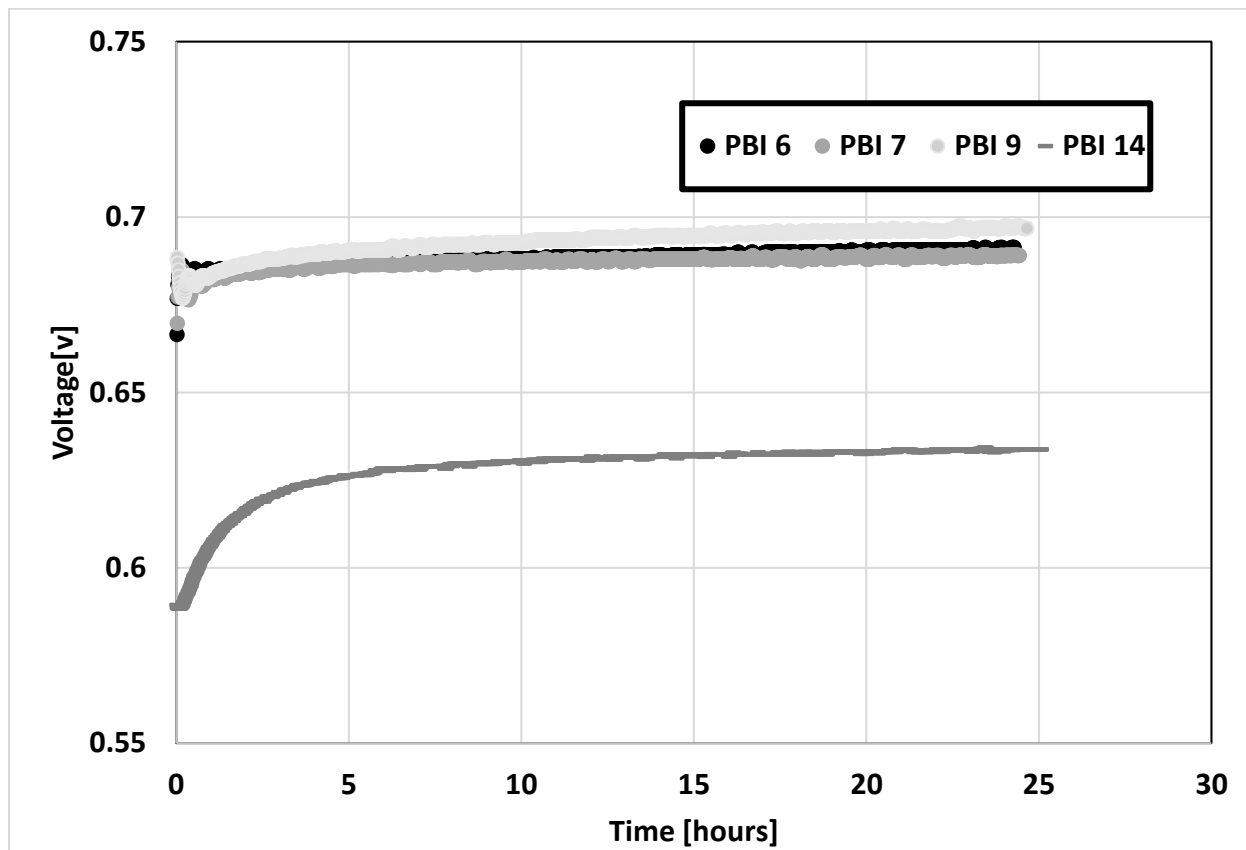


Figure 5.24: Break in voltage curves for PBI 6,7,9, and 14

The increase in voltages seen in Figure 5.24 for PBI 6, 7, 9 and 14 is typical for our MEAs during the break-in period. As described in the Introduction section (Chapter 1), our break-in periods of 24 hours at 160°C and 0.2 A/cm² result in an increase in MEA performance prior to the start of any durability or performance testing. In Figure 5.24 the difference in voltage between PBI 14 and the other MEAs is believed to be a product of manufacturing deviation or variability in the cell assembly process. It has been speculated that the improvement in performance observed during the break in process is due to rehydration and redistribution of acid within the cell. This is validated by the work in Chapter 2 on the rehydration of recently hot-pressed MEAs. This work

showed that the hot-pressing procedure could dehydrate the MEA, which was observed through the SEM oxygen-to-phosphorus ratio measurements. It was shown that rehydration was possible and resulted in an increase in the oxygen-to-phosphorus ratio. The evidence in this chapter points toward PBI 16 having undergone an initial rehydration during the break in period and experiencing minimal dehydration during the entire 1588-hour runtime.

Conclusions and Future work

The primary objective of the experiments reported in this chapter was to develop methods to reduce the degradation of MEAs at 200°C and 0.4A/cm². This was accomplished through the rehydration of the electrolyte with the addition of water, or by the increase of operational pressure to be closer to the vapor pressure of the ortho-phosphoric acid. While the degradation rate was reduced in magnitude and improvements were shown to be made with increasing pressure, the degradation rate was not reduced to the levels observed at more benign operating conditions with lower temperature and/or current density. It is understood now that this is most likely due to the slight dehydration of the acid in the membrane occurring at the triple phase boundary, where the reaction is the hottest, and could have impacts beyond what the net dehydration of the membrane indicates. In the future, to prove this point a pressure higher than 300 kPa should be tested to overcome the concerns about the vapor pressure of the phosphoric acid. An O/P ratio of around 5, as seen in the methods of Chapter 2, and the measurements of PBI 16 prove that little dehydration is occurring. This point was never reached at 200°C. To confirm the validity of the hypothesis of cell rehydration during the break in procedure and the initial loss of acid due to compression during cell assembly, an MEA should be run through the break-in procedure with measurement of acid

content and O/P ratio. The results from this Chapter showed no improvement in cell durability with enhanced hydration, although hydration was conclusively shown to improve voltage performance of the cell.

Citations Chapter 5

[1] Waller, Michael G., Mark R. Walluk and Thomas A. Trabold, 'Performance of High Temperature PEM Fuel Cell Materials. Part 1: Effects of Temperature, Pressure and Anode Dilution' (2016) 41 *International journal of hydrogen energy* 2944

[2] Larminie, James, Andrew Dicks, and Maurice S. McDonald. *Fuel cell systems explained*. Vol. 2. Chichester, UK: J. Wiley, 2003.

Chapter 6 - Comparative Analysis of HT-PEM Performance Versus Results of Prior Studies

For many of the fuel cell experiments described in Chapters 3, 4 and 5, a series of polarization curves were measured at beginning-of-life to establish a baseline of performance. These measurements were conducted after the break-in period (160°C @ 0.2 A/cm² for 24 hours) and covered a range of temperatures and pressures depending on the objective of the specific MEA experiment, as well as the capabilities of the testing stand used. Because of the wide ranges of conditions tested using nominally equivalent PBI-based MEA materials, it was instructive to compare the present results to prior reported data for HT-PEM systems because to the best of our knowledge no such comparative analysis has been reported previously.

Several criteria were established for selecting data included within the comparative dataset. First, the MEAs needed to be commercially purchased. This was important to ensure reasonable quality control of materials tested across different studies and due to inherent variability with in-house developed material, as observed in our in-house fabrication of MEAs reported in Chapter 2. Secondly, we only included polarization data obtained at one of the three specific temperatures (160, 180 and 200°C) and at atmospheric pressure. The operating temperature and pressure were necessary criteria due to the obvious effects of temperature and pressure on cell performance. The third requirement was that the cell needed to be operated on pure hydrogen and air. There exists a wealth of data on the effect of CO and other impurities on cell performance, however, the inclusion of impurities in the fuel has well-known negative impact on cell performance, and therefore data from these studies cannot readily be compared to pure H₂-air systems. The fourth requirement was that polarization data were acquired prior to any operation which could have

compromised the performance of the cell, such as an accelerated stress or a startup/shut-down testing.

A computer-aided design (CAD) software method was used to extract data from previously published papers. Figures from published manuscripts were processed in the Autodesk inventor professional package to determine the numerical values of different data points of interest. Tables of the raw data extracted using this method are provided in the Appendix and all studies included in the analysis are listed in Table 6.1.

Table 6.1: Studies utilizing Commercial MEAs sourced in this chapter

Reference	MEA Type	Area [cm ²]	Temperature [°C]	Stoich Ratio [H ₂ /Air]	Notes
Present study	Advent PBI	45.2	160,180,200	1.5/2	
Cicconardi et al. (2011)	Commercial	45	160,180	1.2/2	Back pressure set to 1.2 bar
Pilinski et al. (2015)	Celtec®-P1100W	20.25	160	1.5/2	Tested load cycling and acid uptake into flow fields.
Schonvogel et al. (2015)	Celtec®-P1100W	20.25	160	1.5/2	Beginning of life data from several different AST
Tseng et al. (2016)	Advent TPS®	25	180	1.2/3	Also did studies with a metal foam flow field; these data not included
Waller et al. (2016)	Advent PBI	45.2	160,180,200	1.5/2	
Büselmann et al. (2017)	Commercial	25	160	1.5/2	The difference in MEA (S vs. L) was tested after characterization, but did not impact BOL POL.
Zhou et al. (2019)	Dapozol G77	46.5	160,180	2/4	Assessed the effect of humidity
Yang (2019)	Advent PBI	45.2	200	1.5/2	
Advent (2020)	Advent PBI		160	1.2/2	

Results of the comparative analysis are presented in Figures 6.1, 6.2 and 6.3, corresponding to cell temperature of 160, 180 and 200°C, respectively. Each figure follows the same format with the first two sub-figures (A and B) showing the full data sets, with the average of the present data indicated by solid circles and connecting lines. The third and fourth sub-figures (C and D) show the data from this study, with the solid symbols representing the average and the error bars indicating the minimum and maximum values for all MEAs included in that dataset.

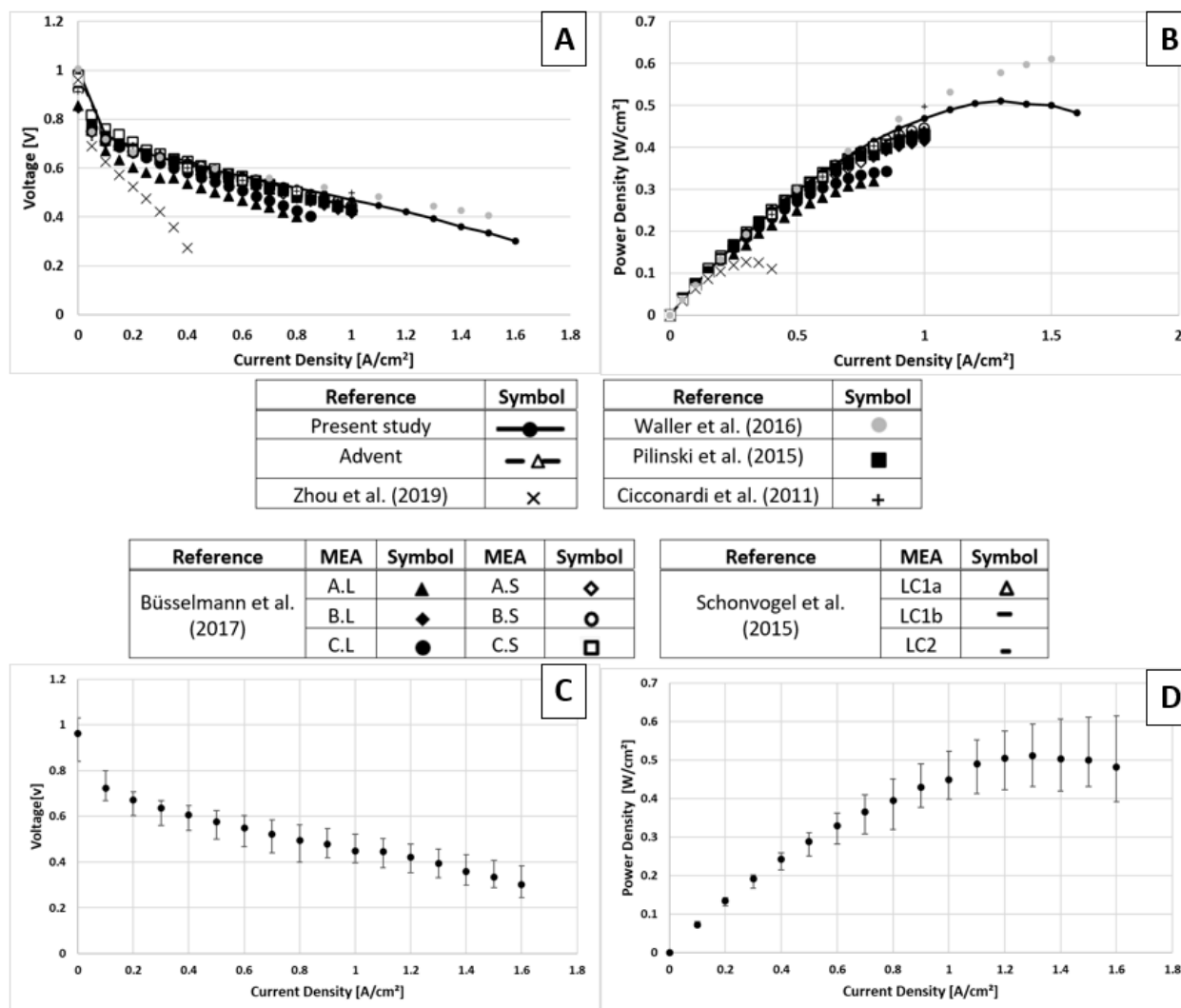


Figure 6.1: Comparative voltage and power data for commercially available MEAs operated on H_2 and air at $160^\circ C$

(A) Full polarization dataset (B) Full power data set (C) Average polarization data from present study, with errors bars indicating min/max (D) Average power data from present study, with errors bars indicating min/max

From Figure 6.1(A), the majority of the data sourced from literature can be seen to cover current densities only up to $1.0 A/cm^2$. In the context of Figure 6.1(B) this becomes relevant as the maximum power point in most studies exceeds the value measured at $1.0 A/cm^2$. In the case of $160^\circ C$, the maximum power point can be seen from the average in Figure 6.1(D) to be $0.51 W/cm^2$ at $1.3 A/cm^2$, with the error bars representing the maximum and minimum values obtained from

all nominally equivalent MEAs tested under the same conditions. In Figure 6.1(C), the variability in the data is shown to be consistent and generally independent of current density. The error is multiplied when presented as power density, leading to an increasing min-to-max range with increasing current density in Figure 6.1(D). It is unknown why exactly the voltage data for Zhou et al. was significantly lower than the other datasets; it may stem from the cell assembly, MEA fabrication, or testing setup.

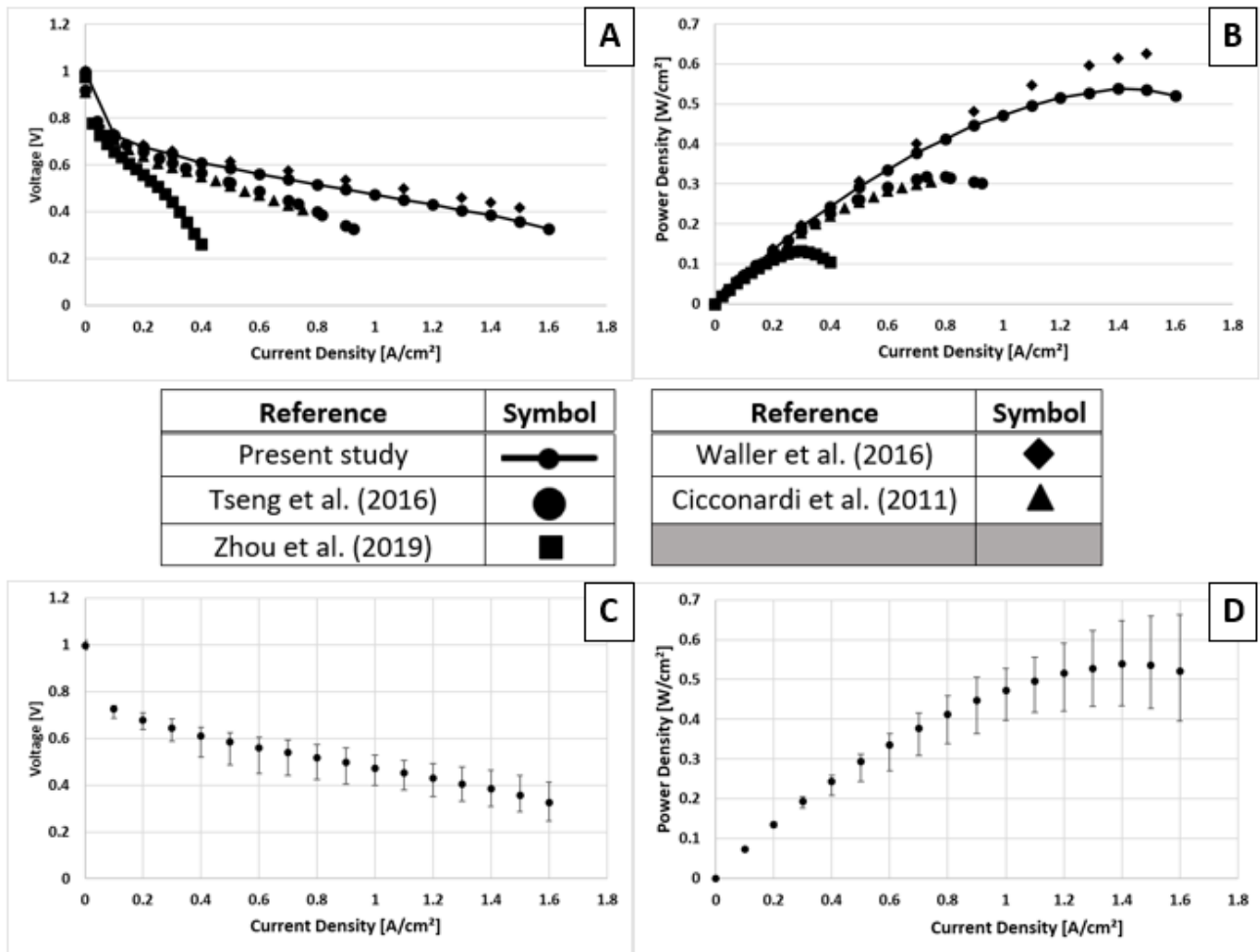


Figure 6.2: Comparative voltage and power data for commercially available MEAs operated on H_2 and air at $180^\circ C$

(A) Full polarization dataset (B) Full power data set (C) Average polarization data from present study, with errors bars indicating min/max (D) Average power data from present study, with errors bars indicating min/max

At $180^\circ C$, the maximum power point for the MEA shifts farther out to $1.4 A/cm^2$ with a power density of $0.54 W/cm^2$. At $180^\circ C$ there are far fewer data points from literature to compare against than at $160^\circ C$.

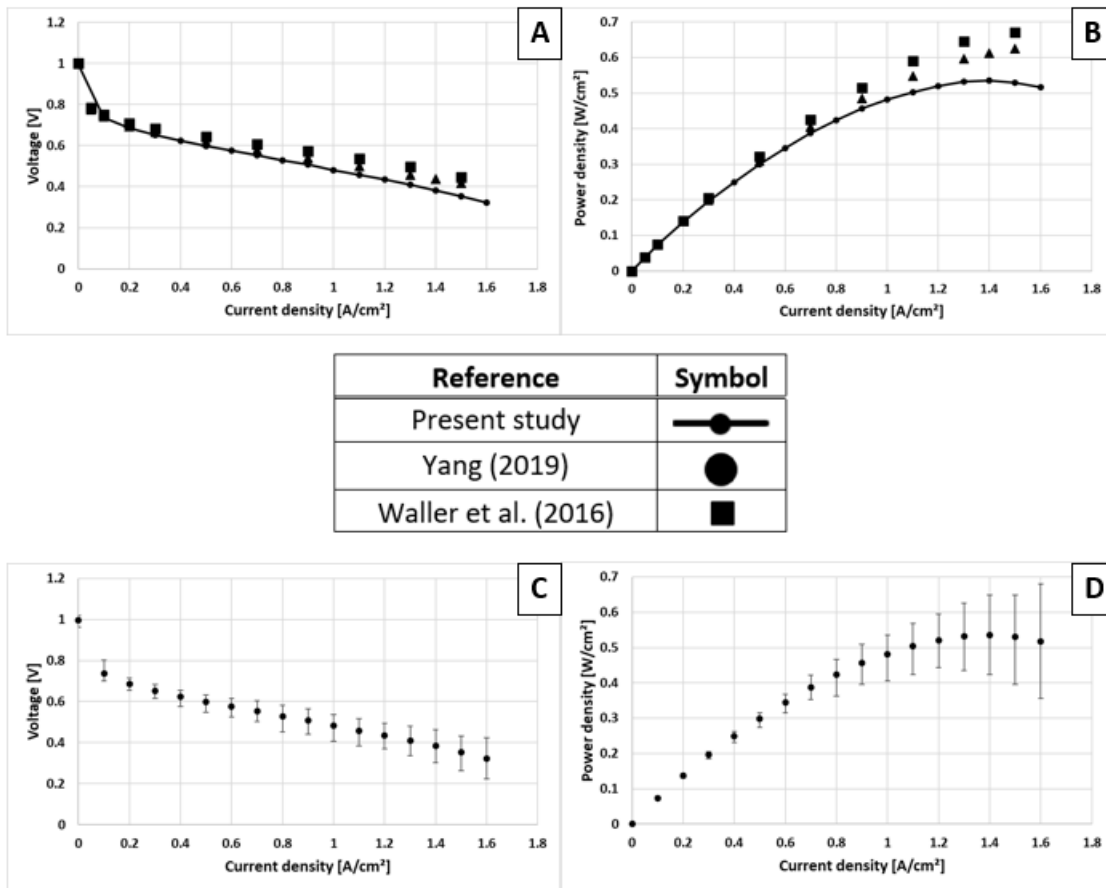


Figure 6.3: Comparative voltage and power data for commercially available MEAs operated on H₂ and air at 200°C

(A) Full polarization dataset (B) Full power data set (C) Average polarization data from present study, with errors bars indicating min/max (D) Average power data from present study, with errors bars indicating min/max

Similar to 180°C, the maximum power point seen at 200°C was 0.54 W/cm² at 1.4 A/cm² with even fewer studies in literature to include at this temperature. The work of both Yang (2019) and Waller et al. (2016) exceed the performance of the average of the MEAs included in this study. However, these earlier results from our research group are still covered within the spread of the data shown with the error bars in Figures 6.3(C)- and (D).

Application of TPS Type MEAs

Some limited fuel cell testing was also conducted with TPS type MEAs supplied by Advent Technologies in 45.2 cm² size. TPS MEAs were selected for testing because we thought they would have a lower degradation rate, as promoted by Advent and reported in several prior literature studies. Based on the claims from Advent and positive results from at least some of the published research, we believed that TPS MEAs would have a lower beginning-of-life voltage over the current density range of interest, however, the system would benefit from less voltage degradation over time. Essentially, we would be sacrificing initial performance for a more stable, longer lasting system. This could have many benefits in reducing the cost of maintenance and repair of HT-PEM systems. The TPS system is marketed for operation at 180-200°C whereas the PBI based system for 160°C. All the testing on the TPS MEAs was performed on the Stand 1 testing setup and were treated the same as the PBI MEAs in break-in and build procedure. Three TPS MEAs were tested in 200 hours durability tests within beginning- and end-of- life polarization curves taken to establish change in performance over time.

TPS 1

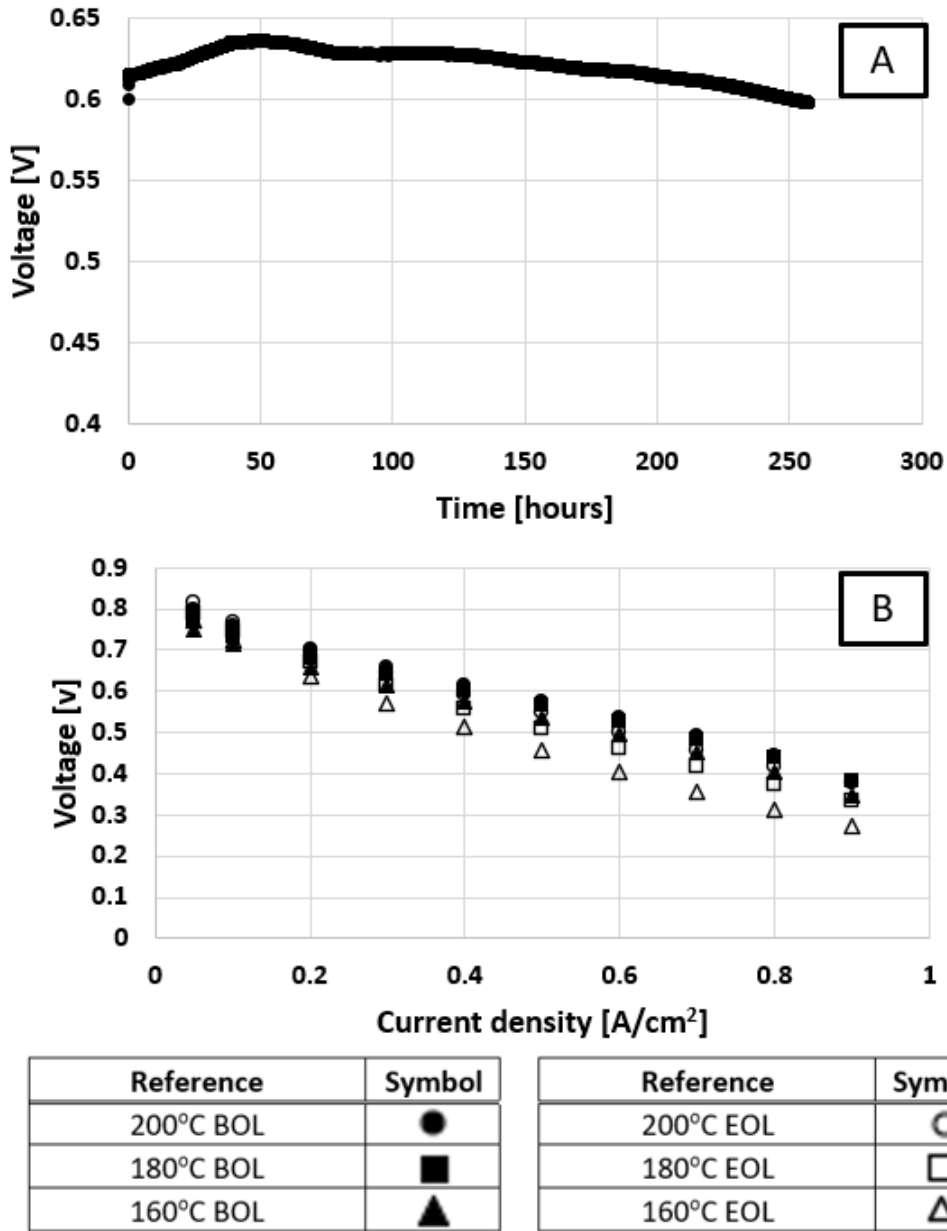


Figure 6.4: (A) Voltage degradation profile of TPS 1 at 0.4 A/cm², 200°C, and atmospheric pressure with H₂/air stoichiometric ratios = 1.5/2 (B) Polarization curves of TPS 1 at 160, 180, and 200°C and atmospheric pressure with H₂/air stoichiometric ratios = 1.5/2 for BOL and EOL

The voltage degradation profile for TPS1 can be seen in Figure 6.4(A) with the polarization data for beginning- and end-of- life at 160, 180 and 200°C in Figure 6.4(B). The voltage degradation profile shows a similar pattern to that of the PBI MEAs with the voltage peaking then following a

relatively linear degradation profile for the remainder of the testing. However, the peak in voltage can be seen at roughly 50 hours in Figure 6.4(A), a much longer time to peak than observed for any of the PBI MEAs. TPS 1 had a degradation rate of $292.7 \mu\text{V/h}$, far greater than the rate for the PBI testing reported in previous chapters.

TPS 2

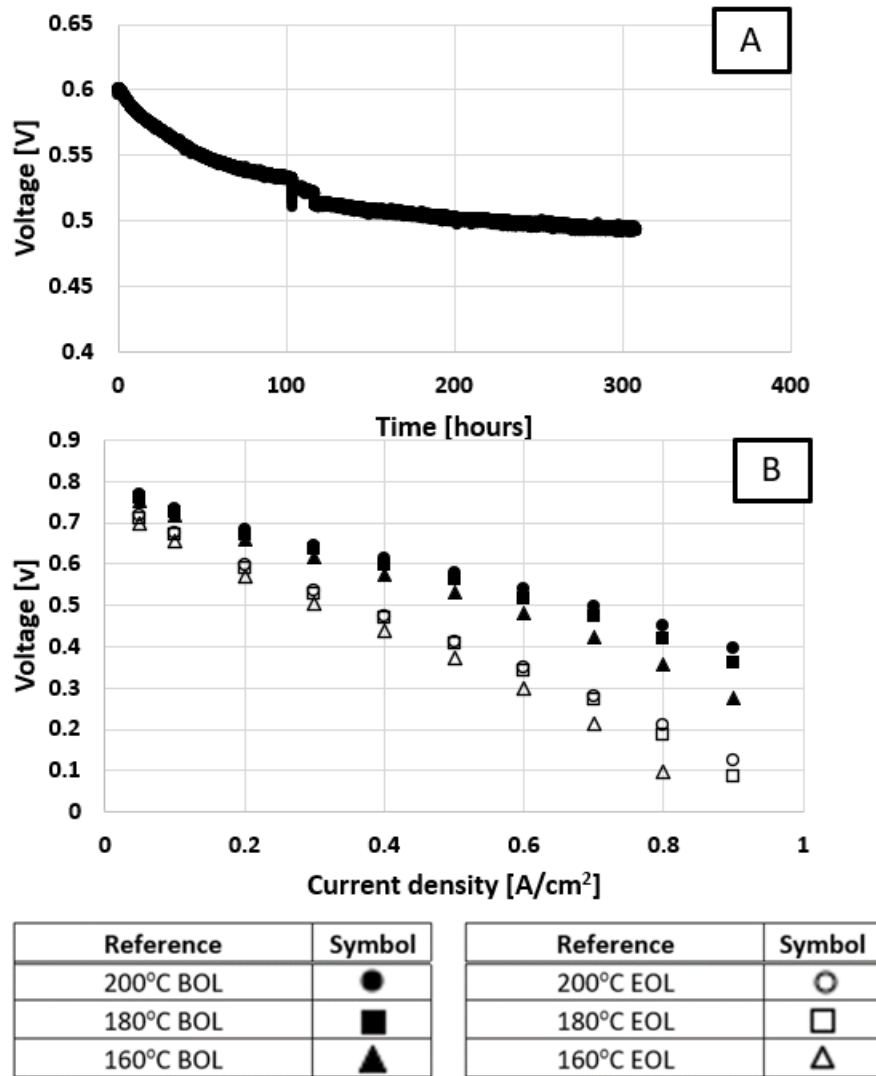


Figure 6.5: (A) voltage degradation profiles of TPS 2 at 0.4 A/cm^2 , 200°C , and atmospheric pressure with H_2/air stoichiometric ratios = $1.5/2$ (B) Polarization curves of TPS 2 at 160, 180, and 200°C at atmospheric pressure with H_2/air stoichiometric ratios = $1.5/2$ for both beginning of life (BOL) and end of life (EOL)

Figure 6.5 presents the results of experiments with TPS 2 with the voltage degradation profile in Figure 6.5(A) and the beginning- versus end-of-life polarization data in Figure 6.5(B). Compared to the majority of the PBI MEAs tested and the results from TPS 1 in Figure 6.4, this MEA displayed a different voltage profile with the peak occurring at the beginning-of-life. It is unknown what happened at roughly 100 hours to cause the voltage fluctuation, but it is assumed to be a slight issue with the test stand. Noting the scale on the y-axis, the magnitude of the fluctuation is relatively small, on the order of 30 mV. A degradation rate of 580.4 $\mu\text{V}/\text{h}$ was calculated for this MEA, which is far greater than the rate observed in both the previous PBI MEAs and TPS 1.

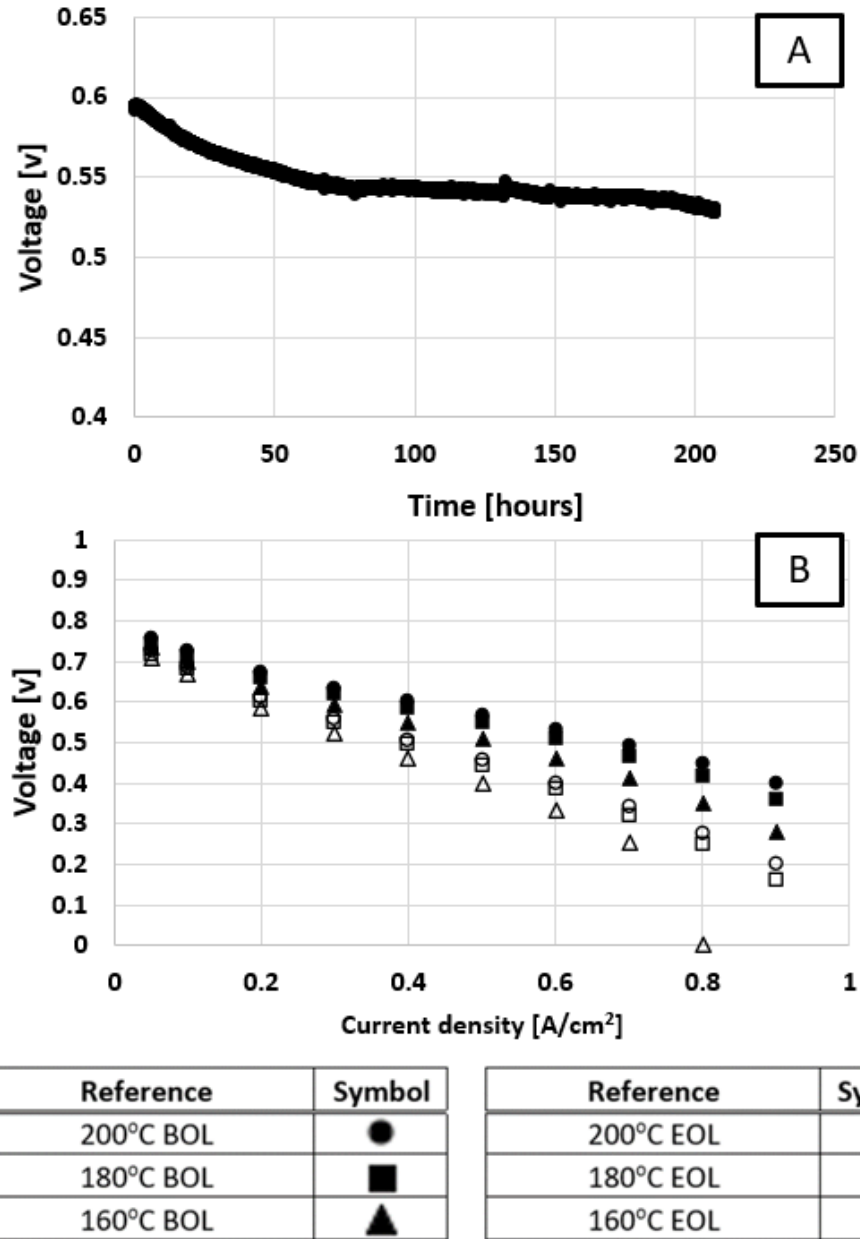


Figure 6.6: (A) voltage degradation profiles of TPS 3 at 0.4 A/cm², 200°C, and atmospheric pressure with H₂/air stoichiometric ratios = 1.5/2 (B) Polarization curves of TPS 3 at 160,180, and 200°C at atmospheric pressure with H₂/air stoichiometric ratios = 1.5/2 for both beginning of life (BOL) and end of life (EOL)

The results for TPS 3 experiments run at 200°C are shown in Figure 6.6. The voltage data in Figure 6.6(A) follow a similar profile to that of TPS 2 and not TPS 1, with the beginning of life

voltage being the highest. Also, similar to TPS 2, the voltage degradation rate computed for TPS 3 was 542.5 $\mu\text{V}/\text{h}$. As observed for both TPS 2 and 3, the profiles appear to deviate significantly from linearity and instead display two distinct regions with a change in slope occurring between elapsed times of 75 and 125 hours. Compared to previously tested PBI-based cells and TPS 1, there is an initial accelerated degradation and secondary normalizing and leveling of the voltage. With the overall trend no longer linear it may not be appropriate to take the degradation rate over the entirety of the testing period. Revising the measurement to just the linear region after the change in slope gives an approximate voltage degradation rate of over 200 $\mu\text{V}/\text{h}$ for both TPS 2 and 3, depending on where the selected region of the slope.

Presentation of Normalized Data

Normalizing the data for comparison of the three different TPS runs, shows the inconsistency in the data and also highlights the severity of the degradation for TPS2 and 3. It is unknown what caused the accelerated degradation of these systems when the expectation based on claims and prior studies was that they would experience a reduced degradation rate.

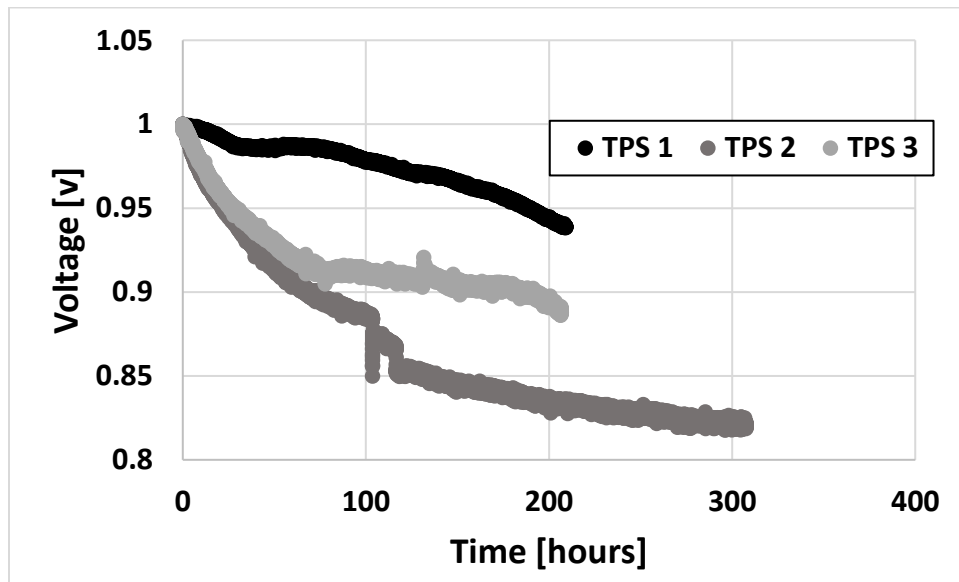


Figure 6.7: Normalized voltage degradation profiles of TPS 1, 2, and 3 at 0.4 A/cm², 200°C with H₂/air stoichiometric ratios = 1.5/2

It may be that the system does not function well at 200°C as it is designed for operation at 180°C, or it may be due to a shelf life limitation. This batch of MEAs was left over from a larger batch of MEAs obtained during previous testing. They have been sitting in the original packaging in a climate-controlled room for about 10 years. Based on direct communication with Advent Technologies, they concurred the unexpectedly poor performance was most likely a shelf-life issue, however they have had some customers using MEAs of about the same age.

Conclusions

The results presented in this chapter established both performance and repeatability data for a range of temperature conditions for HT-PEM. The current work compares the tests run in this study with those of other commercial MEAs. The findings demonstrate that the maximum power point is greater than indicated in many previous studies, and the significant increase in data points thoroughly establishes a baseline of operational performance. Given the use of commercially available MEAs, assembled under stringent laboratory conditions, the work in this study established the performance range which can be expected from these cells due to manufacturing and assembly variations. This can be highly useful for the future modeling of fuel cells by defining the latitude of cell performance. The durability of TPS type MEAs was also tested and found to perform poorly relative to PBI-based materials, likely due to the age of the MEAs.

Citations Chapter 6

Waller, Michael G., *Development of an Integrated Reformer and Fuel Cell System for Portable Power Applications* (ProQuest Dissertations Publishing, 2016).

Yue, Yang, *Performance and Durability of High-Temperature Proton Exchange Membrane Fuel Cells Operated on Propane Reformate* (Rochester Institute of Technology, 2019).

Tseng, Chung-Jen, Ying-Jui Heush, Chien-Jui Chiang, Yi-Hsuan Lee, and Kan-Rong Lee. "Application of metal foams to high temperature PEM fuel cells." *International journal of hydrogen energy* 41, no. 36 (2016): 16196-16204.

Cicconardi, S., R. Cozzolino, A. Perna, and M. Minutillo. "Sensitivity Analysis on Commercial PBI-Based MEAs for HT-PEMFC." *EFC2011* (2011): 1-2.

Zhou, F., D. Singdeo, and S. Knudsen Kær. "Investigation of the Effect of Humidity Level of H₂ on Cell Performance of a HT-PEM Fuel Cell." *Fuel Cells* 19, no. 1 (2019): 2-9.

Pilinski, Nadine, Maren Rastedt, and Peter Wagner. "Investigation of phosphoric acid distribution in PBI based HT-PEM fuel cells." *ECS Transactions* 69, no. 17 (2015): 323.

Büselmann, J., M. Rastedt, V. Tullius, K. Yezerska, A. Dyck, and P. Wagner. "Evaluation of HT-PEM MEAs: Load cycling versus start/stop cycling." *International Journal of Hydrogen Energy* 44, no. 35 (2019): 19384-19394.

Schonvogel, D., M. Rastedt, P. Wagner, M. Wark, and A. Dyck. "Impact of accelerated stress tests on high temperature PEMFC degradation." *Fuel Cells* 16, no. 4 (2016): 480-489.

Zhou, F., D. Singdeo, and S. Knudsen Kær. "Investigation of the Effect of Humidity Level of H₂ on Cell Performance of a HT-PEM Fuel Cell." *Fuel Cells* 19, no. 1 (2019): 2-9.

Cicconardi, S., R. Cozzolino, A. Perna, and M. Minutillo. "Sensitivity Analysis on Commercial PBI-Based MEAs for HT-PEMFC." *EFC2011* (2011): 1-2.

Advent Technologies. (2022, October 4). Retrieved November 16, 2022, from <https://www.advent.energy/>

Chapter 7 - Techno-Economic Analysis of SOFC vs. HT-PEM for use with Reformate Fuel Derived from Co-pyrolysis

Introduction

Currently one of the greatest obstacles to the widespread deployment of fuel cells is the lack of an inexpensive, distributed supply of hydrogen [1]. One potential answer to this issue is the use of reformat fuels derived mostly or entirely from renewable resources. Pyrolysis of biomass offers an appealing supply of renewable energy. Co-pyrolysis of waste plastic and biomass allows the conversion of a waste stream into a usable reformat fuel, while also providing an economically viable pathway to handle difficult-to-manage waste materials such as agricultural mulch film [2,3]. In this study, a co-pyrolysis unit was modeled as an integrated system with either a solid oxide fuel cell (SOFC) or high-temperature proton exchange membrane (HT-PEM) fuel cell and analyzed based on cost. This is accomplished by normalizing the power outputs of the two systems to 1 kW and calculating the cost of both configurations. This work drew heavily from the earlier research of James (2012) on the cost comparison of low-temperature proton exchange membrane (LT-PEM) fuel cell, HT-PEM fuel cell, and SOFC run on natural gas [4]. James investigated the effect of power production and manufacturing quantity on the cost per unit of these different fuel cell systems. He found that for all but the lowest production quantity (< 100 units/year), and lower power output (1 kW), SOFC was the best option in terms of total cost of ownership. However, in the 100 unit/year and 1kW case, HT-PEM was the superior choice. In the current study it was anticipated that SOFC not HT-PEM would be the less expensive option, due to the composition of the pyrolysis gas with higher H₂ concentration that may enable internal reforming within the SOFC stack. However, it was considered important to extend the earlier results of James (2012) by using

the most recent cost data available for SOFC and HT-PEM stacks, materials and balance-of-plant components, in the context of renewable hydrogen fuels derived from biomass.

Methods and Results

An overall system diagram is provided in Figure 7.1. Here the process begins on the far left in the blue shaded region with the pyrolysis operation. As this is simulating a co-pyrolysis process, there are biomass and plastic inputs as well as operational parameters related to the biomass-to-hydrogen syngas conversion process. Depending on the material makeup of the inputs, as well as the condition under which the pyrolysis reaction is managed, the composition of the product gas can be changed. This gas composition can then be fed directly into an SOFC or alternatively directed through a reforming stage and then into an HT-PEM Fuel cell. The model was sized for a 1 kW power output with the cell active areas determined based on assumed voltage/current performance and gas flow rates dependent on assumed anode and cathode stoichiometric ratios. With both the HT-PEM and SOFC systems designed to satisfy the 1 kW power requirement, the cost of both systems was then calculated. It is important to note that the costs used in this analysis do not take the life cycle costs into account, only capital cost of the system is calculated.

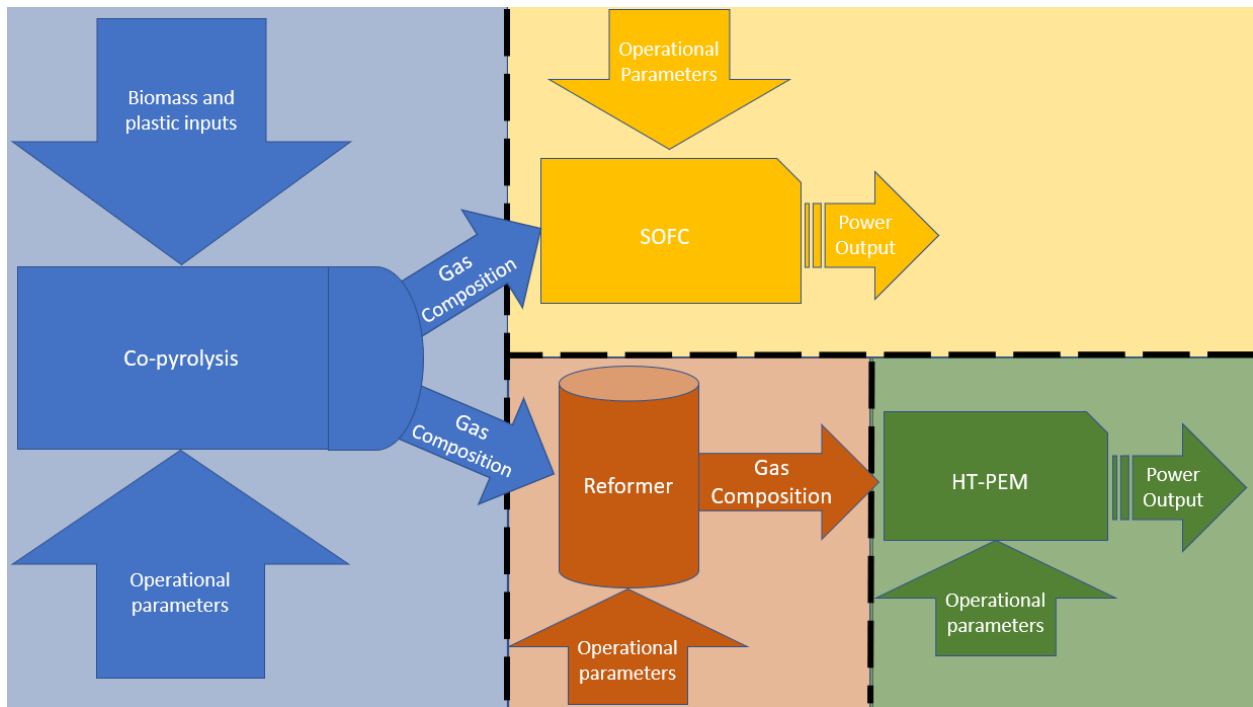


Figure 7.1: System Diagram

Co-pyrolysis system

To determine the concentrations of the gases produced through the pyrolysis process, Table 7.1 was based on co-pyrolysis processes reported in the literature, including the inputs and outputs of the system. It was found that the work of Serio et al (2008) “Pyrolysis of Mixed Solid Food, Paper, and Packaging Wastes” best reflected the planned co-pyrolysis supply of this study for intended use with agricultural biomass residues and waste low-density polyethylene (LDPE) mulch film.

Table 7.1: Summary of prior biomass-plastic co-pyrolysis studies (PLA-Polylactic acid, PE-Polyethylene, PP-Polypropylene, PS-Polystyrene, PHB- Polyhydroxybutyrate, LDPE-Low density polyethylene, HDPE- High density polyethylene)

Year	Title	Process	Biomass	Biomass % Range	Plastic	Plastic % Range	Temp First Stage [C]MAX	Temp Second Stage [C] MAX	CO [%]	H2 [%]
2007	Flash co-pyrolysis of biomass with polylactic acid. Part 1: Influence on bio-oil yield and heating value	Flash Co-pyrolysis	Willow	90.9%-50%	PLA	9.1-50%	450			
2008	Pyrolysis of mixed solid food, paper, and packaging wastes	hybrid pyrolysis/oxidation reactor	Lignin, Food Waste, Cellulose	Lignin-3%, Food 30-60%, Cellulose 33-50%	PE	4-17%	700	1050	14.7-24.8%	32-38.5%
2008	Flash co-pyrolysis of biomass with polyhydroxybutyrate: Part 1. Influence on bio-oil yield, water content, heating value and the production of chemicals	Flash Co-pyrolysis	Willow	50-87.5%	PHB	12.5-50%	450			
2009	Study of the co-pyrolysis of biomass and plastic waste	pyrolysis	Pine residue	0-100	PP,PS,PE	0-100%	350-450		CO and CO2 reported together	0.05

2009	Flash co-pyrolysis of biomass: The influence of biopolymers	Flash Co-pyrolysis	Willow	50-100%	PLA,Corn Starch, PHB,BIO Pearls,Easter, Solanyl, Potato starch	50%	450			
2009	Influence of zinc chloride addition on the chemical structure of bio-oil obtained during co-pyrolysis of wood/synthetic polymer blends		Pinewood Sawdust	50-75%	PP,PS	25-50%	120	450		
2010	Co-pyrolysis of pine cone with synthetic polymers	Co-pyrolysis	Pine cones and powdered cellulose	30-50%	LDPE,PP,PS	50-70%	500		only reported elemental makeup	
2012	An experimental study on bio-oil production from co-pyrolysis with potato skin and high-density polyethylene (HDPE)	Co-pyrolysis	potato chip waste	0-100%	HDPE	0-100%	470-520			

2013	Preparation of liquid chemical feedstocks by co-pyrolysis of electronic waste and biomass without formation of polybrominated dibenzo-p-dioxins	Co-pyrolysis	Fir Sawdust	0-100	local plastic recycling waste	0-100	450-600			
2014	Hydrogen production from biomass and plastic mixtures by pyrolysis-gasification	pyrolysis/gasification	Wood Sawdust	80-100	PP,HDPE,PS, RP PE	0-20	600	800	25-25%	32-69%
2014	Pyrolysis of mixtures of palm shell and polystyrene: An optional method to produce a high-grade of pyrolysis oil	Pyrolysis	palm shell	60-80%	PS	20-40%	500			
2014	A review on co-pyrolysis of biomass: An optional technique to obtain a high-grade pyrolysis oil	Co-pyrolysis								

To obtain the greatest power output for both the SOFC and the HT-PEM systems, the sample composition which produced the highest concentration of hydrogen, while maintaining material inputs similar to those desired for the feedstock in this study was selected (Table 7.2)

Table 7.2: Sample Composition 4B refers to the sample set in the sourced reference.

Sample composition	polyethylene	Lignin	Food	Cellulose
4B	4	3	60	33 (paper)

The setup for this run used a 2-chamber pyrolysis unit with the first unit heated to 700°C and the second cracking chamber heated to 1050°C. The unit was operated in dynamic mode ensuring a constant flow of gas. Samples were translated through the chambers at 0.76 cm/min. The output gas concentrations from the co-pyrolysis process described above are presented in Table 7.3 below.

Table 7.3: Composition of gas exiting the co-pyrolysis process

H ₂	CO ₂	CO	CH ₄	C ₂ H ₄
37.5	17.0	16.5	23.1	6.0

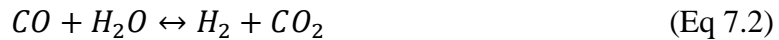
These gas concentrations were assumed to be scalable while maintaining this presented gas composition. The intention was to scale the pyrolysis unit to meet the fuel flow demand of the fuel cells without changing the output concentration of the gas.

SOFC system

The solid oxide fuel cell was assumed to not require any pre-reforming of the gas. This is due to the ability of the solid oxide fuel cell to self-reform fuels within the cell [17]. Operating a SOFC directly off biogas has been studied by Shiratori (2008) in research on “feasibility of direct-biogas SOFC” Shiratori found that a SOFC system could be operated directly off biogas and produce

stable performance over time [18]. He also investigated losses associated with fuel selection and found these to stem from contamination of hydrogen sulfide (H₂S), not the reforming of methane (CH₄). It is important to note that the biogas used in this prior study was comprised of 62.6% CH₄ and 35.7% CO₂. The gas composition sourced from pyrolysis proposed here includes much higher initial, and post reforming, concentrations of H₂ as well as lower initial concentrations of CH₄. This indicates that the system would be able to be directly fed from the pyrolysis gas supply without prior reforming and without suffering performance losses.

With the introduction of water to the system, methane (CH₄), carbon monoxide (CO) and ethylene (C₂H₄) are known to be reformed within a SOFC fuel cell according to the following reactions:



Equation 7.1 is the steam methane reforming reaction that dominates the reformation of methane within the cell [19]. The methane reforms with the added steam and forms carbon monoxide as well as hydrogen, which can further feed the fuel cell electrochemical reaction. The addition of the carbon monoxide concentration from the steam reforming of methane in turn enters a water gas shift reaction (Equation 7.2), and forms CO₂ with more H₂ [20]. The interaction of ethylene within SOFC reforming is, however, less well understood. It has been shown that ethylene can undergo steam reforming under similar conditions to that of methane, (Equation 7.3) [21]. It is understood that the nickel catalyst used in this reaction is stable in the reforming of biogas, and it has been shown that ethylene is not a contaminant of concern for the proper function of an SOFC cell [22]. The contamination concern is greatest with nickel, as the effect of most major fuel

impurities is seen through an impact on the catalyst. The reformation of ethylene produces further hydrogen and carbon monoxide with the CO undergoing a water gas shift reaction[23].

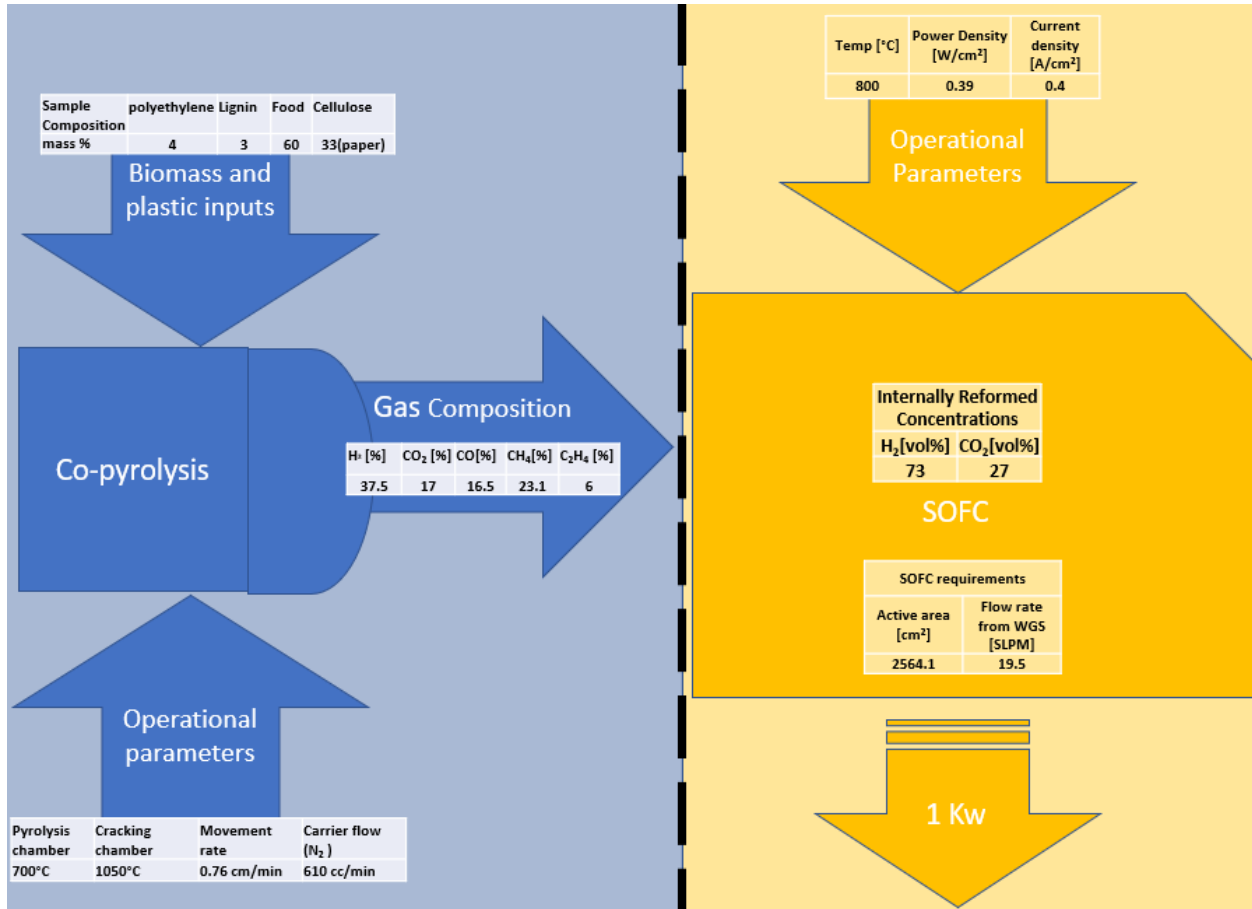


Figure 7.2: Sub-model of co-pyrolysis and SOFC system

Figure 7.2 shows the sub-model of the SOFC co-pyrolysis system. In blue are the values sourced from the work of Serio et al. (2008) and on right in yellow is a compilation of information on the performance of the fuel cell based on the pyrolysis inputs required to achieve the desired 1 kW power output.

The cell size was determined from the power density of SOFC running on reformat fuel and the requisite power requirement of the system [24]. From the cell size, current density and gas concentration defined above, reactant flow rates were calculated assuming hydrogen/air stoichiometric ratios of 1.2/1.5.

HT-PEM system

A HT-PEM cell does not have the benefit of internal reforming as does SOFC. In the case of HT-PEM, the steam reformation and water gas shift processes occurring internally within the SOFC system, need to be mechanized as sub-systems outside the HT-PEM fuel cell stack itself. This is required due to the known deleterious effect of carbon monoxide on the cell [25].

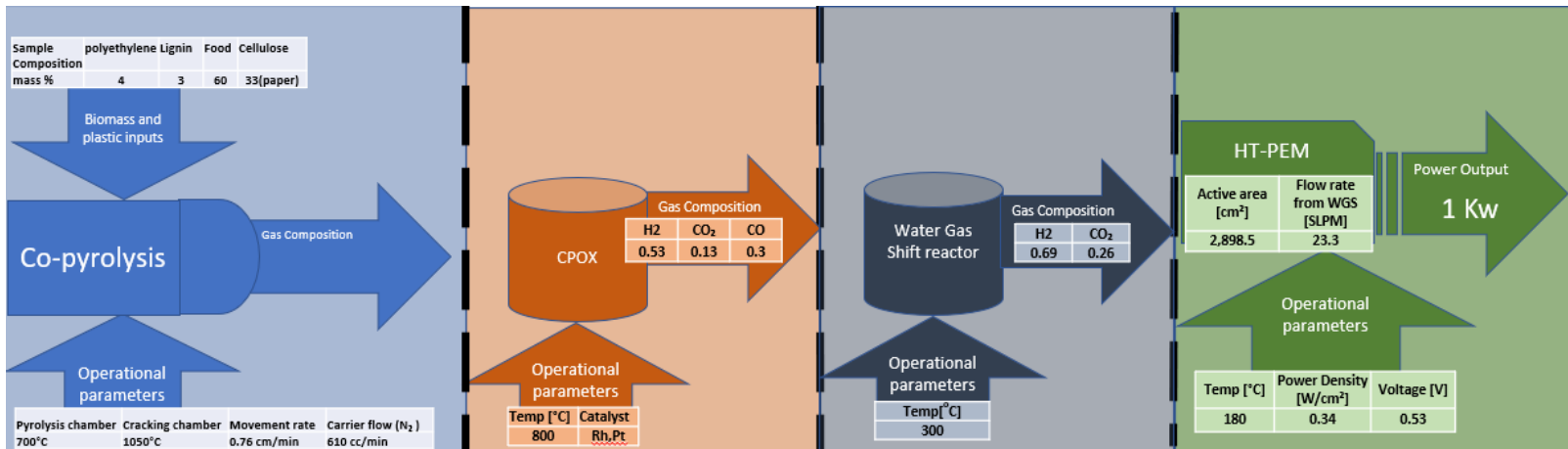


Figure 7.3: Sub-models of co-pyrolysis, two fuel reforming stages, and HT-PEM systems

As in Figure 7.2 the blue region in Figure 7.3 represents the pyrolysis process as reported by Serio et al. (2008). The first reforming stage shows a catalytic partial oxidation process (CPOx), chosen over a steam reforming process due to the parasitic loss of heating the steam reforming reaction and the scaling issues with downsizing a water gas shift reactor [26].



The CPOx reaction is exothermic, thus offering a smaller footprint, is less expensive, and with the inclusion of a catalyst can offer conversion efficiency with H₂/CO ratios of 2:1 over steam reforming. Equation 7.4 describes the CPOx reaction for methane [27,28]. The reaction of ethylene with a CPOx reaction is not as well documented. Equation 7.5 describes the equilibrium for ethylene conversion via CPOx, but in practice ethylene has been linked to increased coke and soot production [29]. The buildup of coke and soot can lead to the deactivation of the catalysts and a loss in conversion efficiency of the reformer. However, in the coke and soot scenario, the ethylene formed within the reactor may be an indicator of a system level issue or an incomplete/side reaction rather than an effect of the ethylene itself. In this study, it is assumed that complete reforming of all gases occurs via the equations above, with ethylene conversion via Equation 7.5. From the reactions above, the gas flow out of the CPOx reactor and into the water gas shift may be calculated.

The water gas shift reaction follows Equation 7.3 above and is included to reduce the concentration of CO within the reactant stream. The impact of CO on PEM fuel cells is widely documented and it is known to have a negative impact on cell performance and longevity [30]. Through the addition of water, CO is converted into additional H₂ and CO₂. This is beneficial to the cell performance as CO₂ is known to have only a diluting effect on a HT-PEM cell, contributing a relatively small mass transport voltage loss at high current density [31].

Cost Analysis

The foundation of the cost analysis presented below was the previously mentioned study by James (2012) that analyzed the costs of SOFC, LT-PEM and HT-PEM fuel cell systems. Several updates were made to the cost data included here. Due to the technical rationale outlined above, it was determined that current SOFC systems should not require a separate fuel reforming sub-system when fueled with hydrogen-rich syngas produced by biomass-plastic co-pyrolysis. This is due to the difference in the source of reactants between the two studies, the pyrolysis system generating a fuel stream with a relatively high starting concentration of H₂ instead of the methane (natural gas) fuel assumed by James. Additionally, as the price data in the James study were published in 2012 or earlier, an adjustment for inflation of 30% over that period has been made to reflect the change in price over time [32]. This value was sourced from the US bureau of labor statistics using the consumer price index. The inflation rate calculated uses the average rate of inflation from 2012 to the average of the months of January-September in 2022. Data for the full year of 2022 is not available. Furthermore, based on the HT-PEM performance data established in the previous chapters, as well as the cited studies on the performance of SOFC on biogas and reformat, adjustments were made to the stack cost. This had the effect of decreasing the cost of both the SOFC and HT-PEM stacks, reflecting on the improvements in performance achieved in recent years.

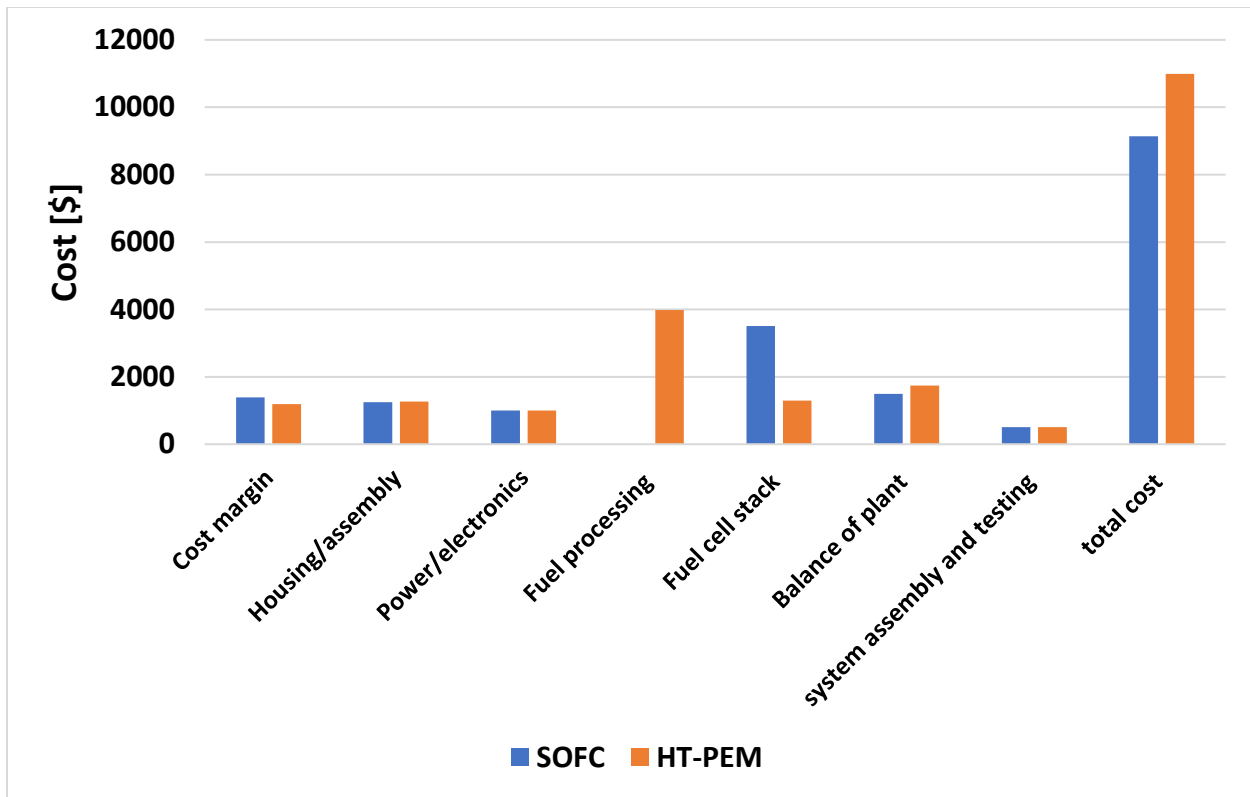


Figure 7.4: Presentation of cost data for 1 kW SOFC and HT-PEM systems at annual production scale of 100 units/year

From Figure 7.4 it can be seen that the total cost of the SOFC system is lower than the HT-PEM alternative. Between the two, most components are of comparable cost. There are two major factors influencing the difference in price between the two systems, the fuel processing cost, and the fuel cell stack cost. The fuel processing cost of the SOFC is zero due to the internal reforming assumed for the cell. For HT-PEM, the cost of reforming was reduced by 75% due to the more favorable composition of the co-pyrolysis gas used in this study. However, this sub-system still represents a large cost to the HT-PEM system that is not present in the SOFC case. The values used for the price data for HT-PEM and SOFC are displayed in table 7.4 below.

Table 7.4: Comparative cost data for SOFC and HT-PEM systems in 2022 dollars

Component	SOFC [\$]	HT-PEM [\$]
Cost margin	1390	1190
Housing/assembly	1250	1270
Power/electronics	1000	1000
Fuel processing	0	3980
Fuel cell stack	3510	1300
Balance of plant	1490	1750
System assembly and testing	500	500
Total cost	9140	10,990

The cost of the pyrolysis unit was not included in this study as there does not exist much price data for small-scale pyrolysis units. Additionally, the required reactant flow for the SOFC and HT-PEM systems are so similar, that an almost identical co-pyrolysis unit would be required for both scenarios, with no significant impact on the cost difference.

Conclusions and Future Work

With the total cost of the SOFC system in Figure 7.4 being greater than the cost of the HT-PEM system it was shown that for a 1 kW system operating off a co-pyrolysis unit, SOFC would be a less expensive option. This confirmed our initial hypothesis and was due to the option of internal reforming within the SOFC stack despite the increased cost of SOFC stacks over that of HT-PEM. In future work it would be beneficial to investigate the effect of ethylene and methane on a HT-PEM cell. If like carbon dioxide, methane and ethylene can be considered dilutants, rather than a contaminant like carbon monoxide it may allow the simplification of the reforming stages, bringing costs down for HT-PEM. This would have the impact of requiring a greater flow rate to increase the amount of hydrogen to make up for what was not gained due to reforming. However, in this study the feedstock was considered a waste and assigned no cost.

Citations Chapter 7

- [1] Nordin, Normayati. "Limitations of Commercializing Fuel Cell Technologies." AIP Conference Proceedings. Vol. 1225. No. 1. American Institute of Physics, 2010.
- [2] Nardella, Federica, Simona Bellavia, Marco Mattonai, and Erika Ribechini. "Co-pyrolysis of biomass and plastic: Synergistic effects and estimation of elemental composition of pyrolysis oil by analytical pyrolysis–gas chromatography/mass spectrometry." *Bioresource Technology* 354 (2022): 127170.
- [3] Cisse, Ibrahim, Yvan D. Hernandez-Charpak, Carlos A. Diaz, and Thomas A. Trabold. "Biochar derived from pyrolysis of common agricultural waste feedstocks and co-pyrolysis with low-density polyethylene mulch film." *Waste and Biomass Valorization* (2022): 1-20.
- [4] James, Brian D., Andrew B. Spisak, and Whitney G. Colella. "Manufacturing cost analysis of stationary fuel cell systems." *Strategic Analysis Inc. Arlington, VA* (2012).
- [5] Cornelissen, Tom, Jan Yperman, Guy Reggers, Sonja Schreurs, and Robert Carleer. "Flash co-pyrolysis of biomass with polylactic acid. Part 1: Influence on bio-oil yield and heating value." *Fuel* 87, no. 7 (2008): 1031-1041.
- [6] Serio, M. A., Erik Kroo, Elizabeth Florczak, Marek Wójtowicz, Kanapathipillai Wignarajah, John Hogan, and John Fisher. "Pyrolysis of mixed solid food, paper, and packaging wastes." In *38th International Conference on Environmental Systems, San Francisco, CA*. 2008.
- [7] Cornelissen, Tom, M. Jans, Jan Yperman, Guy Reggers, Sonja Schreurs, and Robert Carleer. "Flash co-pyrolysis of biomass with polyhydroxybutyrate: Part 1. Influence on bio-oil yield,

water content, heating value and the production of chemicals." *Fuel* 87, no. 12 (2008): 2523-2532.

[8] Paradela, Filipe, Filomena Pinto, Ibrahim Gulyurtlu, Isabel Cabrita, and Nuno Lapa. "Study of the co-pyrolysis of biomass and plastic wastes." *Clean Technologies and Environmental Policy* 11, no. 1 (2009): 115-122.

[9] Cornelissen, Tom, M. Jans, Mark Stals, Tom Kuppens, Theo Thewys, G. K. Janssens, H. Pastijn et al. "Flash co-pyrolysis of biomass: The influence of biopolymers." *Journal of Analytical and Applied Pyrolysis* 85, no. 1-2 (2009): 87-97.

[10] Rutkowski, Piotr. "Influence of zinc chloride addition on the chemical structure of bio-oil obtained during co-pyrolysis of wood/synthetic polymer blends." *Waste management* 29, no. 12 (2009): 2983-2993.

[11] Brebu, Mihai, Suat Ucar, Cornelia Vasile, and Jale Yanik. "Co-pyrolysis of pine cone with synthetic polymers." *Fuel* 89, no. 8 (2010): 1911-1918.

[12] Önal, Eylem, Başak Burcu Uzun, and Ayşe Eren Pütün. "An experimental study on bio-oil production from co-pyrolysis with potato skin and high-density polyethylene (HDPE)." *Fuel processing technology* 104 (2012): 365-370.

[13] Liu, Wu-Jun, Ke Tian, Hong Jiang, Xue-Song Zhang, and Guang-Xi Yang. "Preparation of liquid chemical feedstocks by co-pyrolysis of electronic waste and biomass without formation of polybrominated dibenzo-p-dioxins." *Bioresource technology* 128 (2013): 1-7.

[14] Alvarez, Jon, Shogo Kumagai, Chunfei Wu, Toshiaki Yoshioka, Javier Bilbao, Martin Olazar, and Paul T. Williams. "Hydrogen production from biomass and plastic mixtures by

pyrolysis-gasification." *International Journal of Hydrogen Energy* 39, no. 21 (2014): 10883-10891.

[15] Abnisa, Faisal, WMA Wan Daud, and J. N. Sahu. "Pyrolysis of mixtures of palm shell and polystyrene: an optional method to produce a high-grade of pyrolysis oil." *Environmental Progress & Sustainable Energy* 33, no. 3 (2014): 1026-1033.

[16] Abnisa, Faisal, and Wan Mohd Ashri Wan Daud. "A review on co-pyrolysis of biomass: an optional technique to obtain a high-grade pyrolysis oil." *Energy Conversion and Management* 87 (2014): 71-85.

[17] Singh, Prabhakar, and Boxun Hu. *Advanced Anode for Internal Reforming and Thermal Management in Solid Oxide Fuel Cells*. Univ. of Connecticut, Storrs, CT (United States), 2020.

[18] Shiratori, Y., T. Oshima, and K. Sasaki. "Feasibility of direct-biogas SOFC." *International Journal of Hydrogen Energy* 33, no. 21 (2008): 6316-6321.

[19] Saunders, J. E. A., and M. H. Davy. "In-situ studies of gas phase composition and anode surface temperature through a model DIR-SOFC steam–methane reformer at 973.15 K." *International journal of hydrogen energy* 38, no. 31 (2013): 13762-13773.

[20] Quang-Tuyen, Tran, Yusuke Shiratori, and Kazunari Sasaki. "Feasibility of palm-biodiesel fuel for a direct internal reforming solid oxide fuel cell." *International journal of energy research* 37, no. 6 (2013): 609-616.

[21] Yang, Lu, Maxim P. Bukhovko, Andrzej Malek, Liwei Li, Christopher W. Jones, Pradeep K. Agrawal, and Robert J. Davis. "Steam reforming of ethylene over nickel based spinel oxides." *Applied Catalysis A: General* 603 (2020): 117739.

- [22] Araki, Sadao, Naoe Hino, Takuma Mori, and Susumu Hikazudani. "Durability of a Ni based monolithic catalyst in the autothermal reforming of biogas." *International journal of hydrogen energy* 34, no. 11 (2009): 4727-4734.
- [23] Fu, Xian-Zhu, Jing-Li Luo, Alan R. Sanger, Nemanja Danilovic, and Karl T. Chuang. "An integral proton conducting SOFC for simultaneous production of ethylene and power from ethane." *Chemical communications* 46, no. 12 (2010): 2052-2054.
- [24] Wuillemmin, Zacharie, S. Ceschini, Y. Antonetti, C. Beetschen, S. Modena, D. Montinaro, T. Cornu, O. Bucheli, and M. Bertoldi. "High-performance SOFC stacks tested under different reformate compositions." In *11th European SOFC & SOE Forum Lucerne A*, vol. 901. 2014.
- [25] Søndergaard, Stine, Lars Nilausen Cleemann, Jens Oluf Jensen, and Niels J. Bjerrum. "Influence of carbon monoxide on the cathode in high-temperature polymer electrolyte membrane fuel cells." *International Journal of Hydrogen Energy* 42, no. 5 (2017): 3309-3315.
- [26] Ogden, Joan M. "Review of small stationary reformers for hydrogen production." *Report to the international energy agency* 609 (2001).
- [27] Mhadeshwar, A. B., and D. G. Vlachos. "A catalytic reaction mechanism for methane partial oxidation at short contact times, reforming, and combustion, and for oxygenate decomposition and oxidation on platinum." *Industrial & engineering chemistry research* 46, no. 16 (2007): 5310-5324
- [28] Ma, Ruoshui, Bang Xu, and Xiao Zhang. "Catalytic partial oxidation (CPOX) of natural gas and renewable hydrocarbons/oxygenated hydrocarbons—A review." *Catalysis Today* 338 (2019): 18-30.

- [29] Trabold, T. A., J. S. Lylak, M. R. Walluk, J. F. Lin, and D. R. Troiani. "Measurement and analysis of carbon formation during diesel reforming for solid oxide fuel cells." *International journal of hydrogen energy* 37, no. 6 (2012): 5190-5201.
- [30] Camara, G. A., Edson Antonio Ticianelli, S. Mukerjee, S. J. Lee, and J. McBreen. "The CO poisoning mechanism of the hydrogen oxidation reaction in proton exchange membrane fuel cells." *Journal of The Electrochemical Society* 149, no. 6 (2002): A748.
- [31] Larminie, James, Andrew Dicks, and Maurice S. McDonald. *Fuel cell systems explained*. Vol. 2. Chichester, UK: J. Wiley, 2003.
- [32] U.S. Bureau of Labor Statistics. (n.d.). CPI inflation calculator. U.S. Bureau of Labor Statistics. Retrieved November 16, 2022, from https://www.bls.gov/data/inflation_calculator.htm

Chapter 8 - Conclusions and Future Outlook

To date the majority of HT-PEM fuel cell research has been focused on improving performance through the development of novel MEA chemistries, focusing on testing at more benign operating conditions. The objective of this work was to see what is possible with the systems we currently have, operating at higher temperatures and current densities which can be considered more aggressive on the cell. In this work we focused on commercially available MEAs, establishing repeatability within constant operating conditions. With this method we were able to investigate previously understudied temperatures and current densities for HT-PEM systems. We found that operating under these aggressive conditions resulted in a greatly increased rate of degradation that we interpreted to indicate a shortened lifespan of the system.

Observing the variability in published data on the preparation of fuel cell MEAs, we identified the hot-pressing procedure to be both understudied and of importance to the fabrication of a quality PEM fuel cell MEA. By varying the hot-pressing parameters for sample MEAs we were able to optimize the pressing conditions resulting in an improved MEA performance. With this initial step we then investigated the impact of electrode layer thickness and catalyst composition. Finding thinner electrodes to be superior to a point. During hot press testing it was observed that at higher temperatures, pressures, and over longer times the MEAs performed poorly. This was shown to be a reversible process with post press rehydration, achieving an improvement in performance of the MEA.

Through preliminary ex-situ, and in-situ testing of the MEAs we identified phosphoric acid loss, taking the form of both dehydration and migration, to be the primary driver of this accelerated degradation. Attempts were made to mitigate the degradation through increasing the operating

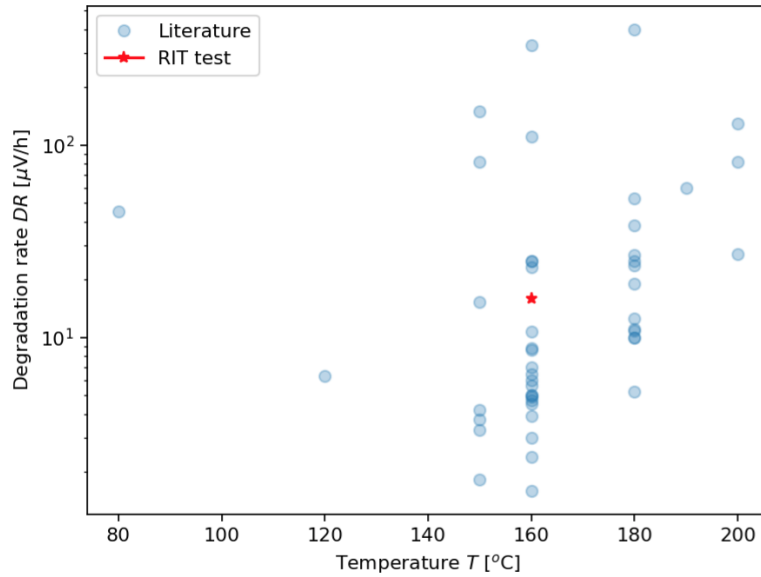
pressure and by the addition of water to the system. While water was shown to improve performance, it was not observed to have a conclusive impact on the degradation rate. Increasing the pressure, however, leads to a slightly decreased rate of voltage loss over time. Ex-situ testing showed that increasing the pressure reduced the dehydration of the phosphoric acid due to the change in the vapor pressure. It was found that the migration of electrolyte out of the system occurred at the beginning of life due to cell compression and at a greatly reduced rate during operation. SEM EDX was identified and proven to be an accurate and repeatable method for determining acid content of aqueous samples.

With the current focus of HT-PEM research geared towards innovative breakthroughs and modeling, the relatively large quantity of MEAs tested in this dissertation offered a unique opportunity to create a standardized baseline for the current performance of HT-PEM systems. This was done for 3 operating temperatures of 160, 180, and 200°C utilizing BOL POL data. This study used commercially available MEAs in repetition to establish a baseline of performance, and also tested at higher current densities finding the peak power point to be greater than anticipated. This set of data can be very beneficial for modeling and understanding the variations in performance between nominally identical MEAs.

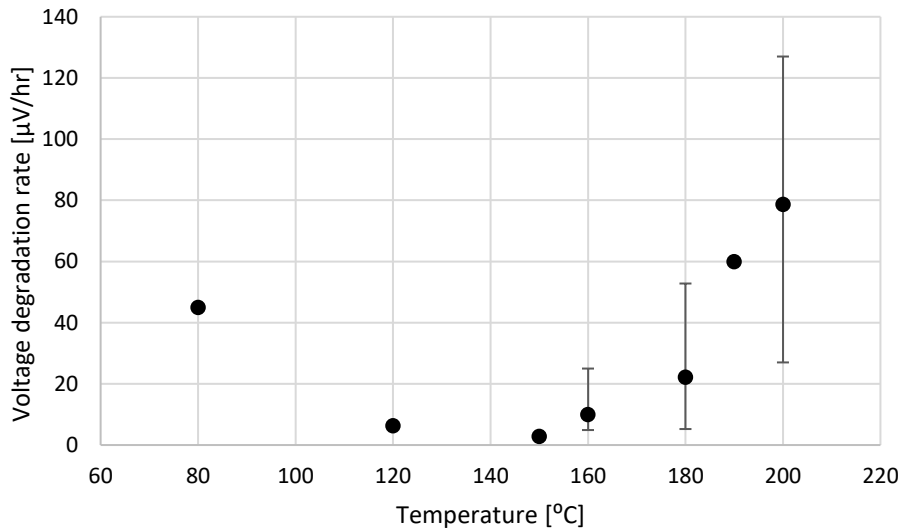
With the greatest benefit of HT-PEM systems being realized at higher temperatures it is unfortunate that operating at higher temperatures shortens the life of the system. Future research should be undertaken towards optimizing operating pressure at different temperatures to reduce acid dehydration. While the vapor pressure of phosphoric acid at 200°C may be too high to reasonably operate a system at, this may be practical for lower operating temperature such as 180°C.

One of the greatest advantages of high temperature operation is the ability to withstand higher concentrations of CO. As noted in the previous chapters CO occupies the platinum active sites leading to reduced cell performance. Future work should investigate if the CO poisoning occurring at lower temperatures is reversible at higher temperatures, and the time that this takes. If this is possible it could lead to a system which cycles a high temperature mode to mitigate the effect of CO while primarily operating at a lower temperature to reduce MEA degradation over time.

Appendix -Chapter 1



Alternate Figure 1.2 – Reported voltage degradation rates with hydrogen/air at 0.2 A/cm². Bars indicate minimum-to-maximum ranges in reported data at 160, 180 and 200°C



Alternate Figure 1.2 – Reported voltage degradation rates with hydrogen/air at 0.2 A/cm². Bars indicate minimum-to-maximum ranges in reported data at 160, 180 and 200°C

Appendix -Chapter 6

160°C POL Curves

Pilinski		
Current Density [A/cm ²]	Voltage [V]	Power Density [W/cm ²]
0	0.96	0
0.05	0.78	0.04
0.1	0.73	0.07
0.15	0.70	0.11
0.2	0.68	0.14
0.25	0.66	0.17
0.3	0.64	0.19
0.35	0.63	0.22
0.4	0.61	0.24
0.45	0.59	0.27
0.5	0.58	0.29
0.55	0.56	0.31
0.6	0.55	0.33
0.65	0.54	0.35
0.7	0.52	0.36
0.75	0.51	0.38
0.8	0.48	0.38
0.85	0.47	0.40

0.9	0.46	0.41
0.95	0.45	0.43
1	0.43	0.43

MEA C.L,Büselmann		
Current Density [A/cm ²]	Voltage [V]	Power Density [W/cm ²]
0	0.96	0.00
0.05	0.76	0.04
0.1	0.72	0.07
0.15	0.69	0.10
0.2	0.67	0.13
0.25	0.64	0.16
0.3	0.62	0.19
0.35	0.60	0.21
0.4	0.58	0.23
0.45	0.56	0.25
0.5	0.54	0.27
0.55	0.53	0.29
0.6	0.51	0.30
0.65	0.49	0.32
0.7	0.47	0.33
0.75	0.45	0.33
0.8	0.43	0.34
0.85	0.40	0.34

MEA B.L,Büselmann		
Current Density [A/cm ²]	Voltage [V]	Power Density [W/cm ²]
0	0.93	0.00
0.05	0.74	0.04
0.1	0.71	0.07
0.15	0.69	0.10
0.2	0.66	0.13
0.25	0.65	0.16
0.3	0.63	0.19
0.35	0.62	0.22
0.4	0.60	0.24
0.45	0.58	0.26
0.5	0.57	0.28
0.55	0.55	0.30
0.6	0.54	0.32
0.65	0.52	0.34
0.7	0.51	0.36
0.75	0.51	0.38
0.8	0.48	0.38
0.85	0.46	0.39
0.9	0.45	0.40

MEA A.L,Büselmann		
Current Density [A/cm ²]	Voltage [V]	Power Density [W/cm ²]
0	0.86	0.00
0.05	0.70	0.04
0.1	0.67	0.07
0.15	0.63	0.09
0.2	0.60	0.12
0.25	0.58	0.15
0.3	0.56	0.17
0.35	0.56	0.20
0.4	0.54	0.22
0.45	0.52	0.23
0.5	0.50	0.25
0.55	0.49	0.27
0.6	0.47	0.28
0.65	0.45	0.29
0.7	0.44	0.31
0.75	0.42	0.31
0.8	0.40	0.32

MEA C.S,Büselmann		
Current Density [A/cm ²]	Voltage [V]	Power Density [W/cm ²]
0	0.98	0.00
0.05	0.82	0.04
0.1	0.76	0.08
0.15	0.74	0.11
0.2	0.71	0.14
0.25	0.67	0.17
0.3	0.66	0.20
0.35	0.64	0.22
0.4	0.63	0.25
0.45	0.61	0.27
0.5	0.60	0.30
0.55	0.58	0.32
0.6	0.57	0.34
0.65	0.55	0.36
0.7	0.53	0.37
0.75	0.52	0.39
0.8	0.50	0.40

MEA B.S,Büselmann		
Current Density [A/cm ²]	Voltage [V]	Power Density [W/cm ²]
0	0.92	0.00
0.05	0.75	0.04
0.1	0.71	0.07
0.15	0.69	0.10
0.2	0.67	0.13
0.25	0.66	0.16
0.3	0.64	0.19
0.35	0.63	0.22
0.4	0.62	0.25
0.45	0.61	0.27
0.5	0.59	0.29
0.55	0.58	0.32
0.6	0.56	0.34
0.65	0.55	0.36
0.7	0.54	0.38
0.75	0.52	0.39
0.8	0.51	0.40

MEA A.S,Büselmann		
Current Density [A/cm ²]	Voltage [V]	Power Density [W/cm ²]
0	0.84	0.00
0.05	0.74	0.04
0.1	0.70	0.07
0.15	0.68	0.10
0.2	0.66	0.13
0.25	0.64	0.16
0.3	0.62	0.19
0.35	0.60	0.21
0.4	0.58	0.23
0.45	0.57	0.26
0.5	0.55	0.28
0.55	0.54	0.30
0.6	0.53	0.32
0.65	0.51	0.33
0.7	0.50	0.35
0.75	0.49	0.36
0.8	0.47	0.38

LC1a,Schonvogel		
Current Density [A/cm ²]	Voltage [V]	Power Density [W/cm ²]
0	0.97	0.00
0.05	0.75	0.04
0.1	0.71	0.07
0.15	0.70	0.10
0.2	0.67	0.13
0.25	0.65	0.16
0.3	0.64	0.19
0.35	0.63	0.22
0.4	0.61	0.24
0.45	0.59	0.27
0.5	0.58	0.29
0.55	0.57	0.31
0.6	0.55	0.33
0.65	0.53	0.35
0.7	0.52	0.36
0.75	0.51	0.38
0.8	0.50	0.40
0.85	0.48	0.41
0.9	0.46	0.42
0.95	0.45	0.43

1	0.44	0.44
---	------	------

LC2,Schonvogel		
Current Density [A/cm ²]	Voltage [V]	Power Density [W/cm ²]
0	0.95	0.00
0.05	0.77	0.04
0.1	0.73	0.07
0.15	0.70	0.11
0.2	0.68	0.14
0.25	0.66	0.16
0.3	0.64	0.19
0.35	0.62	0.22
0.4	0.61	0.24
0.45	0.59	0.27
0.5	0.58	0.29
0.55	0.56	0.31
0.6	0.55	0.33
0.65	0.53	0.35
0.7	0.52	0.36
0.75	0.50	0.38
0.8	0.49	0.39

0.85	0.47	0.40
0.9	0.46	0.41
0.95	0.44	0.42
1	0.43	0.43

LC1b,Schonvengle		
Current Density [A/cm ²]	Voltage [V]	Power Density [W/cm ²]
0	0.95	0.00
0.05	0.76	0.04
0.1	0.72	0.07
0.15	0.69	0.10
0.2	0.67	0.13
0.25	0.66	0.16
0.3	0.64	0.19
0.35	0.62	0.22
0.4	0.60	0.24
0.45	0.59	0.26
0.5	0.57	0.29
0.55	0.56	0.31
0.6	0.54	0.33
0.65	0.53	0.34
0.7	0.51	0.36
0.75	0.50	0.38
0.8	0.48	0.39
0.85	0.47	0.40
0.9	0.46	0.41
0.95	0.44	0.42

1	0.43	0.43
---	------	------

Waller		
Current Density [A/cm ²]	Voltage [V]	Power Density [W/cm ²]
0	1.01	0.00
0.05	0.75	0.04
0.1	0.72	0.07
0.2	0.66	0.13
0.3	0.64	0.19
0.5	0.60	0.30
0.7	0.56	0.39
0.9	0.52	0.47
1.1	0.48	0.53
1.3	0.45	0.58
1.4	0.43	0.60
1.5	0.41	0.61

Zhou		
Current Density [A/cm ²]	Voltage [V]	Power Density [W/cm ²]
0	0.96	0.00
0.05	0.69	0.03
0.1	0.62	0.06
0.15	0.57	0.09
0.2	0.52	0.10
0.25	0.48	0.12
0.3	0.42	0.13
0.35	0.36	0.13
0.4	0.27	0.11

Advent		
Current Density [A/cm ²]	Voltage [V]	Power Density [W/cm ²]
0	0.99	0.00
0.1	0.73	0.07
0.2	0.69	0.14
0.3	0.66	0.20
0.4	0.63	0.25
0.5	0.60	0.30
0.6	0.57	0.34
0.7	0.54	0.38
0.8	0.51	0.41

Cicconardi		
Current Density [A/cm ²]	Voltage [V]	Power Density [W/cm ²]
0	0.91	0.00
0.2	0.67	0.13
0.4	0.60	0.24
0.6	0.55	0.33
0.8	0.51	0.40
1	0.50	0.50

	This Study															
	PBI 9		PBI 10		PBI 11		PBI 12		PBI 13		PBI 14		PBI 16		PBI 17	
Current Density [A/cm ²]	V	W/cm ²	V	W/cm ²	V	W/cm ²	V	W/cm ²	V	W/cm ²	V	W/cm ²	V	W/cm ²	V	W/cm ²
0	1.02	0.00	1.02	0.00	1.00	0.00	0.96	0.00	1.02	0.00	0.99	0.00	1.03	0.00	0.99	0.00
0.1	0.73	0.07	0.74	0.07	0.73	0.07	0.72	0.07	0.73	0.07	0.69	0.07	0.80	0.08	0.73	0.07
0.2	0.70	0.14	0.70	0.14	0.68	0.14	0.68	0.14	0.69	0.14	0.64	0.13	0.67	0.13	0.68	0.14
0.3	0.66	0.20	0.67	0.20	0.65	0.19	0.65	0.19	0.66	0.20	0.59	0.18	0.62	0.19	0.66	0.20
0.4	0.64	0.25	0.65	0.26	0.62	0.25	0.62	0.25	0.64	0.25	0.56	0.22	0.60	0.24	0.62	0.25
0.5	0.61	0.31	0.62	0.31	0.59	0.30	0.60	0.30	0.61	0.31	0.53	0.26	0.57	0.29	0.60	0.30
0.6	0.59	0.36	0.60	0.36	0.56	0.34	0.57	0.34	0.59	0.35	0.50	0.30	0.55	0.33	0.57	0.34
0.7	0.58	0.41	0.58	0.41	0.54	0.38	0.55	0.39	0.56	0.39	0.47	0.33	0.52	0.36	0.55	0.39
0.8	0.55	0.44	0.56	0.45	0.51	0.41	0.53	0.42	0.53	0.42	0.45	0.36	0.50	0.40	0.53	0.42
0.9	0.52	0.47	0.55	0.49	0.48	0.44	0.51	0.46	0.51	0.46	0.42	0.38	0.48	0.43	0.50	0.45
1	0.51	0.51	0.52	0.52	0.46	0.46	0.48	0.48	0.48	0.48	0.40	0.40	0.44	0.44	0.47	0.47
1.1	0.49	0.53	0.50	0.55	0.43	0.47	0.46	0.50	0.47	0.52	0.38	0.41	0.41	0.45	0.44	0.48
1.2	0.46	0.56	0.48	0.57	0.40	0.47	0.43	0.52	0.44	0.53	0.35	0.42	0.39	0.46	0.42	0.50
1.3	0.44	0.58	0.46	0.59	0.36	0.47	0.42	0.55	0.38	0.50	0.33	0.43	0.36	0.47	0.38	0.50
1.4	0.42	0.59	0.43	0.61	0.33	0.46	0.38	0.54	0.33	0.46	0.30	0.42	0.33	0.46	0.36	0.50
1.5	0.40	0.59	0.41	0.61	0.29	0.43	0.36	0.53	0.30	0.45	0.29	0.43	0.30	0.45	0.33	0.50
1.6	0.37	0.59	0.38	0.61	0.24	0.39	0.33	0.52	0.25	0.40	0.27	0.43	0.27	0.43	0.30	0.48

POL curve data for PBI MEAs run in this study at 160°C, stoichiometric ratio of 1.5,2 H₂/Air and 101.3 kPa, with column v showing voltage and W/cm² showing power density.

	This Study					
	PBI 9		PBI 10		PBI 12	
Current Density [A/cm ²]	V	W/cm ²	V	W/cm ²	V	W/cm ²
0	1.02	0.00	1.05	0.00	1.03	0.00
0.1	0.77	0.08	0.77	0.08	0.76	0.08
0.2	0.73	0.15	0.72	0.14	0.72	0.14
0.3	0.70	0.21	0.70	0.21	0.69	0.21
0.4	0.68	0.27	0.66	0.27	0.66	0.26
0.5	0.66	0.33	0.64	0.32	0.64	0.32
0.6	0.64	0.38	0.61	0.37	0.62	0.37
0.7	0.62	0.44	0.60	0.42	0.59	0.42
0.8	0.59	0.47	0.57	0.46	0.57	0.46
0.9	0.58	0.52	0.55	0.50	0.55	0.50
1	0.56	0.56	0.53	0.53	0.53	0.53
1.1	0.54	0.59	0.51	0.56	0.51	0.56
1.2	0.52	0.62	0.48	0.58	0.49	0.59
1.3	0.50	0.65	0.46	0.60	0.47	0.61
1.4	0.49	0.68	0.43	0.61	0.45	0.63
1.5	0.47	0.70	0.41	0.62	0.42	0.64
1.6	4.51	7.22	0.39	0.62	0.40	0.64

POL curve data for PBI MEAs run in this study at 160°C, stoichiometric ratio of 1.5,2 H₂/Air and 200 kPa, with column v showing voltage

and W/cm² showing power density.

180°C POL Curves

Zhou		
Current Density [A/cm ²]	Voltage [V]	Power Density [W/cm ²]
0.00	0.98	0.00
0.03	0.78	0.02
0.05	0.73	0.04
0.08	0.69	0.05
0.10	0.66	0.07
0.13	0.63	0.08
0.15	0.61	0.09
0.18	0.58	0.10
0.20	0.56	0.11
0.23	0.53	0.12
0.25	0.51	0.13
0.28	0.48	0.13
0.30	0.44	0.13
0.33	0.40	0.13
0.35	0.36	0.12
0.38	0.31	0.12
0.40	0.26	0.10

Cicconardi		
Current Density [A/cm ²]	Voltage [V]	Power Density [W/cm ²]
0	0.91	0.00
0.05	0.76	0.04
0.1	0.71	0.07
0.15	0.67	0.10
0.2	0.64	0.13
0.25	0.61	0.15
0.3	0.59	0.18
0.35	0.57	0.20
0.4	0.55	0.22
0.45	0.53	0.24
0.5	0.51	0.25
0.55	0.49	0.27
0.6	0.47	0.28
0.65	0.45	0.29
0.7	0.43	0.30
0.75	0.41	0.31

Tseng		
Current Density [A/cm ²]	Voltage [V]	Power Density [W/cm ²]
0	0.92	0.00
0.04	0.79	0.03
0.08	0.73	0.06
0.1	0.72	0.07
0.14	0.69	0.10
0.20	0.66	0.13
0.25	0.63	0.16
0.30	0.61	0.18
0.35	0.59	0.20
0.40	0.57	0.23
0.49	0.53	0.26
0.50	0.52	0.26
0.60	0.49	0.29
0.70	0.45	0.31
0.74	0.43	0.32
0.80	0.40	0.32
0.82	0.39	0.32
0.90	0.34	0.31
0.93	0.33	0.30

Waller		
Current Density [A/cm ²]	Voltage [V]	Power Density [W/cm ²]
0	1.00	0.00
0.05	0.76	0.04
0.1	0.73	0.07
0.2	0.69	0.14
0.3	0.66	0.20
0.5	0.61	0.31
0.7	0.57	0.40
0.9	0.54	0.48
1.1	0.50	0.55
1.3	0.46	0.60
1.4	0.44	0.61
1.5	0.42	0.63

	This Study															
	PBI 9		PBI 10		PBI 11		PBI 12		PBI 13		PBI 14		PBI 16		PBI 17	
Current Density [A/cm ²]	V	W/cm ²	V	W/cm ²	V	W/cm ²	V	W/cm ²	V	W/cm ²	V	W/cm ²	V	W/cm ²	V	W/cm ²
0	1.01	0.00	1.00	0.00	0.99	0.00	1.00	0.00	1.02	0.00	0.98	0.00	0.99	0.00	0.98	0.00
0.1	0.74	0.07	0.74	0.07	0.73	0.07	0.73	0.07	0.73	0.07	0.69	0.07	0.72	0.07	0.74	0.07
0.2	0.69	0.14	0.70	0.14	0.65	0.13	0.69	0.14	0.71	0.14	0.66	0.13	0.64	0.13	0.68	0.14
0.3	0.66	0.20	0.67	0.20	0.63	0.19	0.66	0.20	0.68	0.20	0.61	0.18	0.59	0.18	0.65	0.20
0.4	0.64	0.26	0.65	0.26	0.62	0.25	0.63	0.25	0.63	0.25	0.57	0.23	0.52	0.21	0.62	0.25
0.5	0.62	0.31	0.63	0.31	0.59	0.30	0.60	0.30	0.62	0.31	0.54	0.27	0.49	0.24	0.60	0.30
0.6	0.60	0.36	0.61	0.36	0.56	0.34	0.58	0.35	0.61	0.36	0.50	0.30	0.45	0.27	0.58	0.35
0.7	0.58	0.40	0.59	0.41	0.54	0.38	0.56	0.39	0.59	0.42	0.48	0.34	0.44	0.31	0.55	0.38
0.8	0.55	0.44	0.57	0.45	0.51	0.41	0.53	0.43	0.57	0.46	0.44	0.36	0.42	0.34	0.53	0.42
0.9	0.54	0.48	0.55	0.49	0.48	0.43	0.51	0.46	0.56	0.50	0.43	0.38	0.40	0.36	0.50	0.45
1	0.52	0.52	0.52	0.52	0.46	0.46	0.49	0.49	0.53	0.53	0.40	0.40	0.40	0.40	0.47	0.47
1.1	0.50	0.55	0.51	0.56	0.43	0.47	0.46	0.51	0.50	0.55	0.38	0.42	0.38	0.42	0.46	0.50
1.2	0.48	0.57	0.49	0.59	0.40	0.48	0.44	0.53	0.48	0.58	0.35	0.42	0.37	0.45	0.43	0.52
1.3	0.46	0.59	0.48	0.62	0.36	0.47	0.41	0.54	0.43	0.56	0.33	0.43	0.36	0.46	0.42	0.54
1.4	0.44	0.62	0.46	0.65	0.33	0.46	0.38	0.54	0.43	0.60	0.31	0.43	0.34	0.48	0.38	0.53
1.5	0.42	0.63	0.44	0.66	0.29	0.44	0.36	0.53	0.40	0.60	0.29	0.43	0.31	0.46	0.36	0.55
1.6	0.40	0.64	0.41	0.66	0.25	0.40	0.32	0.52	0.37	0.59	0.27	0.43	0.26	0.42	0.33	0.52

POL curve data for PBI MEAs run in this study at 180°C, stoichiometric ratio of 1.5,2 H₂/Air and 101.3 kPa, with column v showing voltage and W/cm² showing power density.

	This Study					
	PBI 9		PBI 10		PBI 12	
Current Density [A/cm ²]	V	W/cm ²	V	W/cm ²	V	W/cm ²
0	1.01	0.00	1.05	0.00	1.01	0.00
0.1	0.74	0.07	0.78	0.08	0.76	0.08
0.2	0.69	0.14	0.74	0.15	0.73	0.15
0.3	0.66	0.20	0.71	0.21	0.69	0.21
0.4	0.64	0.26	0.68	0.27	0.67	0.27
0.5	0.62	0.31	0.66	0.33	0.64	0.32
0.6	0.60	0.36	0.64	0.38	0.63	0.38
0.7	0.58	0.40	0.61	0.43	0.60	0.42
0.8	0.55	0.44	0.59	0.47	0.58	0.47
0.9	0.54	0.48	0.56	0.51	0.56	0.51
1	0.52	0.52	0.54	0.54	0.54	0.54
1.1	0.50	0.55	0.51	0.56	0.52	0.58
1.2	0.48	0.57	0.51	0.61	0.50	0.60
1.3	0.46	0.59	0.50	0.65	0.48	0.63
1.4	0.44	0.62	0.48	0.68	0.46	0.64
1.5	0.42	0.63	0.46	0.69	0.44	0.65
1.6	0.40	0.64	0.44	0.71	0.41	0.66

POL curve data for PBI MEAs run in this study at 180°C, stoichiometric ratio of 1.5,2 H₂/Air and 200 kPa, with column v showing voltage and W/cm² showing power density.

200°C POL Curves

Waller		
Current Density [A/cm ²]	Voltage [V]	Power Density [W/cm ²]
0.05	0.78	0.04
0.1	0.74	0.07
0.2	0.69	0.14
0.3	0.67	0.20
0.5	0.62	0.31
0.7	0.58	0.40
0.9	0.54	0.49
1.1	0.50	0.55
1.3	0.46	0.60
1.4	0.44	0.61
1.5	0.42	0.63

Yang		
Current Density [A/cm ²]	Voltage [V]	Power Density [W/cm ²]
0	1.00	0.00
0.05	0.78	0.04
0.1	0.75	0.08
0.2	0.71	0.14
0.3	0.68	0.20
0.5	0.64	0.32
0.7	0.61	0.43
0.9	0.57	0.52
1.1	0.54	0.59
1.3	0.50	0.65
1.5	0.45	0.67

Current Density [A/cm ²]	This Study																			
	PBI 6		PBI 7		PBI 9		PBI 10		PBI 11		PBI 12		PBI 13		PBI14		PBI 16		PBI 17	
	V	W/cm ²	V	W/cm ²	V	W/cm ²	V	W/cm ²	V	W/cm ²	V	W/cm ²	V	W/cm ²	V	W/cm ²	V	W/cm ²	V	W/cm ²
0	0.96	0.00	1.00	0.00	1.01	0.00	0.99	0.00	1.00	0.00	1.00	0.00	1.02	0.00	0.99	0.00	1.02	0.00	0.97	0.00
0.1	0.72	0.07	0.74	0.07	0.74	0.07	0.75	0.07	0.73	0.07	0.73	0.07	0.74	0.07	0.70	0.07	0.80	0.08	0.72	0.07
0.2	0.68	0.14	0.71	0.14	0.70	0.14	0.71	0.14	0.68	0.14	0.69	0.14	0.71	0.14	0.66	0.13	0.68	0.14	0.66	0.13
0.3	0.65	0.19	0.68	0.20	0.67	0.20	0.68	0.20	0.65	0.20	0.65	0.20	0.68	0.21	0.62	0.18	0.63	0.19	0.63	0.19
0.4	0.62	0.25	0.65	0.26	0.64	0.26	0.65	0.26	0.62	0.25	0.62	0.25	0.63	0.25	0.58	0.23	0.60	0.24	0.61	0.24
0.5	0.60	0.30	0.63	0.32	0.62	0.31	0.63	0.32	0.60	0.30	0.60	0.30	0.63	0.31	0.56	0.28	0.58	0.29	0.55	0.27
0.6	0.58	0.35	0.61	0.37	0.60	0.36	0.61	0.37	0.57	0.34	0.57	0.34	0.61	0.37	0.52	0.31	0.54	0.33	0.53	0.32
0.7	0.56	0.39	0.60	0.42	0.58	0.40	0.59	0.41	0.55	0.38	0.55	0.38	0.59	0.41	0.50	0.35	0.52	0.36	0.51	0.36
0.8	0.53	0.43	0.58	0.47	0.56	0.45	0.57	0.46	0.52	0.42	0.52	0.42	0.57	0.46	0.45	0.36	0.49	0.39	0.49	0.39
0.9	0.52	0.46	0.56	0.50	0.53	0.48	0.55	0.50	0.49	0.44	0.50	0.45	0.57	0.51	0.44	0.40	0.47	0.42	0.46	0.41
1	0.49	0.49	0.54	0.54	0.51	0.51	0.53	0.53	0.47	0.47	0.47	0.47	0.53	0.53	0.41	0.41	0.44	0.44	0.43	0.43
1.1	0.47	0.52	0.52	0.57	0.49	0.53	0.51	0.56	0.44	0.48	0.44	0.49	0.52	0.57	0.39	0.42	0.40	0.44	0.41	0.45
1.2	0.45	0.54	0.50	0.59	0.46	0.55	0.49	0.59	0.41	0.49	0.41	0.50	0.49	0.59	0.38	0.45	0.38	0.45	0.37	0.44
1.3	0.44	0.57	0.48	0.63	0.44	0.58	0.47	0.61	0.38	0.49	0.40	0.52	0.45	0.59	0.35	0.46	0.36	0.46	0.34	0.44
1.4	0.42	0.58	0.46	0.65	0.41	0.57	0.45	0.63	0.34	0.48	0.36	0.50	0.43	0.61	0.33	0.46	0.33	0.46	0.30	0.42
1.5	0.40	0.60	0.43	0.65	0.38	0.57	0.42	0.63	0.30	0.46	0.33	0.49	0.41	0.61	0.31	0.46	0.30	0.44	0.26	0.40
1.6	0.35	0.56	0.43	0.68	0.35	0.56	0.40	0.64	0.27	0.42	0.29	0.47	0.38	0.60	0.28	0.45	0.26	0.42	0.22	0.36

POL curve data for PBI MEAs run in this study at 200°C, stoichiometric ratio of 1.5,2 H₂/Air and 101.3 kPa, with column v showing voltage and W/cm² showing power density.

	This Study					
	PBI 9		PBI 10		PBI 12	
Current Density [A/cm ²]	V	W/cm ²	V	W/cm ²	V	W/cm ²
0	1.03	0.00	1.03	0.00	1.01	0.00
0.1	0.79	0.08	0.80	0.08	0.76	0.08
0.2	0.75	0.15	0.75	0.15	0.75	0.15
0.3	0.72	0.22	0.73	0.22	0.71	0.21
0.4	0.70	0.28	0.70	0.28	0.67	0.27
0.5	0.67	0.34	0.69	0.34	0.64	0.32
0.6	0.66	0.39	0.66	0.40	0.62	0.37
0.7	0.64	0.45	0.65	0.45	0.60	0.42
0.8	0.62	0.50	0.63	0.50	0.58	0.46
0.9	0.60	0.54	0.62	0.55	0.56	0.50
1	0.58	0.58	0.60	0.60	0.54	0.54
1.1	0.57	0.62	0.58	0.64	0.52	0.57
1.2	0.54	0.65	0.56	0.67	0.50	0.60
1.3	0.53	0.68	0.55	0.71	0.48	0.62
1.4	0.51	0.71	0.53	0.74	0.45	0.64
1.5	0.49	0.74	0.51	0.76	0.43	0.65
1.6	0.46	0.74	0.49	0.78	0.41	0.65

POL curve data for PBI MEAs run in this study at 200°C, stoichiometric ratio of 1.5,2 H₂/Air and 200 kPa, with column v showing voltage and W/cm² showing power density.

Reference	MEA Type	Area [cm ²]	Temperature [°C]	Stoich Ratio [H ₂ /Air]	Notes
Present study	Advent PBI	45.2	160,180,200	1.5/2	
Cicconardi et al. (2011)	Commercial	45	160,180	1.2/2	Back pressure set to 1.2 bar
Pilinski et al. (2015)	Celtec®-P1100W	20.25	160	1.5/2	Tested load cycling and acid uptake into flow fields.
Schonvogel et al. (2015)	Celtec®-P1100W	20.25	160	1.5/2	Beginning of life data from several different AST
Tseng et al. (2016)	Advent TPS®	25	180	1.2/3	Also did studies with a metal foam flow field; these data not included
Waller et al. (2016)	Advent PBI	45.2	160,180,200	1.5/2	
Büsselmann et al. (2017)	Commercial	25	160	1.5/2	The difference in MEA (S vs. L) was tested after characterization, but did not impact BOL POL.
Zhou et al. (2019)	Dapozol G77	46.5	160,180	2/4	Assessed the effect of humidity
Yang (2019)	Advent PBI	45.2	200	1.5/2	
Advent (2020)	Advent PBI		160	1.2/2	